UNIVERSITY OF CANTERBURY

Department of Physics and Astronomy

CHRISTCHURCH NEW ZEALAND

Monte Carlo Investigation into Superficial Cancer Treatments of the Head and Neck

A thesis
submitted in partial fulfilment
of the requirements for the Degree
of
Master of Science in Medical Physics
in the
University of Canterbury
by

Bryn Currie

Monte Carlo Investigation into Superficial Cancer Treatments of the Head and Neck

Bryn Currie

MSc Supervisors:
Assoc. Prof. Lou Reinisch & Lynne Greig

Abstract

This thesis presents the findings of the investigation into the Monte Carlo simulation of superficial cancer treatments of the head and neck region. The EGSnrc system of codes for the Monte Carlo simulation of the transport of electrons and photons through a phantom representative of either a water phantom or treatment site in a patient is utilised. Two clinical treatment units are simulated using the BEAMnrc system of codes: the Varian Medical Systems Clinac® 2100C accelerator for 6MeV electron fields and the Pantak Therapax SXT 150 X-ray unit for 80kV and 100kV photon fields. Depth dose, profile and isodose curves are compared against those measured from a PTW MP3 water phantom with good agreement being achieved. Quantitative dose distributions are determined for both MeV electron and kV photon fields with treatment sites containing high atomic number materials, rapidly sloping surfaces and different density interfaces. This highlights the relatively high level of dose deposition of dose in tissue-bone and tissue-cartilage interfaces in the kV photon fields. From these dose distributions DVH and dose comparators are used to assess the simulated treatment fields.

I will remember that I do not treat... a cancerous growth, but a sick human being, whose illness may affect the person's family... Louis Lasagna, 1964

Contents

Figures

Tables

Chapter 1

Introduction

This thesis presents the results of an investigation into the amalgamation of Monte Carlo simulation methods and electron and photon physics in the 10^3–10^6 eV energy range to find optimal solutions to radiotherapy treatments of superficial cancers of the head and neck region. The motivation for this research has been provided by the difficulties in calculating dose distributions for MeV electron and kV photon fields in complex geometries (*i.e.* areas containing sloping surfaces, inhomogeneous media, polychromatic radiation fields and high atomic number materials) given the current tools in a typical radiotherapy department. There is an enormous body of research dedicated to the interaction of particles with bulk matter (see for example references [1] and [2]) of which the mathematical formulation of the interactions of fundamental particles is in excellent agreement with experiment. This body of research is typically for simple geometries in that homogeneous semi-infinite mediums and planar monochromatic radiation fields incident normally on boundaries are considered. It is from this body of theoretical and experimental work that we shall elucidate dose deposition characteristics for medium energy (80–100 kVp) photons and high energy (6 MeV) electrons in complex geometries.

In order to place into context the concepts and tools involved in this research this chapter will give some background information and then detail the layout of the thesis.

1.1 Background

Superficial cancers can be amongst the most disfiguring and consequently socially debilitating diseases although rarely are they fatal. The vast majority of such cancers are easy to treat and rarely require radiotherapy; however, the minority of difficult to treat basal and squamous cell carcinomas typically present in regions that include radiosensitive structures and require high density materials inserted into the treatment field to adequately protect such structures. The consequences of this are that CT information on which to plan such a treatment does not provide all of the information necessary to calculate the dose distribution (either through artifacts obscuring the image and affecting the CT numbers or no CT information is gathered as is the case for patients undergoing superficial photon treatment[1]). Additionally commercial treatment planning systems do not adequately model the addition of high density materials hence any dose distribution calculated must be interpreted with a degree of caution.

There are many methods utilised in the treatment of superficial cancers; this includes, but is not limited to, cryotherapy, chemotherapy, surgery and radiotherapy in no particular order. Radiotherapy modalities that have been employed in the treatment of superficial cancers are: photons in the kilo-voltage range, electrons in the mega-voltage range and

[1]In fact there are currently no commercially available treatment planning systems that are used in planning superficial photon treatments

brachytherapy sources [3]. Brachytherapy, though a successful contemporary treatment modality, has not been investigated.

Treatment planning system algorithms are configured in such a way so as to provide clinicians with accurate information in a timely manner. This requires the incorporation of assumptions into the algorithm that allow the calculation to proceed on the order of minutes; however, these same assumptions invalidate the dose distribution calculation in the presence of high density materials, rapidly sloping surfaces and inhomogeneous regions. Each of these are present in the sites considered in the current investigation. Monte Carlo methods are starting to be used in commercial treatment planning systems but these are still a cut down version of a true Monte Carlo simulation; additionally the input information (*i.e.* accurate geometric and material information describing the treatment field) is still problematic to obtain.

The emphasis in this project is not on extending or altering the simulation techniques associated with the Monte Carlo method, it is in developing a means of assessing and hence optimising calculated dose distributions. Although this is a general statement concerning optimisation of any dose distribution the current thesis will focus on the head and neck region as the treatment of these sites contains high density materials, rapidly sloping surfaces and inhomogeneous regions.

1.2 Layout of Thesis

Due to the complex and interdisciplinary nature of the research presented in this thesis some time is spent introducing the concepts and tools used. The second chapter of this thesis will address superficial cancers of the head and neck from initially an anatomy and physiology perspective and then from a pathology perspective. The class of superficial cancers is restricted in discussion to basal and squamous cell carcinomas but due to the indiscriminate ability of radiation to be able make non-viable any cell this discussion could be expanded to include any superficial cancer. Chapter 2 will also provide a brief synopsis on the sorts of treatment associated with superficial cancers.

A brief review of the means by which current treatment planning systems undertake the calculation of dose distributions is presented in chapter 3 with the intent to contrast this with the Monte Carlo method. Only the Gaussian pencil beam model for electrons and pencil beam convolution model for photons will be discussed as these are broadly representative of typical treatment planning system algorithms. A complete review of commercial treatment planning systems will not be undertaken within this thesis as there are a number of medical physics books that review this adequately (see for example [3]). Only passing mention will be made of commercial treatment planning system algorithms utilising Monte Carlo methods (such as Varian Medical System's electron Monte Carlo algorithm, eMC) in the thesis.

After an appreciation has been built for what constitutes current and common methods for dose distribution calculation the Monte Carlo method will be detailed in chapter 4. The basis of the method will be reviewed with the intent to demonstrate the versatility and generality of the method. Hence, even though the thesis is restricted to the discussion of superficial cancers of the head and neck it is a widely applicable method in radiation oncology. Chapter 4 will also give an overview of the Monte Carlo computer codes used in the current investigation. There are a number of codes available free for research use and the National Research Council of Canada's Electron Gamma Shower system of codes

was deemed suitable given the specific radiation oncology and medical physics bias system and supplementary applications.

Chapter 5 will detail the radiation interactions that are explicitly modelled in the EGSnrc system of codes. This shall demonstrate the general nature of the Monte Carlo method but also highlight the intrinsic assumptions built into the system of codes. This is due to the need to achieve reasonable simulation times in contrast to preserving full generality of the standard model of particle physics. As such empirical fits to the observed interactions are extensively used in the EGSnrc system of codes but it shall be demonstrated that these are valid for the energy range considered in the current thesis.

The current investigation required the modelling of both a medical electron accelerator and a superficial photon unit. The medical electron accelerator modelled was a Varian Clinac® 2100C and the superficial unit modelled was a Pantak Therapax SXT150. Both of these modelling tasks are possible using the OMEGA (Ottawa Madison Electron Gamma Algorithm) collaboration system of codes called BEAMnrc[4] that allows the user to consider photons down to an energy of 1keV. Chapter 6 details the modelling and simulation of outputs from both of these units. The Clinac® studies will not be shown in full in accordance with the confidentiality agreement with Varian Medical Systems to obtain the required information to model the accelerator. All of the modelled accelerator outputs are compared with measured water phantom data.

Dose distributions in complex geometries are investigated in chapter 7. MeV electron and kV photon dose deposition studies for three treatment sites (left ear, left lateral nose and right medial canthus) will be compared and the physics behind the particular pattern of dose distribution will be discussed. The dose distributions derived are for comparison with each other only and are not used to calculate monitor units or treatment times for any medical equipment.

As a final introductory word it should be noted that within the confines of this thesis neither Varian Medical Systems nor National Research Council of Canada have developed or released information that should be used in the treatment of any patient. The information derived from the information and code systems provided are strictly for research purposes only.

Chapter 2

Superficial Cancers

New Zealand has a well publicised high rate of cancers of the skin. There are many physiological, environmental and cultural factors that may contribute to such an occurrence but it is beyond the scope of this thesis to attempt an exposition of such factors. Rather, the discussion shall be confined to a select class and manifestation of a somewhat ubiquitous cancers of the skin; namely basal and squamous cell carcinomas (BCC and SCC). Additionally, the focus shall be on only one region of the body, the head and neck, in determining the effectiveness of different modalities of radiotherapy. The head and neck is chosen as the combination of complex geometry, rapidly varying density interfaces and radiosensitive structures represents a region that is ideally suited to dose distribution determination via Monte Carlo methods.

Even though the removal of the vast majority of basal or squamous cell carcinomas is usually through excision or cryotherapy on an outpatient basis it is still a relevant area of study for radiation oncology medical physics. A relatively minor fraction of patients that present with basal or squamous cell carcinoma will require radiotherapy; similarly a fraction of these patients will have lesions in regions where treatment planning systems utilising pencil beam algorithms will have difficulty calculating dose distributions[1] Typically the radiation oncologist will prescribe superficial photons or mega-voltage electrons in treating convoluted sites with little recourse to a treatment planning system.

In the following chapter the anatomy and physiology of the head and neck shall be reviewed with an intent to show the complexity of this particular region and the problems that arise in applying radiotherapy to the region. Following this the pathology of the head and neck shall be discussed with emphasis on basal and squamous cell carcinomas. In conclusion a brief exposition upon the treatment of basal and squamous cell carcinomas shall be presented.

2.1 Anatomy and Physiology of the Head and Neck

The principle interest in this thesis is that of the deposition of dose within the anatomy associated with the area of the head and neck. The reason why this is of interest is that the sloping surfaces and many different density interfaces create problems for typical dose distribution determining algorithms as shall be discussed in chapter 3. However,

[1]The number of patients undergoing procedures to remove basal and squamous cell carcinomas are extremely problematic to obtain. Even though BCCs and SCCs are often quoted as the most common cancer in countries containing a majority of fair-skinned people in the population little information is kept in official records to indicate exact numbers as BCCs and SCCs are exempt from reporting and many treatments are done without an associated biopsy. This is due to the majority of treatments occurring on an outpatient basis with no hospitalisation required. It would be possible to construct an indication of the numbers through an analysis of histology laboratory results and Ministry of Health Statistics but this shall not be attempted within the confines of this thesis.

Monte Carlo techniques provide an extremely powerful method for determining dose distributions in such complex geometries. The head and neck is further complicated by the characteristics of dose deposition by different particles of different energies within the various structures of the area; such as preferential absorption of dose in higher density structures (*i.e.* bone and cartilage as well as lead or tungsten shielding) relative to tissue for superficial photons and the presence of air filled cavities with concomitant build up and build down effects for MeV electrons.

As shall be detailed in the present section the various areas likely to be irradiated in the treatment of superficial cancers are complex in the nature of their geometry. By complex it is meant that the usual method by which dose deposition is studied (planar beams incident normally to an homogeneous isotropic water equivalent substance) does not correlate well with physical reality.

The head and neck area consists of many different biological systems that contribute towards maintaining homeostasis in the body. Each of these systems presents different considerations that one must make in the direct or scattered irradiation of the structures associated with it. It is beyond the scope of the current thesis to detail all of the biological systems located in the head and neck that may be affected by radiation. Hence, regions that shall be considered for discussion of their gross anatomical features and physiology are those that are located in the sites to be investigated in chapter 7, *i.e.* the eye, ear and nose.

The eye is a complex arrangement of accessory structures and specialised nerve tissue (see figure 2.1). It has a number of radiosensitive structures embedded in it and surrounding it that contribute to normal tissue complications during radiotherapy. The accessory structures are the eyelids, eyelashes, lacrimal apparatus and the extrinsic eye muscles. Of the accessory structures the eyelids and eyelashes protect the eye from excessive sunlight and foreign bodies. The lacrimal apparatus provides a means of cleansing, lubricating and protecting the eyeball. The lacrimal apparatus consists of a lacrimal gland the sits superior to the upper eyelid and drains across the eye (spread additionally by blinking of the eyelids) into lacrimal sacs inferior to the inferior nasal concha. The extrinsic eye muscles control smooth, precise and rapid movement of the eye.

The eyeball consists of a fibrous and vascular tunic, the retina, lens, anterior cavity and vitreous chamber. Each of these structures is of interest in the present thesis however the lens is the most sensitive to radiation damage (see table 2.1). Typically cataract surgery to repair any radiation induced damage to the lens is considered an effective treatment hence irradiation of the area can exceed the lens tolerance in certain instances.

The ear is not only the primary means of detecting sound but is also a means by which the body can detect orientation and hence maintain balance. The ear is divided into three main regions: the external, middle and internal ear (see figure 2.2). The external ear consists of the auricle, external auditory canal and eardrum. The auricle is a skin covered portion of elastic cartilage. The external auditory canal is a tube of approximately 25 mm length containing ceruminous glands that secrete cerumen (ear wax) thus prevent dust and the like from entering the ear. The eardrum is a thin, simple cuboidal epithelial layered membrane separating the external ear from the middle ear. The middle ear is an air filled cavity containing the auditory ossicles: the malleus, incus and stapes. The anterior wall of the middle ear has an opening that leads to the Eustachian tube, connecting the middle ear with the nasopharynx. The inner ear is an intricate arrangement of canals containing the cochlea, which houses the receptors for hearing.

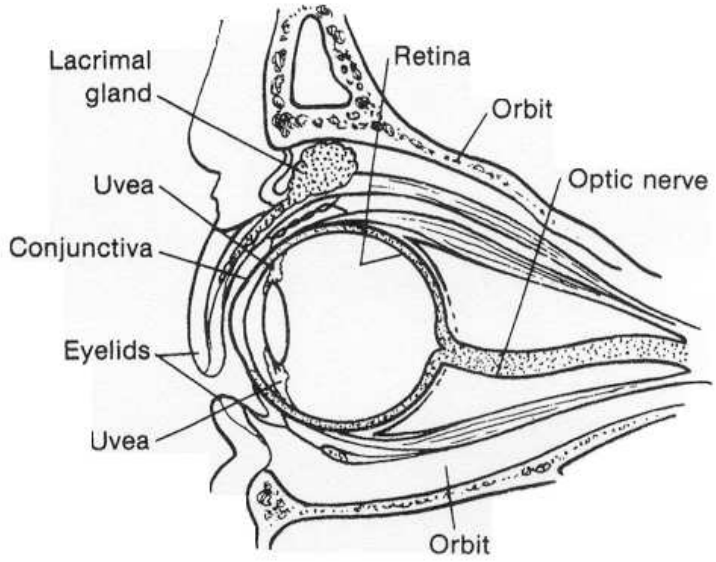

Figure 2.1: Sagittal cross section of the eye [Reproduced from [5]]

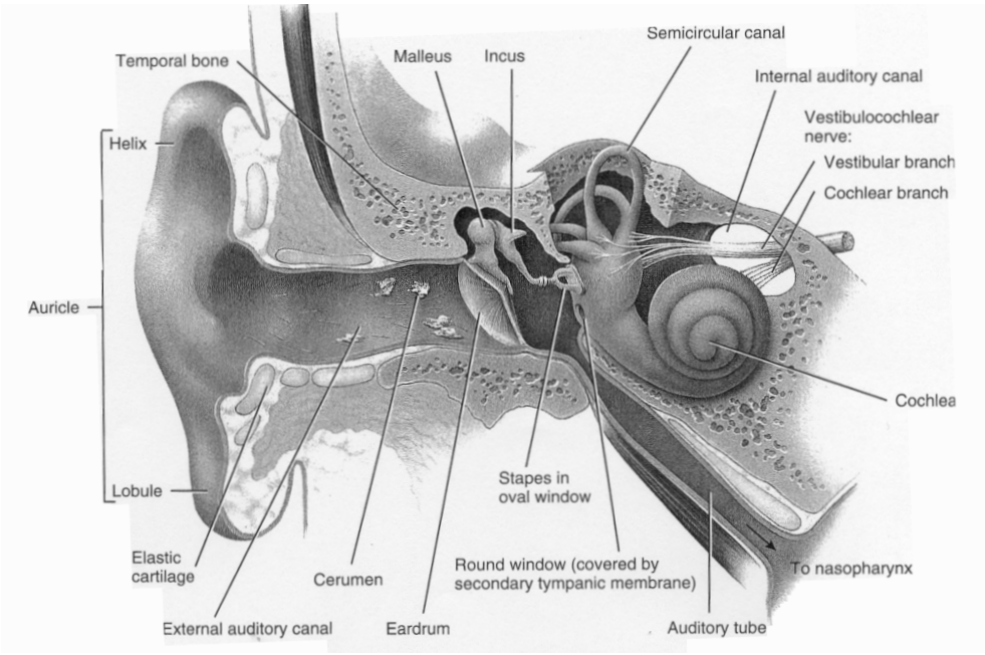

Figure 2.2: Frontal section through the right side of the skull showing gross anatomy of the ear [Reproduced from [6]]

The nose can be divided into two portions - an external portion and an internal portion. The external portion is a framework of bone and cartilage covered with skin and muscle. This provides support for the external nares. The internal nose allows for warming,

filtering and moistening inhaled air. The space within the internal nose is called the nasal cavity and consists of a vertically partitioned space constructed from cartilage and the vomer, ethmoid, maxillae and palatine bones (see figure 2.3). The space contains coarse hairs to remove large particles, mucous membranes and houses the sensory receptors for olfaction.

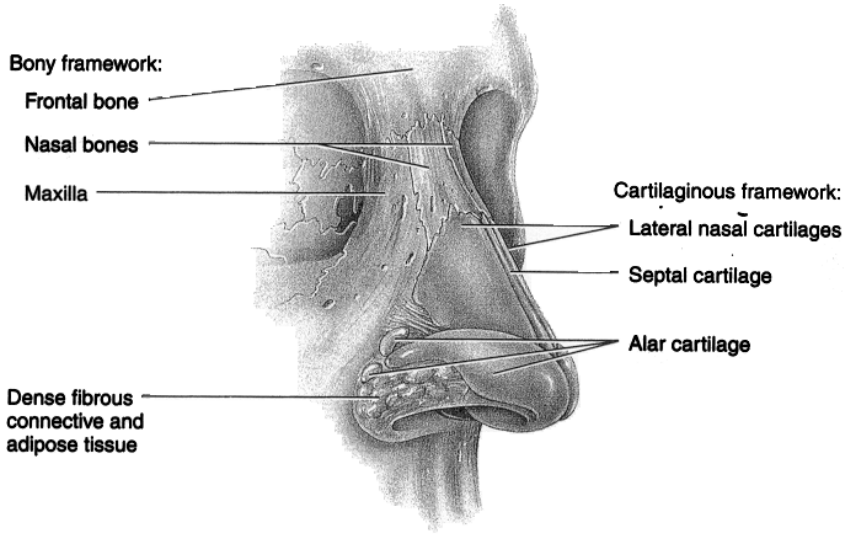

Figure 2.3: Anterolateral view of external portion of nose showing cartilaginous and bony structures [Reproduced from [6]]

The ICRP releases reports on the effects of dose in terms of injury at five years (see table 2.1) for certain percentages of a population irradiated within a particular body organ. Even though this list is by no means exhaustive it provides nonetheless an indication of the normal tissue complications that may arise in the irradiation of the head and neck region. It should also be noted that such a table is an indication only as to the potential amount of radiation required to produce the stated injury. The table represents extrapolation and retrospective analysis of data from a host of sources including radiation accidents and medical interventions.

2.2 Pathology of the Head and Neck

There are many neoplastic conditions of the head and neck region. It is beyond the scope and intent of this thesis to summarise all of the possible neoplastic conditions hence the focus shall be on cancers of the skin in the head and neck region. Such cancers present difficulties in treatment in that it is desirable to shield underlying structures from irradiation of an overlying tumour. There are many means by which one can mitigate radiation damage to normal tissue in the treated volume which shall be the focus of later chapters.

In terms of neoplastic skin conditions these may be classed as basal cell or squamous cell carcinomas (cancers arising in the basal and squamous cells of the epidermis), melanomas (cancers arising in the melanocytes of the epidermis), see figure 2.4. There

Organ	Injury at 5 years	Dose Causing Effect in 1-5% of Patients	Dose Causing Effect in 25-50% of Patients	Irradiation Field (Area)
Skin	Ulcer, severe fibrosis	55	70	100 cm^2
Oral mucosa	Ulcer, severe fibrosis	60	75	50 cm^2
Salivary glands	Xerostomia	50	70	50 cm^2
Capillaries	Telangiectasis, sclerosis	50–60	70–100	–
Bone, child	Arrested growth	10	30	10 cm^2
Bone, adult	Necrosis, fracture	60	150	10 cm^2
Cartilage, child	Arrested growth	10	30	whole
Cartilage, adult	Necrosis	60	100	whole
CNS (brain)	Necrosis	50	>60	whole
Spinal cord	Necrosis, transection	50	>60	5 cm^2
Eye	Panophthalmitis, hemorrhage	55	100	whole
Cornea	Keratitis	50	>60	whole
Lens	Cataract	5	12	whole
Ear (inner)	Deafness	>60		whole
Vestibulum auris	Menière's	60	100	whole
Thyroid	Hypothyroidism	45	150	whole
Pituitary	Hypopituitarism	45	200–300	whole
Muscle, child	Hypoplasia	20–30	40–50	whole
Muscle, adult	Atrophy	>100		whole
Lymph nodes	Atrophy	35–45	>70	–
Lymphatics	Sclerosis	50	>80	–

Table 2.1: Estimates of approximate threshold doses for clinically detrimental nonstochastic effects in tissues associated with the head and neck region [Reproduced from ICRP Publication 41[7]].

shall be no further discussion on melanoma as this condition is not conducive to the present investigation.

2.2.1 Basal and Squamous Cell Carcinomas

The focus of this thesis will be the treatment of basal and squamous cell carcinomas. Basal cell carcinoma is the most frequent type of skin cancer in fair skinned people; it outnumbers the second most common form of skin cancer, squamous cell carcinoma, by a ratio of 3:1 [8]. There are many different causes of basal and squamous cell carcinomas of which exposure to ultraviolet light probably ranks as being the most common; especially in New Zealand due to the depletion of the ozone layer in the Southern Hemisphere. Typically populations in latitudes distant from the equator are protected from excessive ultraviolet light by the increased thickness of ozone that an obliquely incident photon must traverse before being able to irradiate any person. However, in New Zealand, the apparent lack of protective ozone layer in the atmosphere coupled with the high proportion of fair skinned people of Irish, Scottish and English descent whom have red or light coloured

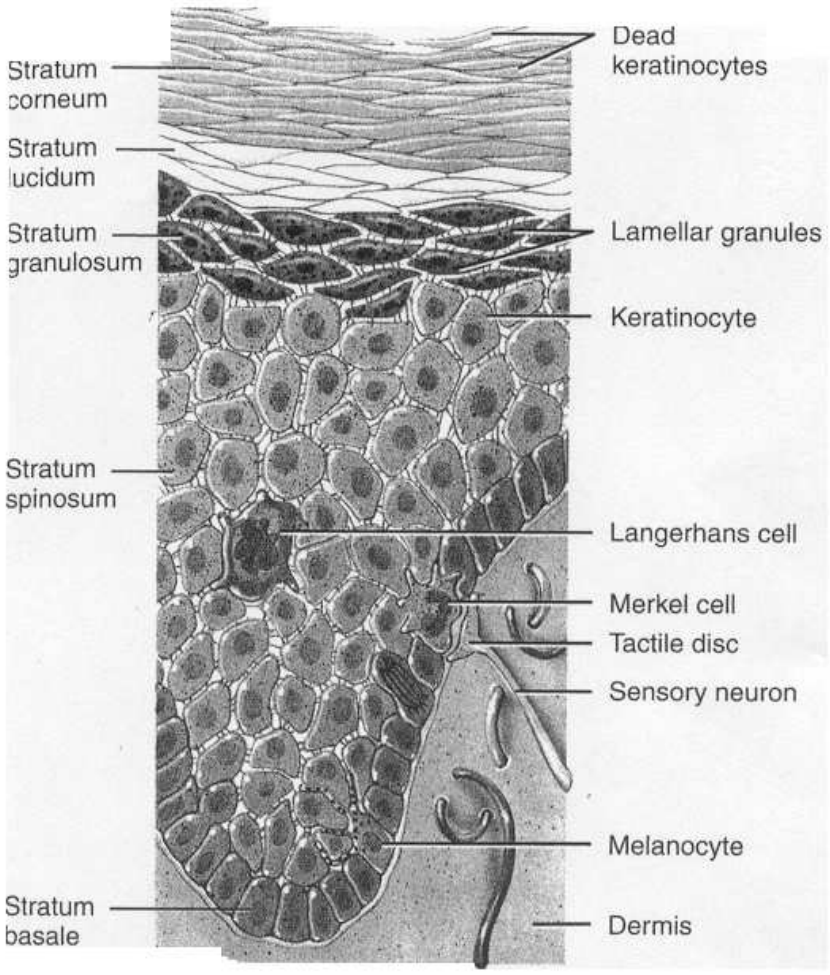

Figure 2.4: Layers of the epidermis [Reproduced from [6]]

hair, blue or green eyes and white skin that freckles indicates a high susceptibility to BCCs and SCCs.

BCCs and SCCs typically occur on the sun exposed surfaces of the body (*e.g.* the back of the hands or the head and neck). Individuals with outdoor occupations or recreational pursuits that involve long periods in sunlight are more prone to developing BCCs and SCCs. This is supported by evidence from a study by Urbach [9] in which ultraviolet light dosimeters were placed on a mannequin and sites which received high doses corresponded to sites in which patients would present with BCC and SCC.

Exposure to chemical and viral carcinogens can also lead to the formation of BCC and SCC. Arsenic is a well known chemical carcinogen and occupational or medical exposure to arsenic predispose an individual to the development of skin cancers as well as arsenical keratoses. Human papilloma viruses, though most commonly found in benign lesions, appears to be potentially oncogenic in humans [8]. A certain combination of factors is probably required to instigate a carcinoma such as exposure to ultra violet light and a decrease in cell mediated immunity along with presence of the virus.

Inappropriate exposure to ionising radiation has historically been shown to induce

chronic radiodermatitis and cancer. There are reports in the early literature that detail the effects of fractionation and overexposure for medically and occupationally exposed individuals respectively[8]. Such radiation induced cancers are rare currently due to accurate calibration of therapy units, fractionation and modern radiation protection practice.

Chronic irritation or inflammation can lead to the development of cancerous lesions. One of the more common cases is in burn victims whom develop aggressive ulcerating squamous cell carcinomas in the burn scar. Other types of infection that can lead to malignant lesions are osteomyelitis, decubitus ulcers and skin areas affected by lupus erythematosus. Additionally it has been shown that the chewing of tobacco can predispose the individual to chronic irritation and neoplasia causing squamous cell carcinomas of the lip and oral cavity.

Immune system function that is defective can lead to the development of malignant cutaneous neoplasms. This is strongly related to those individuals whom undertake immunosuppressive therapy after organ transplantation or for chemotherapy. Such neoplasms tend to be aggressive and have multiple lesions.

Basal Cell Carcinoma

Basal cell carcinoma is a malignant, locally invasive, epidermal skin tumour. BCC arises in the basal cell layers of the epidermis. The majority of people presenting with BCC are above the age of 40 years. BCCs develop typically on hair bearing, sun exposed skin with 85% found on the head and neck area. Pruritus and bleeding are common symptoms, typically the lesion will heal partially and ulcerate again. The frequency of BCC is not isolated in that 36% of individuals whom present with a BCC will develop a second within 5 years.

There are various tumour subtypes including nodular, cystic, ulcerated, superficial, morphoeic (sclerosing), keratotic and pigmented variants. The most common type is the nodulo-ulcerative type that emerges as a flesh coloured, waxy papulae with prominent surface telangiectasias. As the lesion grows ulceration of the central region may occur. Superficial BCCs occur commonly on the trunk and present as ill-defined red scaly macules. Such superficial BCCs increase in size to form crusted, occasionally ulcerated, scaly erythematous patches. Morphoeic BCCs appear as single off-white indurated macules. As morphoeic lesions increase in size they can become depressed.

The behaviour of the BCCs depends upon the tumour type. Each may grow slowly over a number of years with superficial type lesions gradually developing into nodulo-ulcerative type. The nodulo-ulcerative type invades locally by peripheral and deep extension, especially along nerve sheaths. Ulceration may be extensive with secondary bacterial infection and possible organ destruction. Morphoeic BCC is more aggressive and difficult to treat because of indistinct lateral margins and deep infiltration.

BCC metastasizes in only 0.0028% of cases as recorded in Australia and New Zealand by Paver *et al.*[10]. Primary tumours that metastasize are typically located on the head and neck. These are large, locally invasive and recurrent. Mean survival times after diagnosis of metastatic BCC is one year. Dissemination of the neoplasms occurs via the lymphatic system and veins. Hence most metastases are found in regional lymph nodes (68%), but 20% of the time the bone, lung and liver are involved.

Squamous Cell Carcinoma

Squamous cell carcinoma is a neoplastic condition of the skin that arises in the keratinocytes. SCC commonly develops from sun damaged skin or occasionally from existing cutaneous lesions (such as radiodermatitis, small pox vaccination scar, chronic osteomyelitis and burn scars). SCC may remain dormant for many years or may evolve in to a plaque stage with the concomitant development of ulceration, scaly crust and verrucous or papillated surface. This eventually becomes an infiltrating SCC that is endophytic erythematous ulcerated and with a nodular border. Such an advanced SCC grows along the subcutis, muscle, periosteum, along nerves and invades blood and lymphatic vessels.

SCC may metastasize to regional lymph nodes and eventually to distant sites such as bone, brain and lungs. Metastasis depends upon a number of factors including anatomical site, duration and size of lesion, depth of dermal invasion and degree of differentiation of the SCC. The biologic behaviour of neoplasms correlates well with the level of dermal invasion and vertical tumour thickness. Lesions that cause death are at least 10 mm thick and lesions with less differentiation have a greater chance of recurrence. SCC arising from normal skin are more aggressive than those arising from sun damaged skin.

Epstein *et al.*[8] noted that 2% of patients presenting with SCC developed metastatic disease. Of that proportion the metastatic involvement was noted in 2.5% of the cases within 1 month of appearance of the primary lesion, 40% by 6 months and 70% within a year. Survival reflects the aggressiveness of the neoplasms. Only 25% of patients with metastatic disease were alive after 5 years, 13% at 10 years and 8% at 15 years.

2.3 Treatment of Superficial Cancers

Although this thesis will focus upon radiotherapy in terms of the treatment of superficial cancers it should be recognised that this is not the only or most common form of treatment available. Details of the other techniques used, some of which may be used in conjunction with radiotherapy, shall be presented. Table 2.2 summarises the applicability of the various techniques associated with the treatment of primary (previously untreated) BCCs. This should not be confused with the treatment options for a recurrent BCC, however, what is of note with the table is the comparison of the suitability of radiotherapy in comparison to the other treatment techniques.

2.3.1 Radiotherapy

The focus of the thesis shall be radiotherapy as a non-surgical technique for the treatment of BCCs and SCCs. Additionally the comparison between the dose distributions associated with mega-voltage electron beams and kilo-voltage photon beams shall be investigated. Such a comparison will highlight differences in dose distributions like the preferential deposition of dose via the photoelectric effect in the relatively higher density tissues of the ear for kV photons with respect to MeV electrons. This shall be covered in the later chapter (see chapter 5) on the physics of photons and electrons.

During radiotherapy the accessory structures of the skin can be damaged from irradiation of superficial tumours. However, such damage (e.g epilation and erythema) is mostly cosmetic in nature and rarely leads to complications that require ongoing care. Complications from higher doses are moist desquamation and ulceration of the epider-

mis. For skin overlying avascular regions (such as the septum of the nose or auricle of the ear) any ulceration can lead to a chronic condition as there is poor blood supply to facilitate healing of the epidermal layers. Although any skin directly overlying bone has the propensity to ulcerate (*e.g.* the scalp) a favourable prognosis is more likely due to the abundant blood supply to the region.

A brief overview of the properties of the superficial photon and mega-voltage electron beams that lend themselves to consideration during any treatment planning process is given below. Full detail of the properties of such beams can be found radiation therapy textbooks, see for example Khan[3].

Superficial Photons

The benefits of using superficial photons is that the depth of dose maximum is, for all practical purposes, at the surface. Hence for superficial lesions overlying radiosensitive structures the primary concern can be with shielding the deep layers while irradiating the overlying tissue. Additionally penumbral effects are minimal for the photon fields in comparison to electrons.

Mega-voltage Electrons

Electrons in comparison to photons have a much shorter range and hence can be employed when underlying structures are to be spared. The therapy machines that deliver electrons are isocentrically mounted and thus multiple fields can be applied in comparison to the single fields available on superficial units. Due to the shallow d_{max} skin sparing may become an issue but with the use of bolus this can be mitigated somewhat. Additionally, penumbral effects and bremsstrahlung can complicate electrons fields.

2.3.2 Other Treatment Modalities

In all cases radiotherapy is not the generally accepted treatment of choice and hence, when employing radiotherapy, the techniques of cryosurgery, surgical excision, curettage or Mohs' micrographic surgery (MMS) must first be deemed inappropriate or inadequate to guarantee an effective treatment.

Surgical techniques

Curettage and electrodesiccation (cautery) is a technique used for select low risk lesions, *i.e.* small, well-defined primary lesions with non-aggressive histology in non-critical sites. 5-year cure rates of up to 97% are possible using this technique. Recurrent or morphoeic tumours and tumours in facial sites such as the nose, naso-labial folds and around the eyes are not generally treated using this technique.

Cryosurgery is used to freeze and hence render non-viable the cells within a tumour. It is widely used to treat basal and squamous cell carcinomas that are either solitary or multitudinous. Curettage prior to cryosurgery may help to increase the cure rate in such treatments.

Excision with predetermined margins is the surgical removal of the tumour along with seemingly unaffected tissue so as to capture any occult spread. There is a vast amount

of literature on the process and theory behind the techniques employed during excision which shall not be discussed as it is of little relevance to the current investigation.

MMS is a highly accurate means of removal of cancerous lesions. Overall cure rates of 99% have been reported for primary BCCs in the literature using the MMS technique. MMS is a relatively specialised treatment that is expensive and time consuming when compared to other possible treatments.

Non-surgical techniques

Topical therapy is especially useful for low risk lesions on the trunk and lower limbs. Such therapy cannot be expected to eradicate invasive BCC or lesions with follicular involvement.

Chemotherapy has been employed in the treatment of patients suffering from metastatic BCC. This, however, is an extremely rare and rapidly fatal condition. It has also been used for patients with uncontrolled local disease.

Palliative therapy is employed for debilitated patients where aggressive treatment of the cancer would lead to risks from side effects of treatment. Thus palliative treatment can be seen as using simple debulking techniques (excision or curettage) or radiotherapy to gain local control and hence improve quality of life.

BCC histology	Topical therapy	Curettage	RT	Cryosurgery	Excision	MMS
Small and low risk sites						
Superficial	⋆⋆	⋆⋆⋆	⋆	⋆⋆⋆	⋆	×
Nodular	•	⋆⋆⋆	⋆	⋆⋆⋆	⋆⋆⋆⋆	×
Morphoeic	•	⋆⋆	⋆⋆	⋆⋆	⋆⋆⋆⋆	⋆
Large and low risk sites						
Superficial	⋆⋆	⋆⋆⋆	⋆⋆	⋆⋆⋆⋆	⋆⋆	⋆
Nodular	×	⋆⋆⋆	⋆⋆⋆	⋆⋆⋆	⋆⋆⋆⋆	⋆
Morphoeic	×	•	⋆⋆	⋆⋆	⋆⋆⋆⋆	⋆⋆⋆
Small and high risk sites						
Superficial	×	⋆⋆	⋆⋆⋆	⋆⋆⋆	⋆⋆⋆⋆	⋆⋆
Nodular	×	⋆⋆	⋆⋆⋆	⋆⋆⋆	⋆⋆⋆⋆	⋆⋆⋆
Morphoeic	×	•	⋆⋆	⋆⋆	⋆⋆⋆	⋆⋆⋆⋆
Large and high risk sites						
Superficial	×	•	⋆⋆⋆	⋆⋆	⋆⋆⋆	⋆⋆⋆
Nodular	×	×	⋆⋆⋆	⋆⋆	⋆⋆⋆	⋆⋆⋆⋆
Morphoeic	×	×	⋆⋆	×	⋆⋆	⋆⋆⋆⋆

Table 2.2: Evaluation of treatment techniques available for primary (previously untreated) basal cell carcinomas. [Legend: ⋆⋆⋆⋆ probable treatment technique of choice, ⋆⋆⋆ generally good choice of treatment technique, ⋆⋆ generally fair choice of treatment technique, ⋆ a reasonable choice of treatment technique though not often necessary, • generally poor choice of treatment technique, × treatment technique should probably not be used][Reproduced from [11]]

Chapter 3

Treatment Planning Systems

For an appreciation of the power of the Monte Carlo method for calculating dose distributions it is useful to consider the algorithms used by commercial treatment planning systems in calculating dose distributions. The following chapter outlines the photon and electron algorithms used by the CadPlan® treatment planning system from Varian Medical Systems [12]. This shall be contrasted with the Monte Carlo method in the following chapter and the means by which photon and electron interactions are incorporated into the Monte Carlo code in chapter 5. Although CadPlan® is not considered a recent treatment planning system there is no loss in generality of the comparison as the underlying algorithms used in calculating dose are broadly similar across treatment planning systems.

The concept of a pencil beam is used in the following chapter extensively in the algorithms for determining dose in either photon or electron fields. A pencil beam is a fractional part of an entire treatment field and it is by a process of summation of the pencil beams that cover the treatment field that the calculated dose distribution is determined.

3.1 Photon Field Calculations with Pencil Beam Convolution Model

In calculating dose distributions associated with photon fields a number of measured depth dose and profile curves are required by the treatment planning system. These fields for the purposes of this thesis can be treated as open fields but the treatment planning system needs additional information about wedged profiles for a full implementation of the photon treatment planning system within a typical radiation oncology clinic.

Dose to a point, P, within an open symmetric photon field can be calculated by:

$$DOSE(P) = DD(d) \times OA(x, y, d) \times CO \times CF \tag{3.1}$$

where $DD(d)$ is the depth dose value at some depth d, $OA(x, y, d)$ is the off-axis factor at a point (x, y) in a plane perpendicular to the beam central axis at depth d, CO is the correction factor for any surface obliquity and CF is the correction factor for tissue inhomogeneities. See figures 3.1 and 3.2.

The photon pencil beam model can be used to determine dose distributions in water-equivalent phantoms for a specific beam geometry defined by field shape and source to skin distance. Rectangular fields and irregular fields can be considered with the former requiring a regular photon beam model whereas the latter requires a pencil beam convolution model.

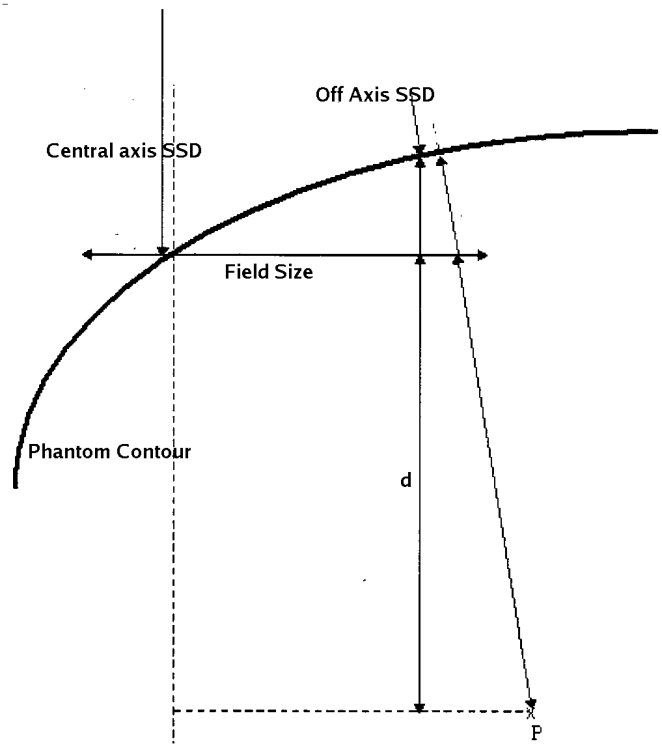

Figure 3.1: Distances used in dose calculations with a curved phantom surface [Reproduced from [12]]

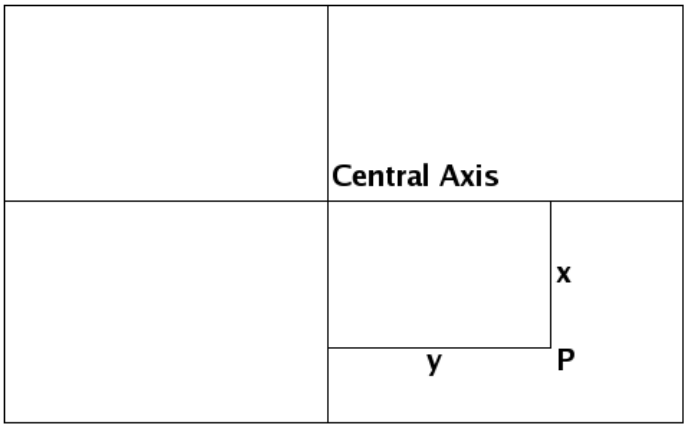

Figure 3.2: Field size geometry

3.1.1 Photon Pencil Beam Model

In the case of the irregular field the determination of off axis ratio, $OA(x, y, d)$ and depth dose, $DD(d)$, from equation 3.1 is based on the convolution of the field with pencil beam kernels for each separately. Depth dose is determined from depth doses of square fields

and peak scatter factors (PSF). Off axis ratio is determined from the boundary profile of a number of square fields. Each of these determinations are performed as if in water at the required distance with changes in source to skin distance (SSD) and skin obliquity factored in where necessary after dose has been calculated.

Irregular Fields

Irregular photon fields, as defined by a multileaf collimator (MLC) or shielding blocks, is projected along fanlines to the plane perpendicular to the beam axis at the required distance for dose calculation. In convolving the irregular field in dose calculation a two dimensional matrix is constructed at the perpendicular plane and populated with values in accordance with whether the beam in a particular matrix element is in an open portion of the field (hence a value of 1), outside of the collimating jaws (hence a value of 0) or in an area capable of receiving transmission or scattered radiation (hence an intermediate value between 0 and 1). The resolution of the matrix is arbitrary.

Depth Dose and Off Axis Factors

Depth dose can be expressed as:

$$DD(d, F) = DD_m(d, A_F) \times CF_{irreg}(d) \times CF_{dd}(d) \times CF_{inv} \tag{3.2}$$

where F is the irregular field, A_F is the equivalent square field, DD_m is the measured depth dose value and the correction factors CF_{irreg}, CF_{dd} and CF_{inv} correspond to the modification of the irregular field due to PSF, depth dose curve due to changed SSD and inverse square law respectively.

Off axis factors are more complicated in that the irregular field, F, has to be convolved with a boundary kernel to determine a two dimensional boundary profile object.

Dose Calculation

After substituting the modified elements into equation 3.1 there is another step in determining dose distribution in some phantom. This requires the modelling of the phantom itself; whereby phantom outline and inhomogeneities are considered. The pencil beam model detailed above only calculates the dose distribution as if in water. The major detraction from calculation of dose at this point is in the inhomogeneity correction factor determination. The inhomogeneity correction factor only takes into account electron density values of tissue ranging from air to bone. The requirement in the current investigation is that of being able to accurately model lead and tungsten in a field; hence the photon pencil beam model is insufficient for this purpose.

3.2 Electron Field Calculations with Generalised Gaussian Pencil Beam Algorithm

Electron beams are inherently more complex in terms of the calculation of dose. The high number of interactions that an electron undergoes in contrast to the photon by merit of the charged nature of the electron requires the use of a different algorithm to model the dose deposition characteristics. Additionally the bremsstrahlung photon contamination

in the electron field requires a separation of the field into two separate components for calculation along different lines. The generalised Gaussian pencil beam algorithm is used in this repsect.

The initial beam data required to utilise the generalised Gaussian pencil beam algorithm is a large field size depth dose curve. Other parameters that are also required are the virtual source to reference plane distance, mean electron scattering angle at the reference point and the mean electron energy at the phantom surface.

3.2.1 Electron Pencil Beam Model

Radial dose distributions, $D(r, z)$, are calculated in the generalised Gaussian pencil beam algorithm. Such dose distributions are calculated from weighted Gaussian distributions at a depth, z, and radial distance, r, from the axis of a pencil beam:

$$D(r,z) = \sum_{k=1}^{m} B_k(z) \exp\left(- \frac{r^2}{b_k(z)\bar{r}^2(z)} \right) \tag{3.3}$$

where B_k and b_k modulate the amplitude and width of the Gaussian distribution respectively, $\bar{r}$ is the mean radius of the beam. The dose to a point (see figure 3.3), (x, y, z), in a beam of incident field area, A, is given by:

$$D(x,y,z) = \frac{P(z) \sum_{k=1}^{m} B_k \iint_A S_{air}(x',y',z) \exp\left(- \frac{(x'-x)^2+(y'-y)^2}{b_k(z)\bar{r}^2(z)\rho(z)} \right) \mathrm{d}x'\mathrm{d}y'}{\pi \bar{r}^2(z)\rho(z) \sum_{k=1}^{m} B_k(z) b_k(z)} \tag{3.4}$$

where:

$$P(z) = P_0(z_{eff}) \left(\frac{s_{vir} + z_{eff}}{s_{vir} + z} \right)^2 \tag{3.5}$$

In equations 3.4 and 3.5 S_{air} is the fluence of the electron beam in air, $\rho(z)$ is an empirically determined factor to account for a particular behaviour of the electrons in a medium, $P_0(z)$ is the central axis depth dose curve of a field large enough so as not to be affected by changes in the periphery of the field, z_{eff} is the effective depth obtained from scaling the depth with inhomogeneities along the beam fanline and s_{vir} is the virtual source to reference plane distance. The concept of a virtual source is required as the electrons do not emanate from a point source.

The effective depth is calculated as:

$$z_{eff} = \sum_{i=1}^{n} (z_i - z_{i-1}) \frac{S_{tot,i}}{S_{tot,w}} \tag{3.6}$$

where $S_{tot,i}$ is the total stopping power of the material in the i^{th} layer of a phantom partitioned into n layers and $S_{tot,w}$ is the total stopping power of water.

The fluence in air term, S_{air} is assumed to be uniform over the entire field area. The effect on the fluence due to field shape is calculated in accordance with an angular variance term along the central axis of the fanline, $\sigma_\theta(0)$:

$$\sigma_\theta(0) = \sqrt{\frac{\bar{\theta}_0^2}{2}} \tag{3.7}$$

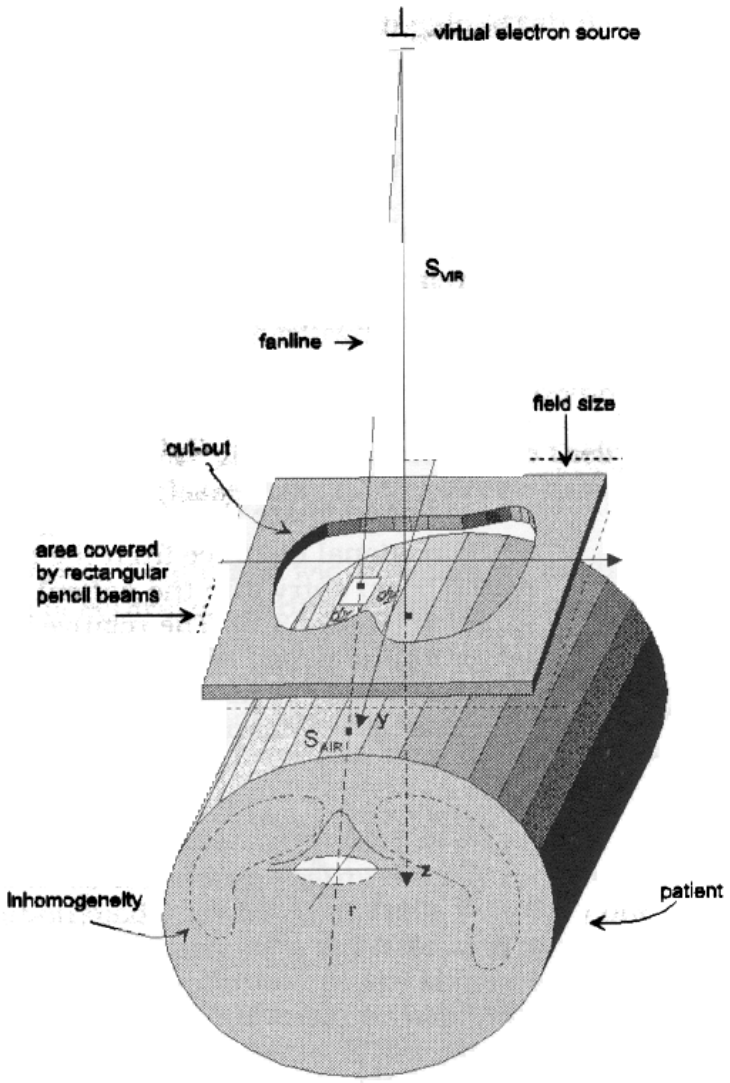

Figure 3.3: Geometry of the three dimensional generalised Gaussian pencil beam algorithm [Reproduced from [12]]

where the $\bar{\theta}_0^2$ term is the mean square scattering angle at the reference plane. The angular variance in air at a more general distance, z, from the reference plane can hence be calculated:

$$\sigma_\theta(z) = \sqrt{\sigma_\theta^2(0)z^2 + \frac{T_{air}}{6}z^3} \tag{3.8}$$

where T_{air} is the scattering power of air. The relative fluence in air, S_{air}, at the distance z_p where the pencil beam enters the phantom can be determined:

$$S_{air}(x, y, z_p) = \frac{1}{2}\left(\text{erf}\left(\frac{r_1(x, y, z_p}{\sigma_\theta(z_p)\sqrt{2}}\right) + \text{erf}\left(\frac{r_2(x, y, z_p}{\sigma_\theta(z_p)\sqrt{2}}\right)\right) \tag{3.9}$$

where r_1 and r_2 are the closest and next closest equilateral distances from the field edge at

the level of the pencil beam entry into the phantom (see figure 3.4). The relative fluence is used as a weighting factor for the pencil beam and accounts for irregular field shapes and the change in penumbra as a function of changed SSD.

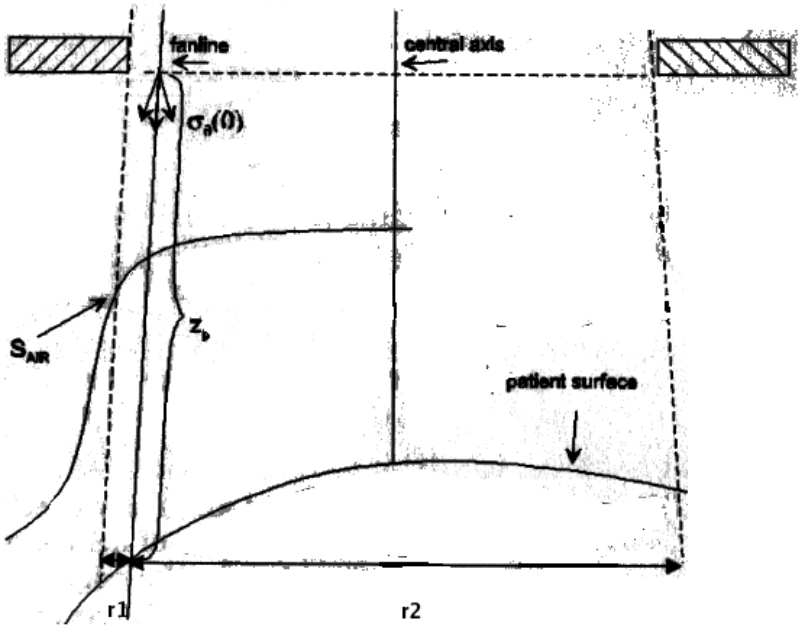

Figure 3.4: Distances used in calculation of fluence in air [Reproduced from [12]]

The scattering and stopping powers are listed in the algorithm for only five material types: air, lung, adipose tissue, muscle and bone. This therefore highlights one of the principle detractions from using the pencil beam algorithm in the current investigation as high atomic number materials such as tungsten and lead will be inserted into the treatment field. The limited nature by which it has been shown that the electron beam dose distributions are calculated in a typical treatment planning system algorithm is insufficient to cope with the added complexity in the treatment fields considered here.

Chapter 4

Monte Carlo Simulation Fundamentals

The Monte Carlo method is a mathematical technique whereby the random sampling of a population is undertaken so as to determine, within some level of confidence, an estimate of various characteristics of the population. The technique in itself is nothing recent having been used as early as 1777 to estimate values for π[13]. However the name "Monte Carlo" was not attached to the method until researchers at Los Alamos during work on the Manhattan Project named it as such. The current investigation relies upon the Monte Carlo method of simulating the transport of photons and electrons through a geometry representative of a patient. The present chapter will develop the background information that is relevant to detailing the Monte Carlo method for the purposes of understanding the differences of a Monte Carlo simulation over a calculation from algorithms detailed in the previous chapter.

The reason for using the Monte Carlo method is that it enables the obtaining of information about a physical situation without the limiting assumptions that must be used in algorithms like those used in the previous chapter. Whether there are convoluted geometries with indiscriminate interfaces between various media or high atomic number materials embedded in geometries there is no disadvantage in terms of the accuracy of an answer by using the Monte Carlo method. The one thing that is sacrificed in utilising the Monte Carlo method is that of time to complete the calculation. As shall be shown, electrons undergo an incredible number of interactions with surrounding media due to their charged nature, this leads to an enormous workload upon computational resources to undertake the calculation of required information about the physical situation. Thus, even though it may be feasible economically to instigate the Monte Carlo method in a clinical setting, the time to complete quite laborious simulations is measured in days and hours.

The power of the Monte Carlo method when applied to radiation transport rests upon two quite distinct principles. The first being that of the law of large numbers and the second being the probabilistic nature of the radiation interactions of various particles of different energies. From the apparently random phenomena of the interaction of radiation with matter the emergence of angular and spectral distributions are observed as the number of interactions simulated increases. Chapter 5 will elaborate further on the types of interactions that are observed in radiotherapy and shall detail the probability distributions or empirical formulas used to describe them.

4.1 Probability

Underlying the Monte Carlo method is the theory of probability. We need only a rudimentary grasp of the subject to be able to interpret Monte Carlo simulations hence the discussion shall be confined to detailing probability distribution functions and cumulative

probability distributions.

However, before beginning elementary probability theory the mathematical object that is central to all Monte Carlo simulations for radiation transport shall be discussed: the cross section. The reason for inserting this outside of the chapter upon radiation transport is that it provides the framework upon which to build the link between probability theory and the Monte Carlo method.

4.1.1 Cross Sections

Within particle physics there are three basic processes by which one can determine the structure and behaviour of a system; these are scattering interactions, decays and bound states. The latter two are of no concern in the present discussion. Cross sections are the important mathematical object in Monte Carlo simulations. However, as shall be shown, cross sections are nothing more than probability functions. The somewhat misleading nomenclature comes from the history of the parameter. It is considered that the area presented by a scattering centre to an incoming particle is the quantity of interest. Unfortunately this is as far as the conceptual framework of the macroscopic world ends and the abstract quantum world takes over. Particles do not present a "hit or miss" target to incoming particles but provide degrees of deflection to an incoming particle dependent upon proximity to the scattering centre. Additionally the cross section depends upon the nature of the incident particle and scattering centre; in this respect the currrent investigation is concerned only with photons and electrons incident upon atomic electrons and nuclei with the electromagnetic force being the mediator of the interaction. Finally the cross section depends upon the velocity of the incident particle.

Suppose that an incident particle encounters a stationary scattering centre and scatters at an angle θ. This scattering angle is a function of the initial radial distance from the scattering centre called the impact parameter, b. $\theta(b)$ depends upon the particular potential associated with the scattering centre; the present analysis depends upon the electromagnetic interaction hence an inverse square relationship would manifest itself in this respect. Additionally, if the incident particle was between b and $b + \mathrm{d}b$ the scattering will occur over the range of θ to $\theta + \mathrm{d}\theta$. To generalise further, if the incident particle passes through an infinitesimal area, $\mathrm{d}\sigma$, it will scatter into a corresponding solid angle, $\mathrm{d}\Omega$ (see figure 4.1). The proportionality factor between the relationship of $\mathrm{d}\sigma$ to $\mathrm{d}\Omega$ is called the differential scattering cross section and can be expressed mathematically as:

$$\mathrm{d}\sigma = D(\theta, \phi)\mathrm{d}\Omega \tag{4.1}$$

Azimuthal angle, ϕ, is included for completeness, however for the spherically symmetry electromagnetic interaction it plays no part. It should also be noted that this is strictly not a differential in the mathematical sense. The term differential is more applicable to the $\mathrm{d}\theta$ and $\mathrm{d}\Omega$ terms individually.

From figure 4.1 it can be determined that:

$$\mathrm{d}\sigma = |b\ \mathrm{d}b\ \mathrm{d}\phi| \qquad \mathrm{d}\Omega = |\sin\theta\ \mathrm{d}\theta\ \mathrm{d}\phi| \tag{4.2}$$

Hence:

$$D(\theta, \phi) = \frac{\mathrm{d}\sigma}{\mathrm{d}\Omega} = \left|\frac{b}{\sin\theta}\frac{\mathrm{d}b}{\mathrm{d}\theta}\right| \tag{4.3}$$

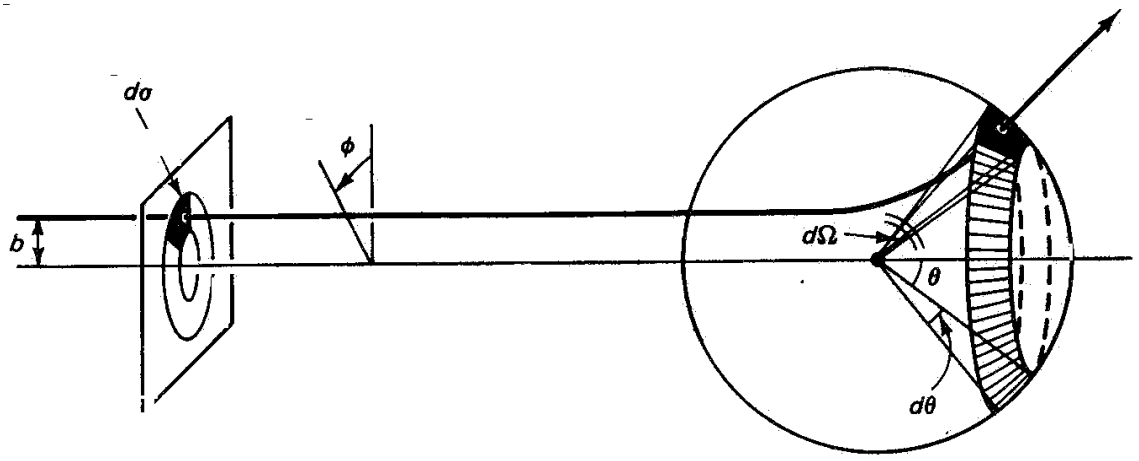

Figure 4.1: A particle is incident upon a scattering centre that passes through an infinitesimal area $\mathrm{d}\sigma$ at some azimuthal angle, ϕ and scatters into a solid angle, $\mathrm{d}\Omega$. [Reproduced form Griffiths pg. 193 [1]]

As shall be shown in the following chapter there are many different ways to express the fundamental concept of the cross section.

4.1.2 Probability Distribution Functions

Probability distribution functions provide a measure of the likelihood of an event occurring. Within the confines of the Monte Carlo method this provides an ideal means of correlating the mathematical machinery with stochastic physical processes such as the interaction of photons and electrons with matter. A probability distribution function, $p(x)$, has the following properties:

- $p(x) \geq 0$ (this property must exist as negative probabilities have no meaning[1])
- $\int_{x_{min}}^{x_{max}} p(x)dx = 1$ (provides for unitary normalisation)

An example of the sorts of probability distributions that are useful in radiation transport is the Cauchy or Lorentz distribution function:

$$p(x) = \frac{1}{\pi}\frac{\Gamma}{\Gamma^2 + x^2} \quad -\infty < x < \infty \tag{4.4}$$

arising from the intrinsic probability distribution of the energy of a quantum from an excited state atomic state of finite lifetime. For the purposes of illustration the more mundane normal distribution will be examined (see figure 4.2).

For the purposes of random sampling of the probability distribution function the cumulative probability distribution is constructed.

4.1.3 Cumulative Probability Distributions

The cumulative probability distribution, $c(x)$ (see figure 4.3), has the following properties:

- $p(x)$ and $c(x)$ are related by the derivative $p(x) = \frac{\mathrm{d}c(x)}{\mathrm{d}x}$

[1]This is not strictly true but within the present thesis it shall be taken as true.

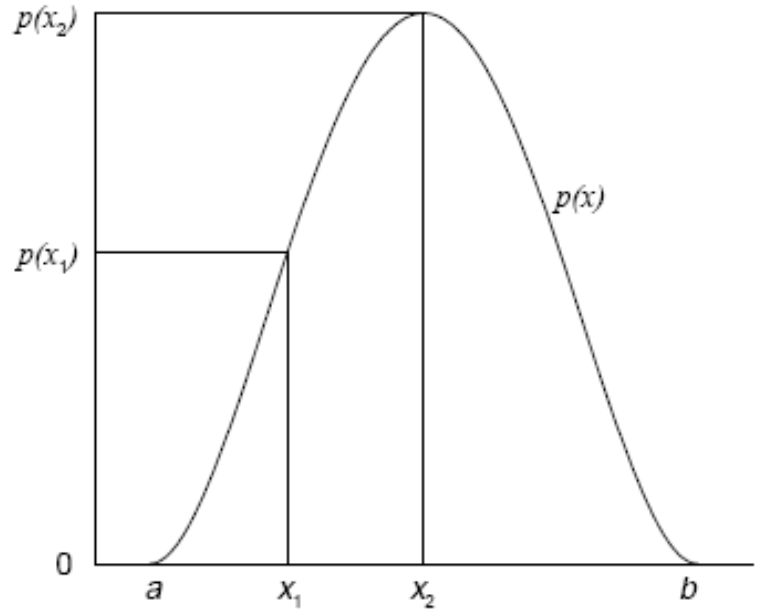

Figure 4.2: A normal probability distribution [Reproduced from [13]]

- $c(x_{min}) = 0$
- $c(x_{max}) = 1$
- $c(x)$ is a monotonically increasing function of x

The cumulative probability distribution function can be related to uniform random numbers to provide a means of sampling the probability distribution function.

4.2 Random Numbers

Random numbers are fundamental to the understanding of the Monte Carlo method. More accurately: "pseudo" random numbers are the fundamental building block of all Monte Carlo simulations. Such random numbers are necessary for generating the random nature of Monte Carlo simulations and hence mimicking the true stochastic nature of the physical system under consideration. The term "pseudo" is used as purely random numbers would make repeated runs and comparisons of simulations a difficult task, hence numbers that can be reproduced from the same initial conditions but appear random are used.

Random number generation in the Monte Carlo method needs to produce numbers of sufficient length and disorder so as to mitigate any structure that may be seen in the simulation. By structure it is meant the propensity for a simulation outcome to oscillate about a certain limiting value for example.

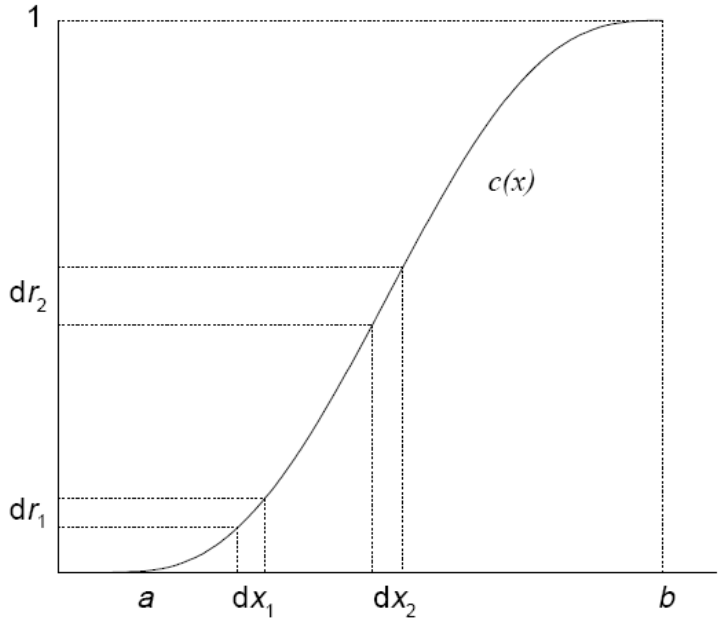

Figure 4.3: A cumulative probability distribution obtained from a normal probability distribution [Reproduced from [13]]

4.3 Sampling Theory

Random numbers are employed to sample the cumulative probability distribution detailed previously. The cumulative probability distribution can be mapped onto a range of random numbers, r, from 0 to 1. These r are uniformly distributed thus implying that $r = c(x)$. With reference to figure 4.3 consider two equally spaced intervals $\mathrm{d}x_1$ and $\mathrm{d}x_2$. It can be shown that:

$$\frac{\mathrm{d}r_1}{\mathrm{d}r_2} = \frac{p(x_1)}{p(x_2)} \tag{4.5}$$

This can be interpreted as that if many random variables on $[0, 1]$ are selected then the number that falls within $\mathrm{d}r_1$ divided by the number falling within $\mathrm{d}r_2$ is equal to the ratio of the probability distribution at x_1 to x_2. Mapping the random numbers onto the cumulative probability distribution function allows the inversion of the equation to yield:

$$x = c^{-1}(x) \tag{4.6}$$

Therefore, by choosing rs randomly over a uniform distribution and substituting them into equation 4.6, xs according to the proper probability distribution function can be generated.

4.4 Monte Carlo Method

Given some distribution of data points according to some function of one or more variables a determination of a property of the system to be modelled can be made. In the case of

the current investigation knowledge about the dose distributions in complex geometries is desired; also knowledge about particle histories, types of particle and errors associated with each is desired. The Monte Carlo method allows for error estimation and variance reduction techniques. Combined with a well defined means of transport through a geometry representative of the physical state modelled this provides sufficient information to extract the desired information. The computer system of codes used in the current investigation is the National Research Council of Canada'a (NRC) Ionizing Radiation Standard's groups implementation of the Monte Carlo method called EGSnrc.

The Monte Carlo method therefore is in contrast to the algorithmic methods detailed in the previous chapter in that no limiting assumptions are made in determining the dose distribution. Hence any geometry can be used and any material can be put in the treatment field provided that cross section data has been gathered for the material in question. The only limitation of the method is the encapsulation of the actual interaction of the particle traversing the phantom by physical theory and subsequent coding of the theory; and the number of particles that are considered in extracting information about the dose distribution. The more particles considered the more confidence in the final result is generated.

4.4.1 EGSnrc

EGSnrc (Electron Gamma Shower) system of codes is a general purpose package for the Monte Carlo simulation of coupled transport of electrons and photons in an arbitrary geometry for electrons and photons of radiotherapeutic energies (1keV to 50MeV). EGSnrc is based upon the the extended Fortran language Mortran. For a general description of EGSnrc see [14].

Chapter 5

Radiation Transport

The differences between the simulations of electrons and photons within the EGSnrc environment considered in the present investigation are important because simulation times and outcomes are tempered by the sorts of physics implemented for the energy regime under consideration. Photons and electrons interact with surrounding matter by a range of processes. The effective modelling of these interactive processes is the basis of a faithful Monte Carlo simulation of physical reality. Should a simulation be run that does not include the mechanism by which the majority of interactions proceeds or includes superfluous interactions then simulations will either become meaningless due to particles being excised needlessly from the simulation or particle interactions being followed for an inappropriate amount of CPU time without effect on the dose distribution. In the following chapter the interactions that are of concern to the simulations presented will be briefly presented.

5.1 Photon Interactions

The photon interactions that are of primary concern within this thesis are those processes which occur from 1 keV to 6 MeV. As such we will not be interested in any photonuclear reactions, which occur at the 10 MeV mark. Thus, pair production, Compton scattering, photoelectric absorption and Rayleigh scattering will be presented.

5.1.1 Pair Production

The Feynman diagram for pair production is given in figure 5.1. A photon interacts with the nucleus of an atom to produce a positron and electron. Triplet production can also occur if one of the atomic electrons receives sufficient energy to exceed the binding energy.

EGSnrc uses the cross section in the extreme relativistic first Born approximation differential cross sections as per Motz *et al.* [15]. This differential cross section is given in [14].

5.1.2 Compton Scattering

Incoherent, or Compton, scattering was observed by A. H. Compton in 1923 [1]. Compton observed that light scattered from a particle at rest is shifted in wavelength by $\lambda_c(1-\cos\theta)$, where λ_c is the so-called Compton wavelength of the target particle of some mass, m. This is expressed as:

$$\begin{aligned} \lambda' &= \lambda + \lambda_c(1-\cos\theta) \\ &= \lambda + \frac{h}{mc}(1-\cos\theta) \end{aligned} \tag{5.1}$$

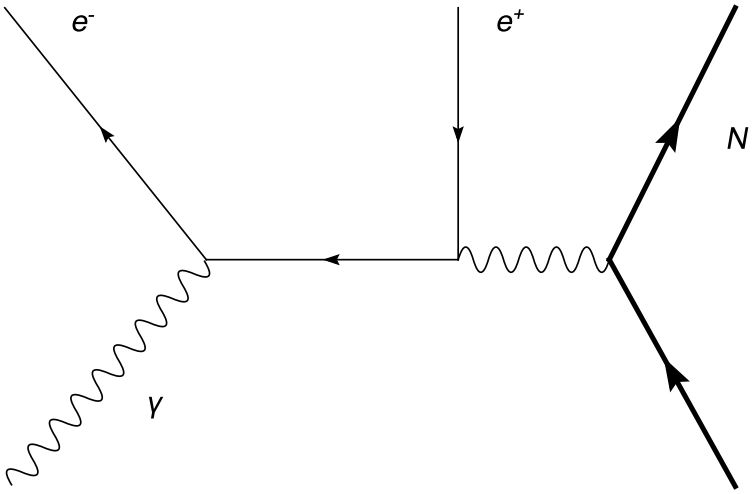

Figure 5.1: Feynman diagram demonstrating pair production in the field of a nucleus.

Figure 5.2 shows the Feynman diagram for Compton scattering. For some atom, **A**, that has an initially bound electron that interacts with the incoming photon to produce a free electron and lesser energy photon.

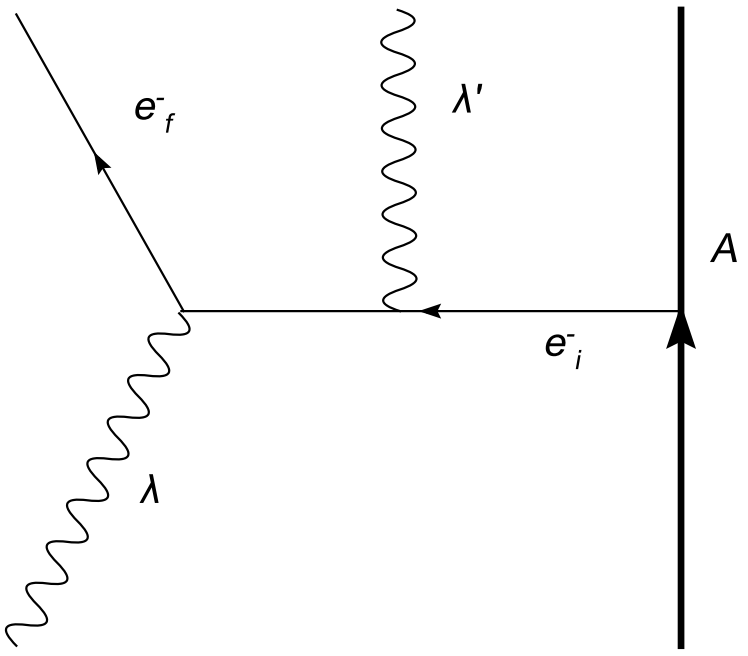

Figure 5.2: Feynman diagram demonstrating Compton scattering of a photon from an initially bound electron.

If the binding to the atom is neglected and the electron, e_i^-, is considered to be at rest, as is the usual convention when considering Compton scattering, the cross section for the process is given by the Klein-Nishina formula [14]:

$$\frac{\mathrm{d}\sigma_{KN}}{\mathrm{d}\cos\theta} = \pi r_0^2 Z X_{KN} \tag{5.2}$$

where θ is the polar angle of the scattered photon with respect to the incident photon, X_{KN} is a factor related to the energy and direction of the scattered photon and Z is the atomic number. The full differential cross section used in EGSnrc is given in [14].

5.1.3 Photoelectric Interaction

In photoelectric absorption a photon is absrobed by an atom resulting in the emission of an electron with an energy equal to the incident photon energy less the binding energy of the electron. This leaves an atom in an excited state which resumes the ground state by emission of fluorescent photons and Auger electrons. EGSnrc simulates the production of K_α and K_β fluorescent radiation with photon energies below the K-shell binding energy having their energy deposited locally and hence taking no part in further simulation.

5.1.4 Rayleigh Interaction

Coherent, or Rayleigh, scattering is useful in the present investigation due to the modelling of superficial X-ray units producing an abundance of photons and electrons below 1MeV. By default this is turned off in MeV energy simulations. The coherent scattering cross section, differential in the photon solid angle is:

$$\frac{\mathrm{d}\sigma_R}{\mathrm{d}\Omega} = \frac{r_0^2}{2}(1+\cos^2\theta)[F_T(q)]^2 \tag{5.3}$$

where θ is the scattering angle and $F_T(q)$ is an atomic form factor from Hubbel and Øverbø[14].

5.2 Electron Interactions

Monte Carlo methods are ideally suited to dealing with electron interactions as there are so many of them. Random sampling to project the picture of interaction is therefore a valid method in this respect. Additionally EGSnrc used a condensed history technique to allow for the multitude of electron interactions [16]. The cumulative effect of all collisions within a certain length of geometry are taken into account by sampling the energy and direction changes with respect to an appropriate scattering distribution. This is similar to the scattering distribution describing the pencil beam shape in the algorithms in the previous chapter except without the subsequent limiting approximations. This is justified for the energy regime under consideration in the current investigation due to the small change in electron state for single collisions.

5.2.1 Bremsstrahlung

Bremsstrahlung and pair production interactions are cross-symmetric in that the figure 5.1 describes the bremsstrahlung process by considering the incident photon and exiting positron lines in place of each other. In EGSnrc the full detail of the process is given in [14].

5.2.2 Inelastic Interactions

Within EGSnrc the two inelastic scattering processes of electron considered are electron-electron or Møller scattering and electron-positron or Bhabha scattering. Both cross sections are detailed in [14].

5.2.3 Elastic Interactions

In elastic scattering processes EGSnrc considers spin effects at the prompting of the user and hence is based on exact theory otherwise the screened Rutherford elastic scattering is used. In the present investigation spin effects are always considered.

5.2.4 Positron Electron Annihilation

The two photon positron annihilation process in EGSnrc is given by the cross section differential in energy of one of the annihilation photons, k:

$$\frac{\mathrm{d}\sigma_{annih}}{\mathrm{d}k} = \frac{\pi r_0^2}{\tau(\tau+2)}[S_1(\kappa) + S_1(\tau+2-\kappa)] \tag{5.4}$$

where τ and κ are the positron kinetic energy and photon energy respectively and S_1 is a function of positron kinetic energy [14]. Single or three or more photon annihilations are possible in the nuclear field, although the probability is very small for the energy regime considered in the present investigation.

In the following chapters the difference between the kV photon beam types of interactions (which are predominantly driven by a dependence on atomic number, Z) and MeV electron beam types of interactions (which are essential independent of Z) shall be referred to as photoelectric and Z-independent respectively.

Chapter 6

Modelling Accelerator Outputs with BEAMnrc

Monte Carlo simulations provide a measure of reality but do not necessarily reflect reality accurately as the Monte Carlo simulations are devoid of any physical contact with the devices being modelled. This thesis shall address this apparent disconnect by employing an iterative process to match the output of the Monte Carlo simulations with water phantom data[1]. By iterative process it is meant that comparisons of typical curves taken from water phantom measurements (*i.e.* depth dose, profile and isodose curves) are made for methodically altered beam parameters. Most notably the parameter that exerts the greatest influence on simulation outcome is the initial energy of the electron beam striking either the scattering foil in the linear accelerator or target in the x-ray tube. From these comparisons slight adjustments to the simulation parameters can be made so as to match the physical beams. The literature predominantly discusses linear accelerator simulations but the x-ray tube simulation arguments are equivalent.

The importance of the initial electron beam exiting the bending magnet assembly (see figure 6.1) in the head of the linac is discussed by Björk *et al.*[17]. They note that accelerator manufacturers rarely supply information on the geometric properties of their linac heads. This, however, is not the case in the current thesis as Varian Medical Systems supplied detailed plans of their Clinac® 2100C head design in exchange for signing a non-disclosure agreement (the essence of which will be discussed later in section 6.3). Björk *et al.* note that a Monte Carlo simulation should be reasonably expected to at least be able to reproduce a measured dose distribution to within ±2% or ±2mm depending upon whether a low or high dose gradient region is being modelled respectively.

The decision to model the entire head of the linear accelerator and x-ray tube was based upon Jiang *et al.*[18]. They discuss the acquisition of phase space data distinct from modelling the entire linear accelerator head with respect to commissioning an electron beam model for treatment planning; this is exactly the focus of the current thesis. It is noted that it would be impractical to develop a treatment planning system based upon individual linac treatment head designs and linac beam tunings. Jiang *et al.* develop a multiple source model that includes a point electron source for direct electrons and electrons scattered from the primary collimator, a point photon source for contaminant bremsstrahlung photons and two electron sources representing electrons scattered from the electron applicator scrappers. For the current thesis a less generic approach is required as the individual beam tuning, linac head and x-ray tube design will not be used to implement a wider treatment planning system. Plus the flexibility afforded in using a less generic means of determining phase space data allows for a greater understanding of the influence of various geometric and electron beam parameters.

Means of determining phase space data other than a trial and error method are dis-

[1]The water phantom used in the present investigation is the PTW MP3 Therapy Beam Analyzer. It is a computer-controlled measuring system for dose distribution and radiation analysis in radiotherapy

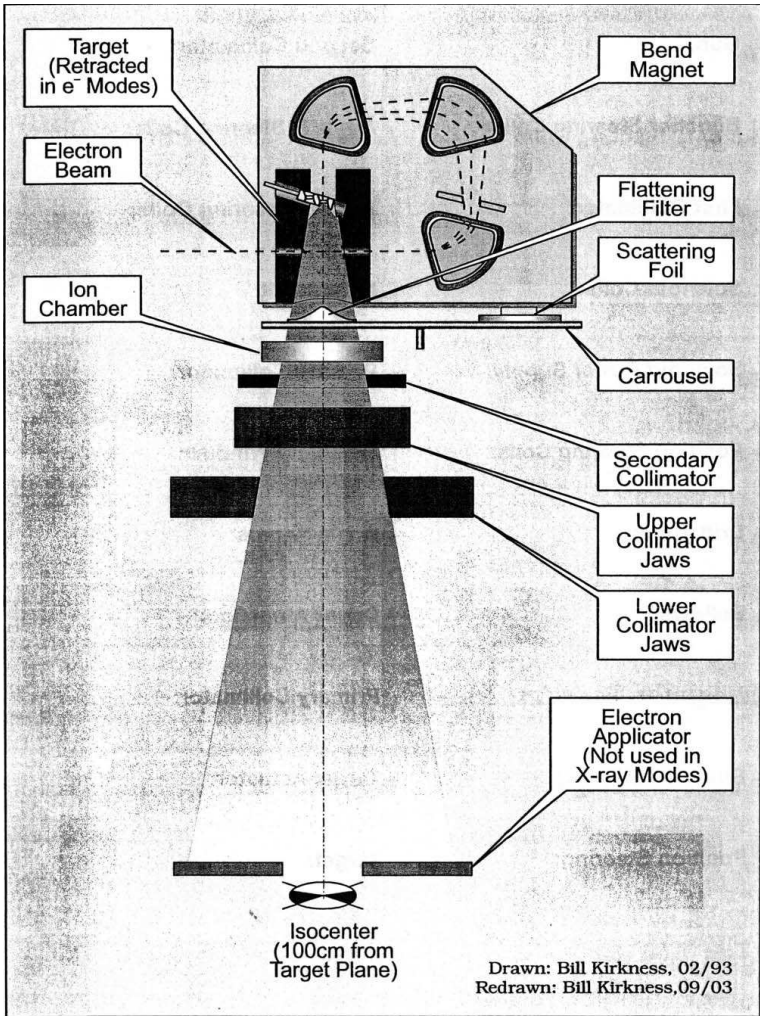

Figure 6.1: Schematic diagram of the beam definition system of a linear accelerator. [Reproduced from Varian Medical Systems High Energy C-series Clinac® Customer Support Course]

cussed by Aljarrah *et al.*[19]. They note that it is very time consuming and requires a lot of Monte Carlo simulation experience and computational resources. Several common cost functions were tested in their paper (notably dose difference at the penumbra edge and slope of the lateral profile) for comparing measured and simulated dose distributions. Ostensibly the paper avoids the issue of minimising the necessity of trail and error modelling by deferring some of the work onto the vendor of the linac. However, the worth of the paper is in the measures associated with comparing the simulated dose distribution which shall be implemented in the current thesis.

Verhaegen and Seuntjens [20] provide a topical review that addresses some of the specific issues that surround the modelling of superficial units. It is noted that accurate simulation of kilovoltage sources requires accurate low-energy electron and photon physics along with cross section data to be properly instigated in any code attempting such. The investigators used an EGS4/BEAM code to study a Philips MCN421 x-ray unit and found an overestimation of the low-energy component at the expense of the high-energy component in the simulated spectrum. The EGSnrc code has recently been extended to include electron impact ionisation (EII); therefore, a more realistic simulation of the x-ray

tube is to be expected in the current thesis.

The following chapter describes the process by which the Pantak Therapax SXT 150 and Varian Clinac® 2100C were modelled using BEAMnrc and matched to PTW MP3 water phantom and ionisation chamber data. Only three energies were considered in the current thesis (80 and 100 kV for the Pantak and 6 MeV for the Clinac®) as these were deemed the only clinically relevant energies for the superficial cancers being irradiated by means of Monte Carlo simulation.

6.1 BEAMnrc

The EGSnrc system of codes is an extremely useful tool in radiotherapy research. However, the labourious writing of `howfar`, `hownear` and `ausgab` subroutines for the user codes in simulating electron accelerators is a major hindrance (see [14] for details on the various subroutines associated with EGSnrc). This has been mitigated by the release of an extensive set of customisable component modules (CM) that represent the various components of the electron accelerator within a system of codes linked to EGSnrc called BEAMnrc. BEAMnrc was collaboratively developed by researchers at National Research Council of Canada (NRCC) and University of Wisconsin as part of the Ottawa Madison Electron Gamma Algorithm (OMEGA) project. Rogers *et al.*[4] describe the general purpose Monte Carlo code BEAM in detail including asymmetric geometrical specification of CMs, variance reduction techniques and particle history tracking. The Ionising Radiation Standards (IRS) unit of the NRCC has also released a user manual[21] that includes detailed instruction on using BEAMnrc.

The entire BEAMnrc system of codes includes programs for:

- building simulations of electron accelerators (BEAMnrc)
- determining dose in rectilinearly defined phantoms (DOSXYZnrc)
- processing data associated with electron accelerator simulations (BEAMDP)
- displaying isodose and phantom data (dosxyz_show)
- graphical user interfaces for each of the above programs
- importing and converting CT information into rectilinear phantoms for use in DOSXYZnrc simualtions

A schematic diagram of the system of codes is shown in figure 6.2. This highlights the modular structure of the system of codes. It is therefore possible for the end user to alter and recompile parts of the system of codes to suit local needs.

The result of a BEAMnrc simulation is a phase space file. This file contains, for each individual particle that crosses a user defined plane in the simulation, a host of information such as energy, position, direction and charge. It is also possible to tag particles to trace their origin and hence undertake investigations into the likes of scatter contributions to the field. From these phase space files (that can be as large as a few gigabytes) dosimetric simulations can be undertaken. The more particles in a phase space file the better the overall simulation statistics become, however the payoff is that the simulation takes a much longer time to complete.

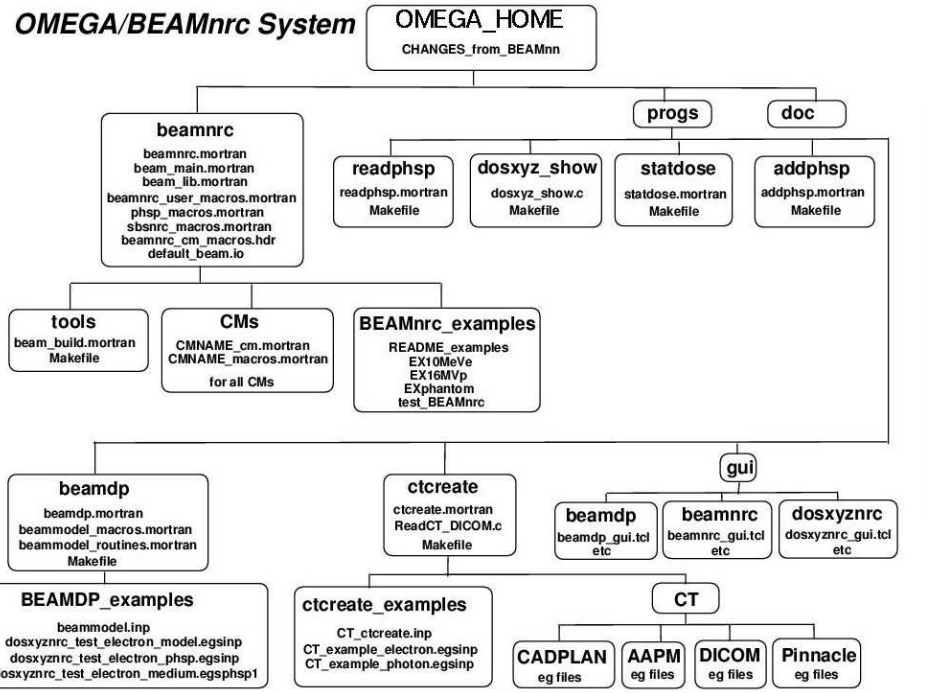

Figure 6.2: Schematic diagram of the main components of the OMEGA_HOME directory nested within the EGSnrc system of codes. [Reproduced from [21]]

Simulations of both a superficial unit and a megavoltage medical electron accelerator have been undertaken in the current thesis. Each simulation consisted of modelling an open accelerator/tube configuration (*i.e.* phase space data was collected at the respective exit windows of the accelerator/tube). In obtaining an open configuration phase space file it is then possible to add applicators and other beam modifiers and obtain a new phase space file at the new exit plane in a fraction of the time that it would take had the entire accelerator/tube configuration been simulated. By far the greatest amount of time was spent on obtaining a reasonable open configuration phase space file that agreed to within $\pm 2\%$ or ± 2mm depending upon whether a low or high dose gradient region was being modelled respectively [17].

6.2 kV Superficial X-Ray Unit

As previously stated, the aim of the current thesis is to explore optimisation of targeted dose distributions (*i.e.* a dose distribution satisfying constraints of a typical radiotherapy prescription) for superficial tumour irradiation. At the time of writing there are currently no commercially available treatment planning systems that create three dimensional dose distributions for superficial or orthovoltage units in radiotherapy [2]. Therefore the first

[2] Alaei *et al.*[22] do evaluate a model-based treatment planning system for kilovoltage energies. The investigation was based upon the ADAC Pinnacle treatment planning system. Although they found that the convolution/superposition based system was capable of computing dose within phantoms of approximate water density to a reasonable degree of accuracy, inaccuracies were prevalent in phantoms containing additional high atomic number materials.

step in being able to have confidence in a Monte Carlo simulation of a targeted dose distribution for superficial units the current thesis shall match a series of depth dose curves, profiles and isodose curves for a rectilinear water phantom.

Kilovoltage x-ray units have achieved a renewed interest in the literature (*e.g.* Verhaegen *et al.*[23]) which is attributable to the availability of open source Monte Carlo systems of code and general computing power available to clinical researchers. Accurate dose distributions from kilovoltage units is problematic in that the necessary information for specifying the beam (photon spectrum, planar fluence and angular distribution) cannot be empirically determined in a typical radiotherapy clinic. Previous empirical attempts to incorporate kilovoltage units in dosimetry protocols (*e.g.* BJR Supplement 25 [24]) have been prone to large systematic uncertainties being introduced. Thus Monte Carlo modelling is the only viable option for studying kilovoltage dose distributions in the current thesis.

Future applications are also driving the renewed interest in kilovoltage x-ray units. One such application is where advantage is taken of the preferential dose deposition in contrast enhanced tumour sites[25] due to the predominance in the energy spectrum of photoelectric absorption. Labelling a tumour with high atomic number contrast presents a number of issues that the method presented in this thesis can help solve. Obtaining accurate CT numbers and hence physical densities via CT scans to enable treatment planning would be very problematic in the presence of high atomic number contrast. However, chapter 7 demonstrates how to solve this problem. Another application is given by Li *et al.*[26] where an endocavitary rectal irradiator is discussed that utilises the Monte Carlo method extensively to ensure accurate dosimetry of delivered kilovoltage treatments.

Electron impact ionisation (EII) is a critical part of the code within EGSnrc in the accurate simulation of superficial units. Verhaegen *et al.*[23] note that even though EII is not explicitly modelled in earlier versions of EGS the influence on the calculated dosimetric quantities is minor. This noted, however, the EII option shall always be utilised in the simulations undertaken in the current thesis.

6.2.1 Pantak Therapax SXT 150 Geometry

The Pantak Therapax SXT 150 unit contains an MXR-161 X-ray tube and has differing diameter circular applicators that can be attached near the exit window of the tube. The geometric specifications of the tube and applicators were obtained from Gulmay Medical Ltd. through the offices of COMET AG, Herrengasse 10, 3175 Flamatt, Switzerland. Table 6.1 gives the specifications of the MXR-161 X-ray tube and figures 6.3 and 6.4 show tube and applicator system views of the geometry from the Gulmay Medical Ltd. technical drawings from which simulation models were derived.

6.2.2 BEAMnrc Parameters

BEAMnrc simulations access all of the relevant information from a user defined script file called an egsinp file. Contained within the egsinp file are the number of histories required per simulation, electron or photon source parameters, variance reduction techniques employed and geometry parameters of the various component modules. The egsinp files used in the current thesis initially simulate an open Pantak Therapax SXT 150 unit for both 80kV and 100kV energies. By open it is meant that the applicator is not explicitly

Nominal tube voltage	160kV
Continuous rating	3000W
Focal spot diameter	7.5mm
Filament current, max.	4.2A
Inherent filtration	0.8mm Be
Target material	W
Target angle	30°
Radiation coverage	40°
Leakage radiation, max.	1mSv/h

Table 6.1: MXR-161 unipolar metal ceramic x-ray tube specifications

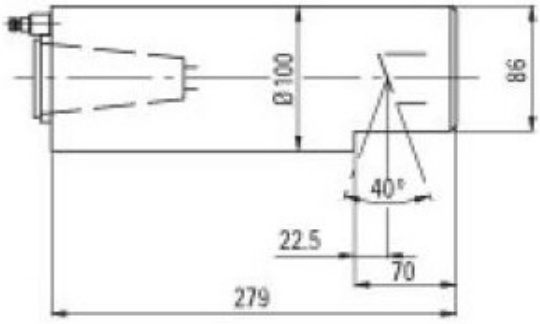

Figure 6.3: MXR-161 x-ray tube outline drawing (all dimensions are in mm) [Reproduced from Comet website http://www.feinfocus/com on 19-Dec-06]

modelled. The differing diameter applicators are modelled afterwards by using the phase space file generated in the open configuration as the source of photons and electrons at the entrance face of the applicator. Appendix A contains all of the egsinp files detailing the open configurations and applicators for both 80kV and 100kV simulations.

6.2.3 80 and 100 kV Simulations and Measurements

Simulations were undertaken for 5cm, 3cm and 1cm diameter circular applicators on the Pantak Therapax SXT 150 unit for both 80kV and 100kV energies. The result of the simulations are eight phase space files of approximately 0.5–1 GB representing each of the geometric and energy combinations. These phase space files are then used in the DOSXYZnrc code to create dose distributions in a water phantom (see section 7.2.1 for a fuller description of the DOSXYZnrc code). MATLAB® was then used to extract depth dose curves, profiles and midplane isodose curves from the resultant three dimensional dose distribution files.

Experimental water tank data was acquired to match against the simulation data. The PTW MP3 water phantom and PTW MEPHYSTO mc^2 software interface were used to extract data from the superficial photon beams. A PTW pinpoint chamber type 31015 was used as the field chamber with no reference used as the fields and set up could not accommodate such. A standoff had to be introduced due to the size of the chamber mount

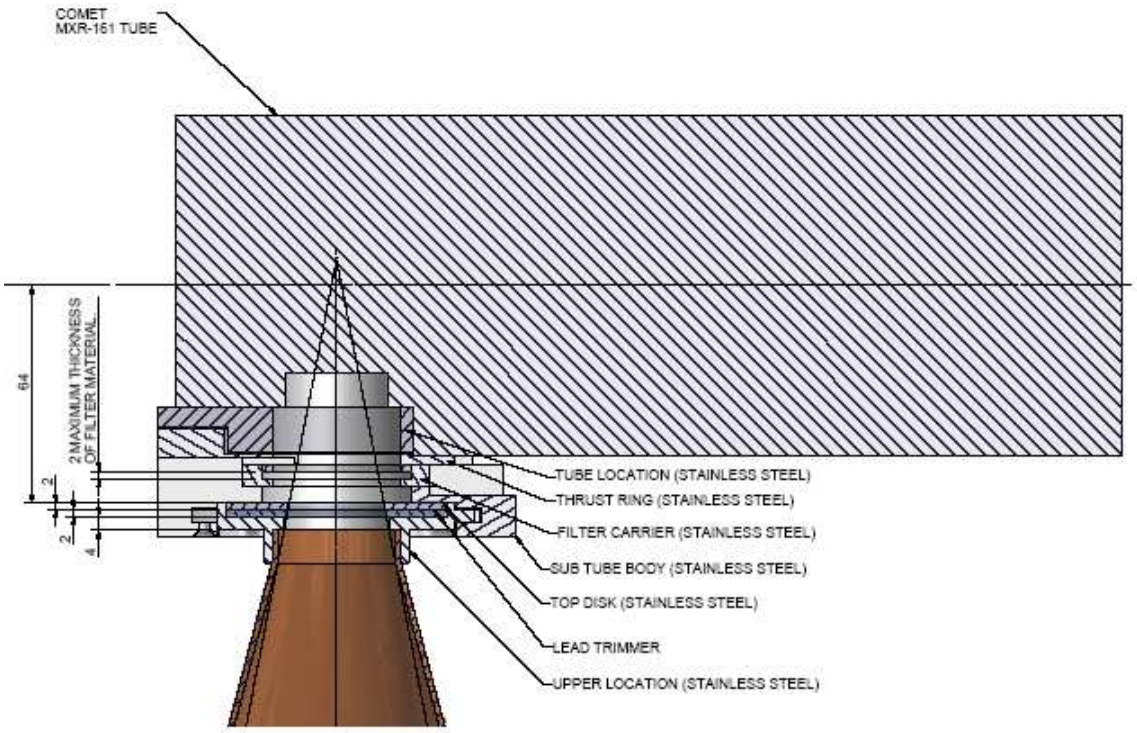

Figure 6.4: Midplane view of tube and applicator assembly for the MXR-161 x-ray tube and Pantak Therapax SXT 150 unit (all dimensions are in mm) [Image courtesy of Gulmay Medical Ltd.]

on the arm of the PTW MP3 water phantom colliding with the applicator cone exit face at water surface. This standoff was explicitly modelled in the Monte Carlo simulations as the distance from the source to isocentre in the egsinp files.

Any contribution from a heel effect on the anode of the Pantak Therapax SXT 150 unit was carefully considered by ensuring the planes from the simulation and water phantom data matched.

Spectral properties of beam will not be investigated here as Verhaegen *et al.*[23] note that explicit matching of the characteristic radiation does not afford a significant increase in the accuracy of the simulation. It shall be deemed sufficient that the simulation and water tank measurement agree within the ±2% or ±2mm stipulation of Björk *et al.*[17].

Depth Dose Curves

The following graphs show the depth dose curves associated with EGSnrc Monte Carlo simulation and PTW MP3 water phantom measurements for 80kV and 100kV photon beams from the Pantak Therapax SXT 150 unit for 5cm, 3cm and 1cm diameter applicator cones. The Monte Carlo simulations were taken from a water phantom constructed from 2mm voxels with a stand off material of air between the surface of the phantom and the phase space file source. The PTW MP3 water phantom measurements were performed bottom up so as to minimise any artifacts from near surface measurements. All scans are normalised to unity at a depth of 20mm.

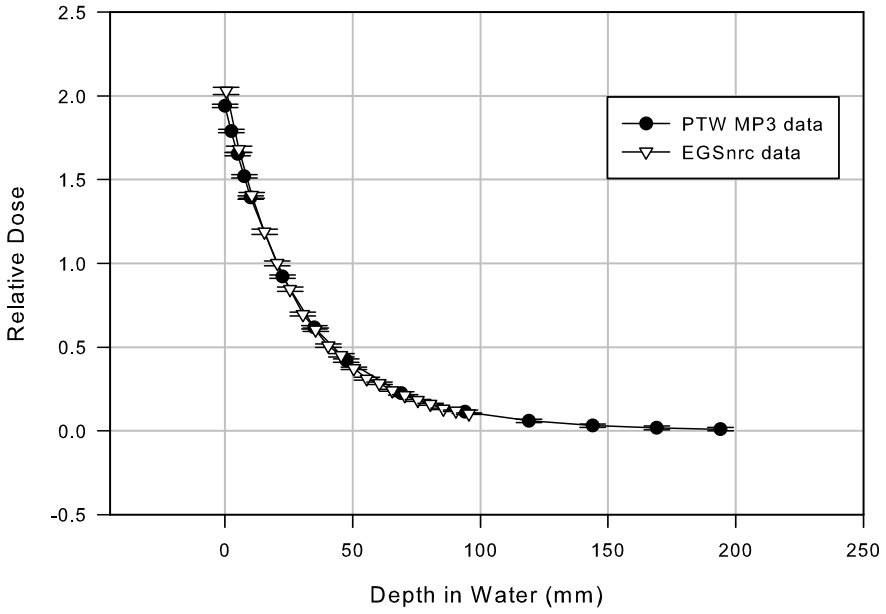

Figure 6.5: Depth dose curves for EGSnrc Monte Carlo simulation and PTW MP3 water phantom measurement of a Pantak Therapax SXT 150 unit 80kV photon beam with 5cm diameter circular applicator attached.

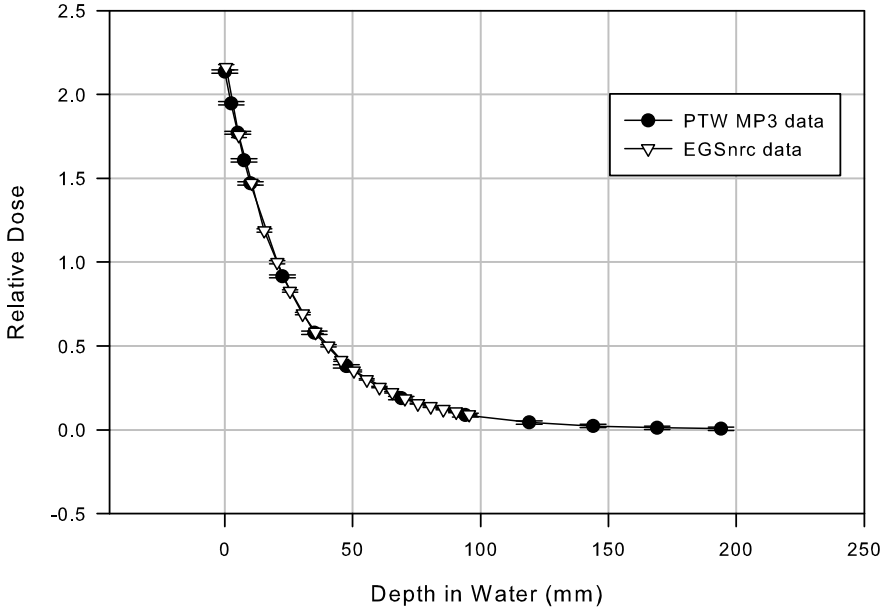

Figure 6.6: Depth dose curves for EGSnrc Monte Carlo simulation and PTW MP3 water phantom measurement of a Pantak Therapax SXT 150 unit 80kV photon beam with 3cm diameter circular applicator attached.

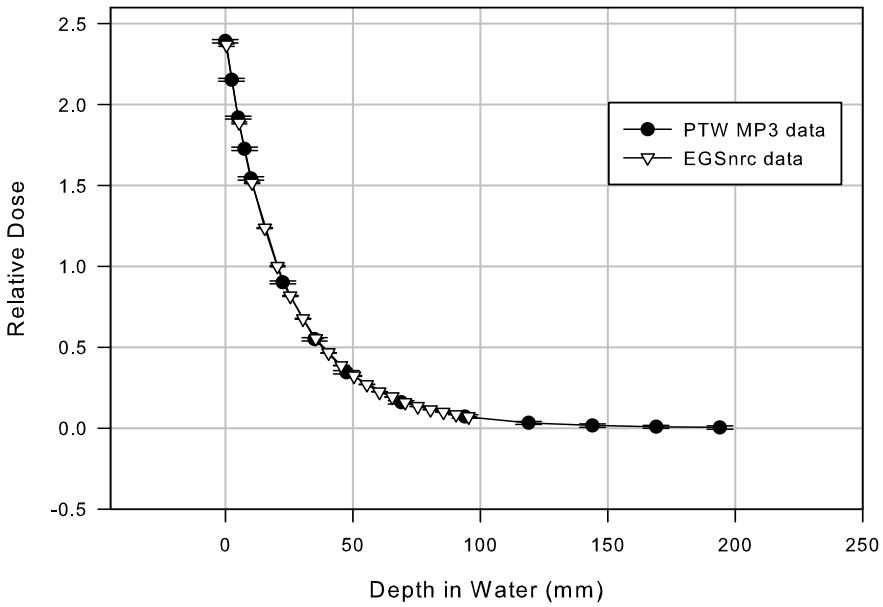

Figure 6.7: Depth dose curves for EGSnrc Monte Carlo simulation and PTW MP3 water phantom measurement of a Pantak Therapax SXT 150 unit 80kV photon beam with 1cm diameter circular applicator attached.

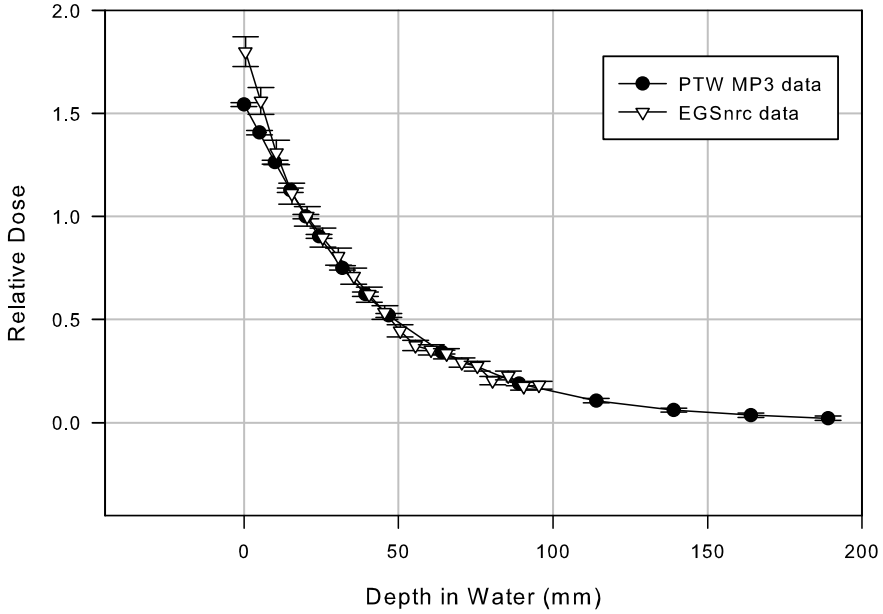

Figure 6.8: Depth dose curves for EGSnrc Monte Carlo simulation and PTW MP3 water phantom measurement of a Pantak Therapax SXT 150 unit 100kV photon beam with 5cm diameter circular applicator attached.

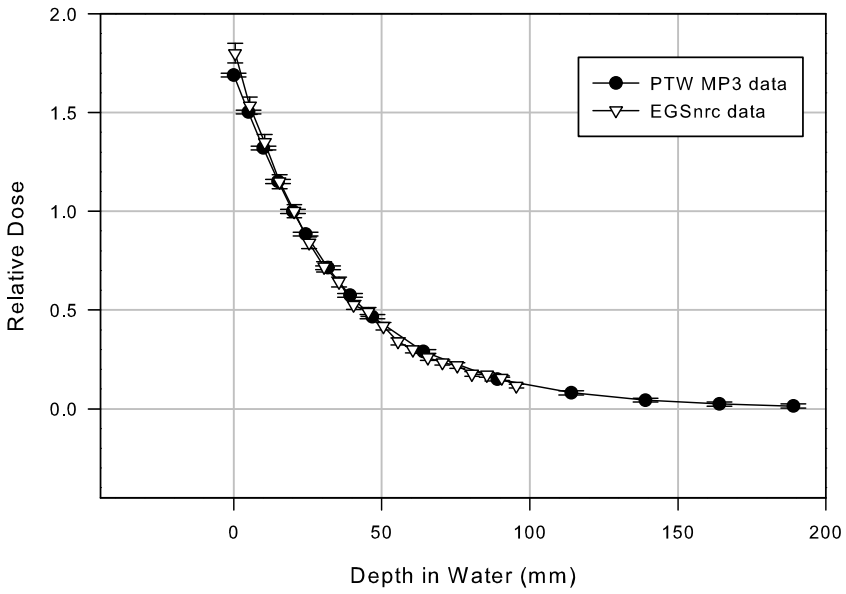

Figure 6.9: Depth dose curves for EGSnrc Monte Carlo simulation and PTW MP3 water phantom measurement of a Pantak Therapax SXT 150 unit 100kV photon beam with 3cm diameter circular applicator attached.

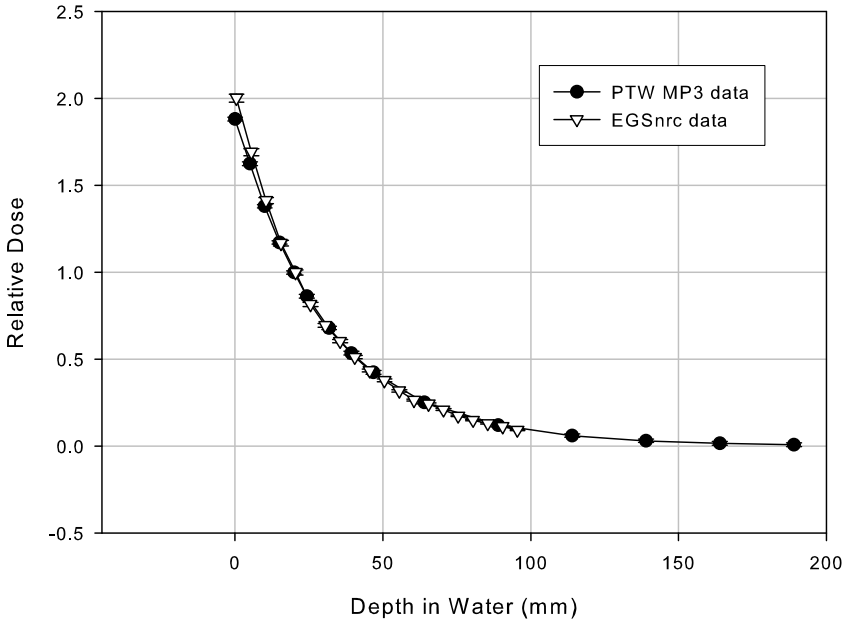

Figure 6.10: Depth dose curves for EGSnrc Monte Carlo simulation and PTW MP3 water phantom measurement of a Pantak Therapax SXT 150 unit 100kV photon beam with 1cm diameter circular applicator attached.

The 80kV and 100kV depth dose curves show excellent agreement at depth with all different diameter applicators except for near the surface. The larger the applicator diameter the larger the discrepancy near the water surface leading to a difference of the order of 20% in the final millimeter of water for the 5cm diameter applicator. However, if these near surface measurements are considered to be in a high gradient region the ±2mm stipulation of Björk *et al.* is easily satisfied. This difference is in part attributable to experimental difficulties in measuring shallow depth dose deposition. The effective measurement point of the PTW pinpoint chamber type 31015 is along the central axis of the chamber for superficial x-rays [27], but as the chamber breaches the surface near the origin of the coordinate system the graphite exterior of the pinpoint chamber will displace the equivalent volume of air and hence present a relatively greater amount of attenuation at these near surface points and consequently give an apparent decrease in relative dose. The PTW pinpoint chamber type 31015 was considered the most appropriate chamber given the small chamber size, hence less perturbation of the radiation field on breaching the surface. Plane parallel type chambers were considered inferior due to the meniscus formed on the entrance face of the chamber as it breaches the surface, hence elevating any surface dose discrepancy further.

Profiles

The following graphs show the profile curves associated with EGSnrc Monte Carlo simulation and PTW MP3 water phantom measurements for 80kV and 100kV photon beams from the Pantak Therapax SXT 150 unit for 5cm, 3cm and 1cm diameter applicator cones. The Monte Carlo simulations were taken from a water phantom constructed from 2mm voxels with a stand off material of air between the surface of the phantom and the phase space file source. The water phantom measurements and simulations were performed at depths of 2cm and 5cm. All scans and simulations are normalised to unity along the central axis at 2cm depth.

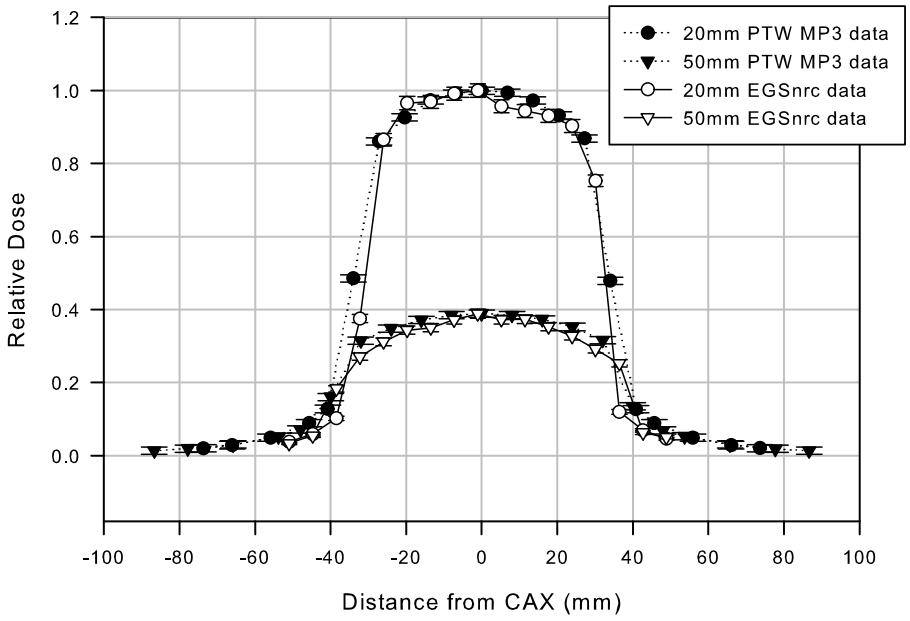

Figure 6.11: Profile curves for EGSnrc Monte Carlo simulation and PTW MP3 water phantom measurement of a Pantak Therapax SXT 150 unit 80kV photon beam with 5cm diameter circular applicator attached.

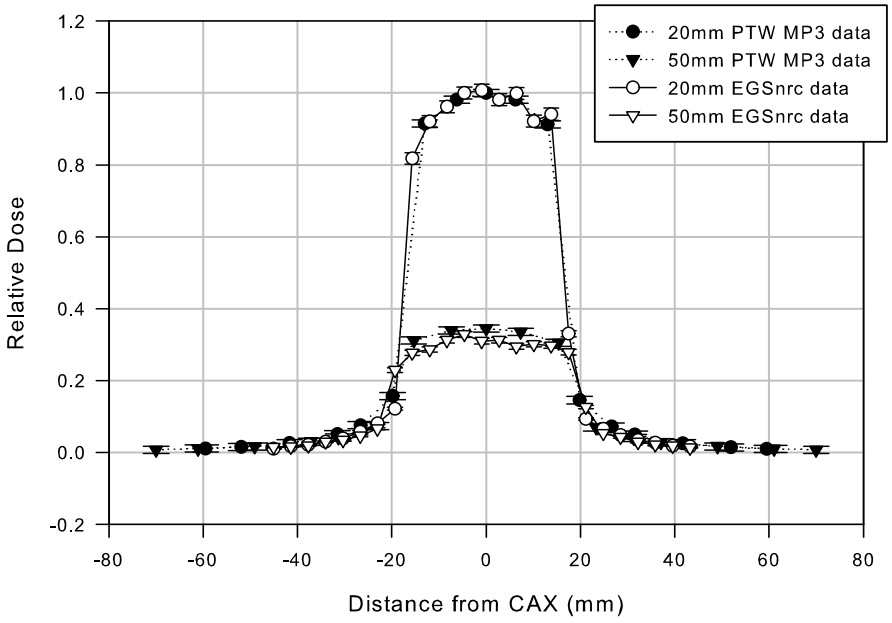

Figure 6.12: Profile curves for EGSnrc Monte Carlo simulation and PTW MP3 water phantom measurement of a Pantak Therapax SXT 150 unit 80kV photon beam with 3cm diameter circular applicator attached.

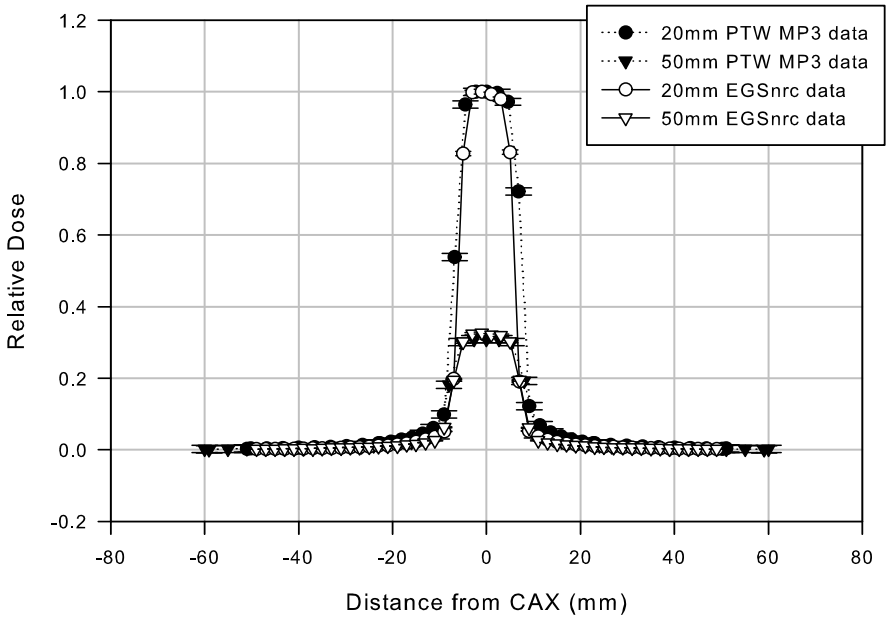

Figure 6.13: Profile curves for EGSnrc Monte Carlo simulation and PTW MP3 water phantom measurement of a Pantak Therapax SXT 150 unit 80kV photon beam with 1cm diameter circular applicator attached.

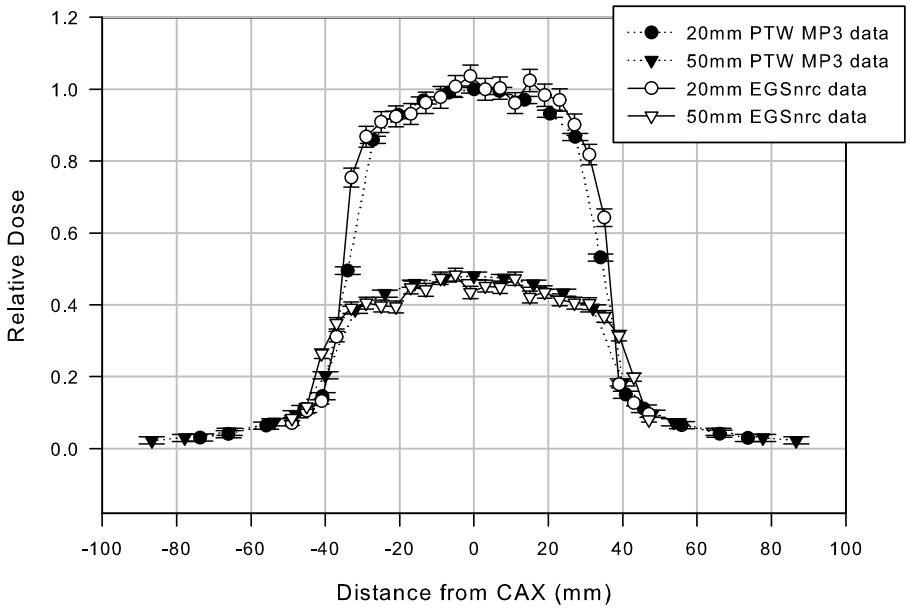

Figure 6.14: Profile curves for EGSnrc Monte Carlo simulation and PTW MP3 water phantom measurement of a Pantak Therapax SXT 150 unit 100kV photon beam with 5cm diameter circular applicator attached.

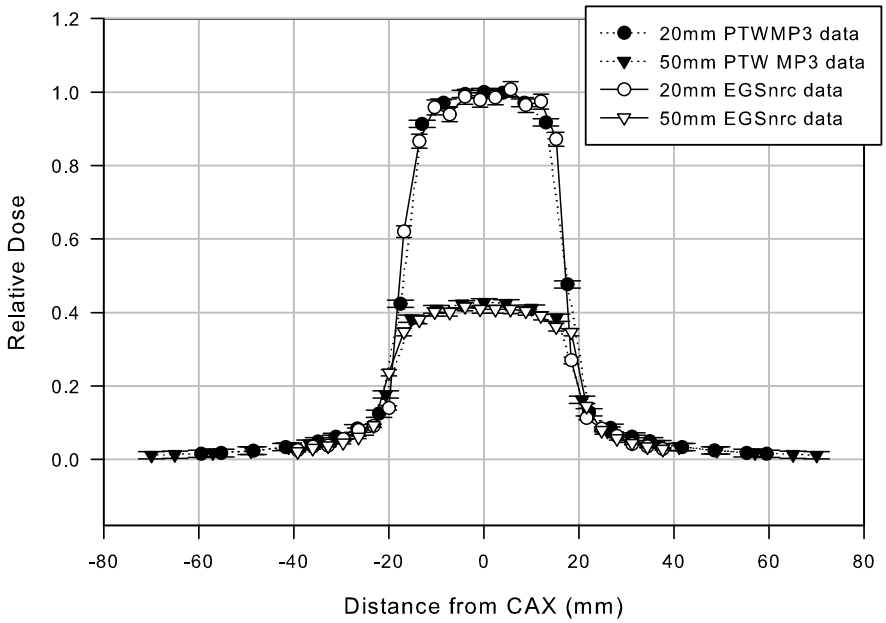

Figure 6.15: Profile curves for EGSnrc Monte Carlo simulation and PTW MP3 water phantom measurement of a Pantak Therapax SXT 150 unit 100kV photon beam with 3cm diameter circular applicator attached.

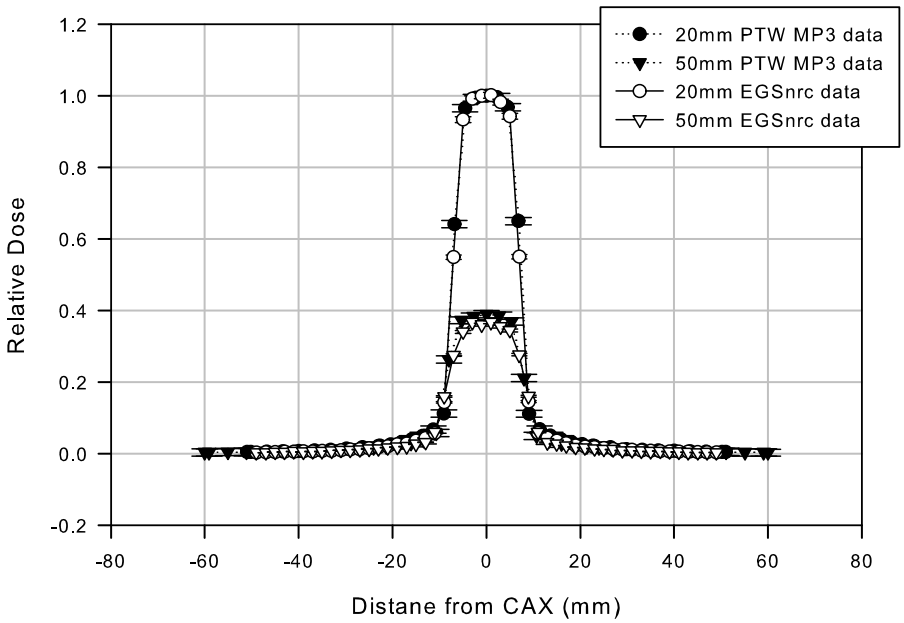

Figure 6.16: Profile curves for EGSnrc Monte Carlo simulation and PTW MP3 water phantom measurement of a Pantak Therapax SXT 150 unit 100kV photon beam with 1cm diameter circular applicator attached.

In each of the energies the 5cm diameter applicator demonstrates a larger degree of

divergence between the EGSnrc simulation and PTW MP3 water phantom data in the penumbral regions. Otherwise the fit between the two sets of data is excellent. The 5cm diameter applicator penumbral differences being in the high dose gradient region satisfy the Björk *et al.* stipulation of ±2mm except when the distance from the central axis is past the 50% mark of the profile. In this region the simulation statistics become poor with errors of up to 10% being evident. Longer simulation times could alleviate this but any improvement in simulation statistics is likely due to the multiple use of particles in the phase space file thus artificially producing smaller errors.

Isodose Curves

The following graphs show the isodose curves associated with EGSnrc Monte Carlo simulation (solid line in the graphs) and PTW MP3 water phantom measurements (dashed line in the graphs) for 80kV and 100kV photon beams from the Pantak Therapax SXT 150 unit for 5cm, 3cm and 1cm diameter applicator cones. The Monte Carlo simulations were taken from a water phantom constructed from 2mm voxels with a stand off material of air between the surface of the phantom and the phase space file source. All scans and simulations are normalised to unity along the central axis at 2cm depth.

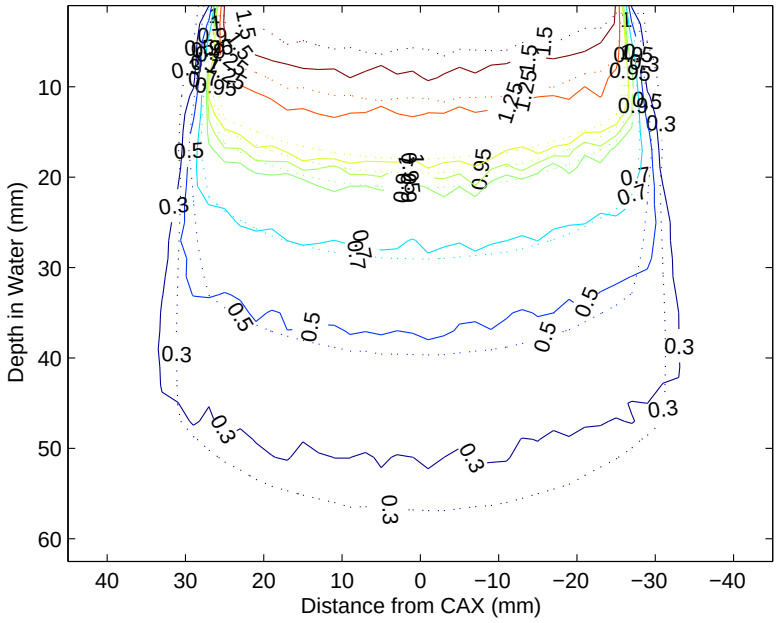

Figure 6.17: Isodose curves for EGSnrc Monte Carlo simulation (solid line) and PTW MP3 water phantom measurement (dashed line) of a Pantak Therapax SXT 150 unit 80kV photon beam with 5cm diameter circular applicator attached.

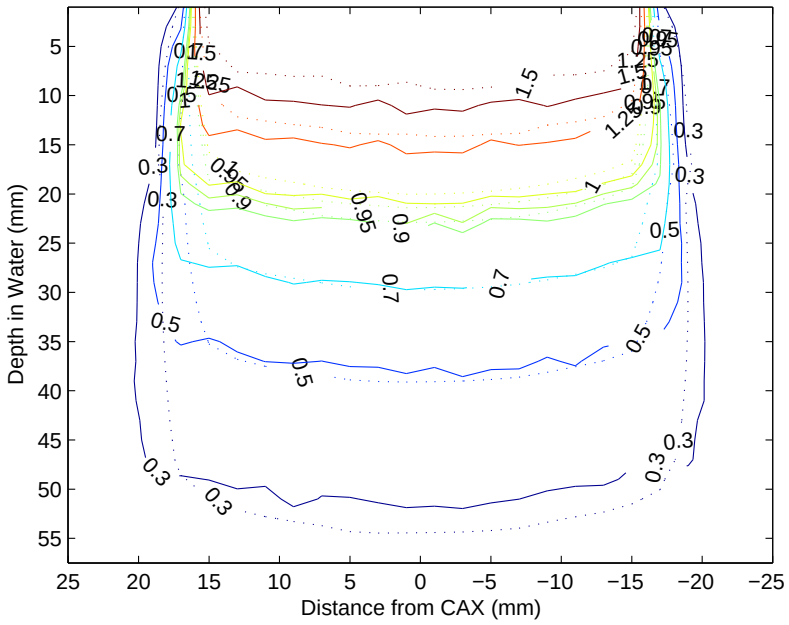

Figure 6.18: Isodose curves for EGSnrc Monte Carlo simulation (solid line) and PTW MP3 water phantom measurement (dashed line) of a Pantak Therapax SXT 150 unit 80kV photon beam with 3cm diameter circular applicator attached.

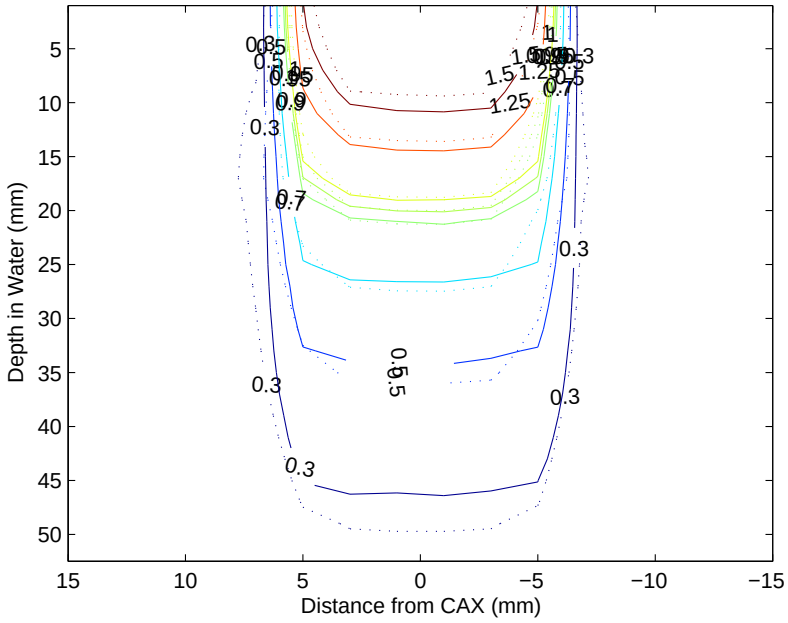

Figure 6.19: Isodose curves for EGSnrc Monte Carlo simulation (solid line) and PTW MP3 water phantom measurement (dashed line) of a Pantak Therapax SXT 150 unit 80kV photon beam with 1cm diameter circular applicator attached.

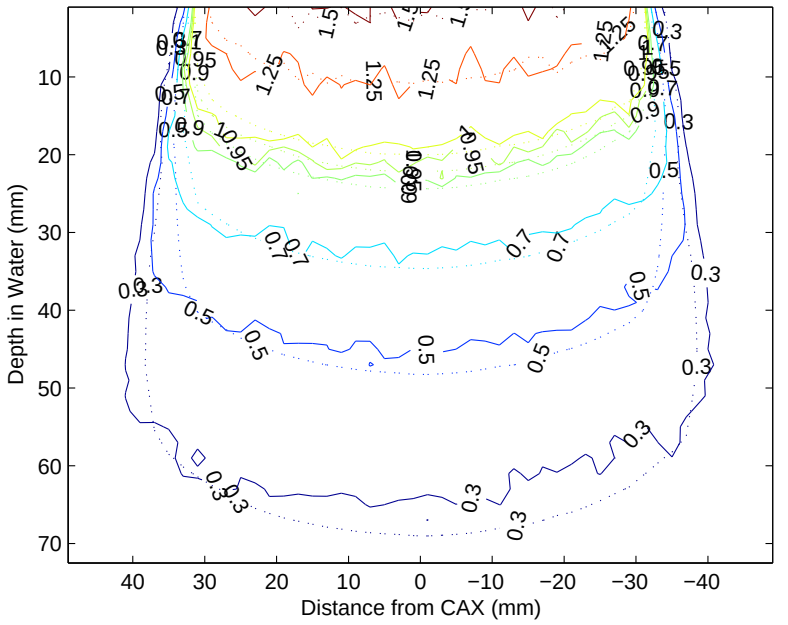

Figure 6.20: Isodose curves for EGSnrc Monte Carlo simulation (solid line) and PTW MP3 water phantom measurement (dashed line) of a Pantak Therapax SXT 150 unit 100kV photon beam with 5cm diameter circular applicator attached.

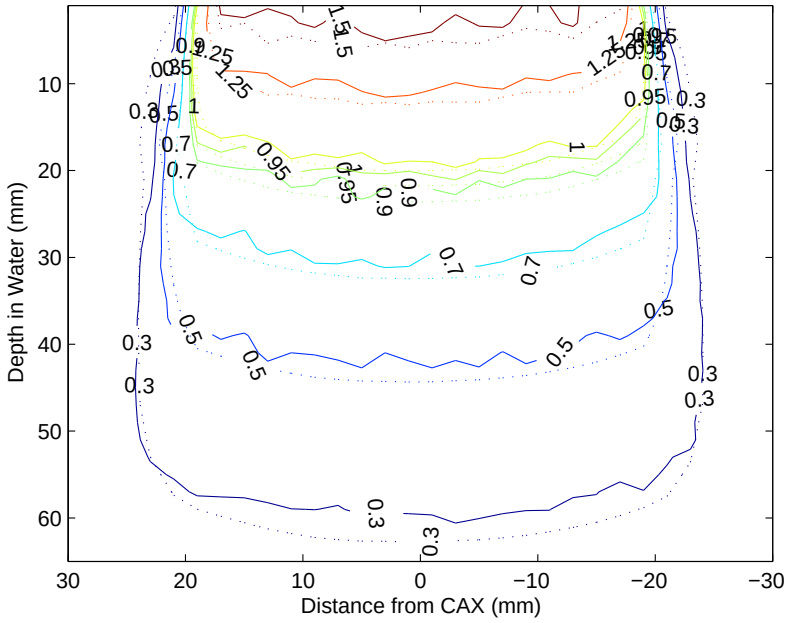

Figure 6.21: Isodose curves for EGSnrc Monte Carlo simulation (solid line) and PTW MP3 water phantom measurement (dashed line) of a Pantak Therapax SXT 150 unit 100kV photon beam with 3cm diameter circular applicator attached.

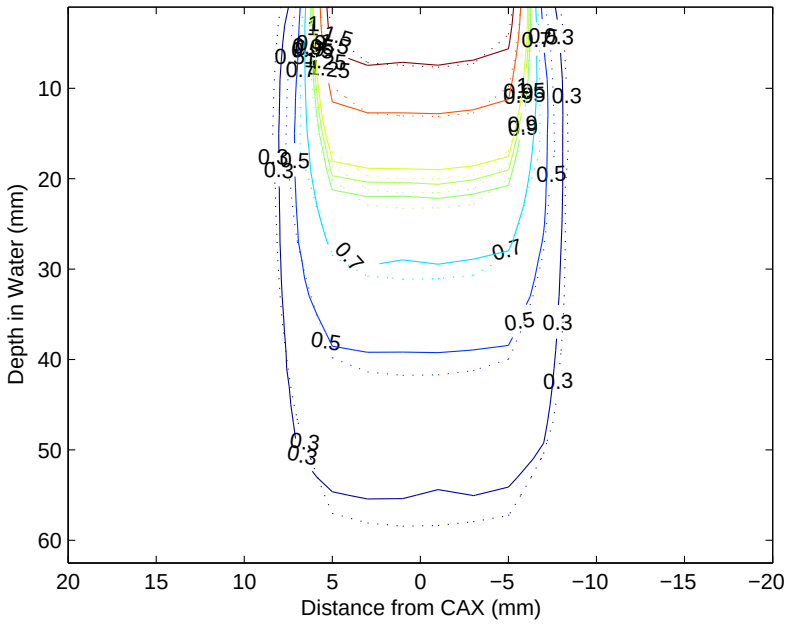

Figure 6.22: Isodose curves for EGSnrc Monte Carlo simulation (solid line) and PTW MP3 water phantom measurement (dashed line) of a Pantak Therapax SXT 150 unit 100kV photon beam with 1cm diameter circular applicator attached.

The matching of the isodose curves is poor in peripheral areas and at times lies outside of the Björk *et al.* stipulation of ±2mm. However, this is due to the means of reconstructing the curves from the limited PTW MP3 water phantom data set. The PTW MP3 water phantom isodose curves were linearly interpolated by considering the percentage depth dose curve as the "spine" of a three dimensional isodose map and overlying "ribs" of suitably normalised profile curves at depth. The isodose map was also constrained at the surface to match the field size of the applicator. Coupled with the inherent empirical difficulty of determining surface dose this can account for the mismatch of the isodose curves in the peripheral areas. Even though there are inherent difficulties in deriving measured isodose plots the comparison is still desirable to see the global nature of the measured and simulated isodose curves are broadly similar.

6.3 MeV Electron Accelerator

The simulation of medical electron accelerators is covered extensively in the literature (see for example [28]). The high degree to which Monte Carlo simulations represent actual dose distributions has contributed to the release of an algorithm by Varian Medical Systems that makes extensive use of Monte Carlo methods [29]. Varian Medical System's electron Monte Carlo algorithm, called eMC, is ostensibly a pared down Monte Carlo simulation that utilises the macro Monte Carlo method of Neuenschwander *et al.*[30] and the initial phase space model of Janssen *et al.*[31]. Varian Medical Systems is not alone in this respect with Cygler *et al.* reporting upon the implementation of Nucletron's Theraplan Plus™ Monte Carlo based treatment planning system for electrons beams utilising Iwan Kawrakow's VMC++ algorithm [32].

Despite the commercial embracement of Monte Carlo methods for electron beam treatment planning algorithms there still exist problems inherent in the treatment planning process. Such problems are exclusively due to the inability of the clinical end user to completely specify the parameters of the electron beams exiting the linear accelerator. An example of this can be seen in Huang *et al.* where the problem of large electron fields is discussed [33]. However, this cannot be seen as a failure of the Monte Carlo method but more due to the radiotherapy community becoming aware of the power and versatility of the Monte Carlo method for electron treatment planning and applying it to poorly parameterised beams.

The Monte Carlo method also highlights the structure that one can determine from the analysis of all aspects of a electron accelerator. This can especially be seen when analysing the spectral properties of a MeV electron beam. Khan [**?**] gives a smooth energy spectrum whereas using the BEAM data processing tool, BEAMDP, one can determine the spectral content of a nominal 6 MeV electron beam for all particles as in figure 6.23. Clearly, the most striking feature of this spectrum is the high energy double peak. This does not in any way affect the dosimetric properties of the beam with subsequent percent depth doses and profiles demonstrating an excellent agreement with experimental data. This double peak is in fact due to some of the peripheral electrons in the initial electron beam that exits the primary collimator not passing through significant amounts of material in the scattering foil high up in the electron accelerator head. A similar study from the National Research Council of Canada [34] also details how such structure in spectra can arise from scattering consideration of component modules further downstream in the electron accelerator head.

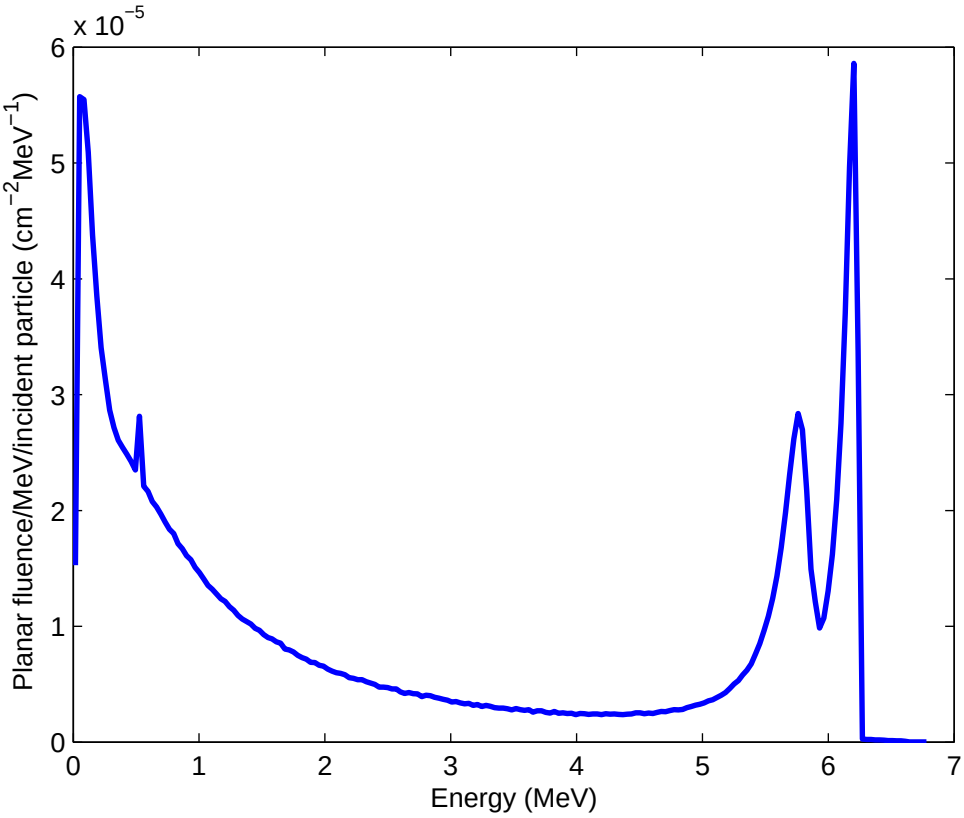

Figure 6.23: BEAMDP derived energy spectrum for all particles from a 6.7 MeV initial electron beam energy incident upon a Varian Clinac® 2100C geometry

Varian Clinac® 2100C Geometry

In order to obtain geometry information for the Varian Clinac® 2100C it was necessary to sign a non-disclosure agreement with Varian Medical Systems. Once the agreement was signed a confidential information package was released. Clearly it is necessary for Varian Medical Systems to protect the proprietary geometry associated with their machines but due to the large number of requests from graduate students and researchers who require information about the clinical machines for Monte Carlo modelling they kindly released geometry details, FAQ sheet and contact details to those researchers willing to sign the non-disclosure agreement. The following 6 MeV simulation makes extensive use of the geometry data released by Varian Medical Systems and in accordance with the non-disclosure agreement none of the BEAMnrc parameters used in the modelling shall be given here. Varian Medical Systems does however mention that if collaboration is sought with other colleagues who have signed the non-disclosure agreement they should contact Varian Product Marketing.

6.3.1 6 MeV Simulation and Measurement

The approximation used in the current thesis in modelling the Clinac® 2100C electron beam was to assume a monoenergetic pencil electron beam exits from the bending magnet system. The shape of the electron beam was taken to be circular in cross section with

a narrow diameter of 1 mm. This was chosen as an initial assumption and used to compare against the PTW MP3 water phantom data. No significant deviation from the experimentally determined dose distributions was observed; so apart from the previously mentioned structure in the beam spectrum the assumption was not changed. The energy settled on after a number of iterations for the monoenergetic electron beam was 6.7MeV. This correlates well with values used by colleagues undertaking Varian Clinac® 2100C simulations in other radiotherapy centres in New Zealand[35].

The PTW plane parallel Roos chamber was used in the PTW MP3 water phantom for determining all percent depth dose and profile measurements. A PTW Semiflex ionisation chamber type 31010 was used as a reference in the electron field for these measurements. Careful consideration was given to scanning directions, speeds and steps in the water phantom, especially those near the water surface, so as to disturb the water surface as little as possible during the scans.

Initially 6 MeV and 9 MeV electron beams were going to be considered. However, after extensive discussions with radiation oncologist Dr. David Hamilton it was decided that the only clinically relevant beam that we need consider for the sites we had planned for Monte Carlo simulation was 6 MeV. Additionally the 6×6 electron applicator was the only applicator relevant for the field sizes for the planned simulations. Simulated and measured beams were taken for both electron applicator sizes of 6×6 and 10×10 as this gave a more robust data set with which to draw comparisons with and hence determine if the simulation was a faithful representation of the clinical electron beam.

All simulations and measurements were carried out at 100 cm SSD. Any comparison between Monte Carlo simulation and water tank measurement that agrees within the ±2% or ±2mm stipulation of Björk *et al.*[17] shall be considered a reasonable fit.

Depth Dose Curves

The following graphs show the depth dose curves associated with EGSnrc Monte Carlo simulation and PTW MP3 water phantom measurements for for 6×6 and 10×10 field size electron beams from the Clinac® 2100C. The Monte Carlo simulations were taken from a water phantom constructed from 2mm voxels with air between the surface of the phantom and the phase space file source. The PTW MP3 water phantom measurements were performed bottom up so as to minimise any artifacts from near surface measurements. All scans are normalised to unity at a depth specified by the electron beam d_{max}.

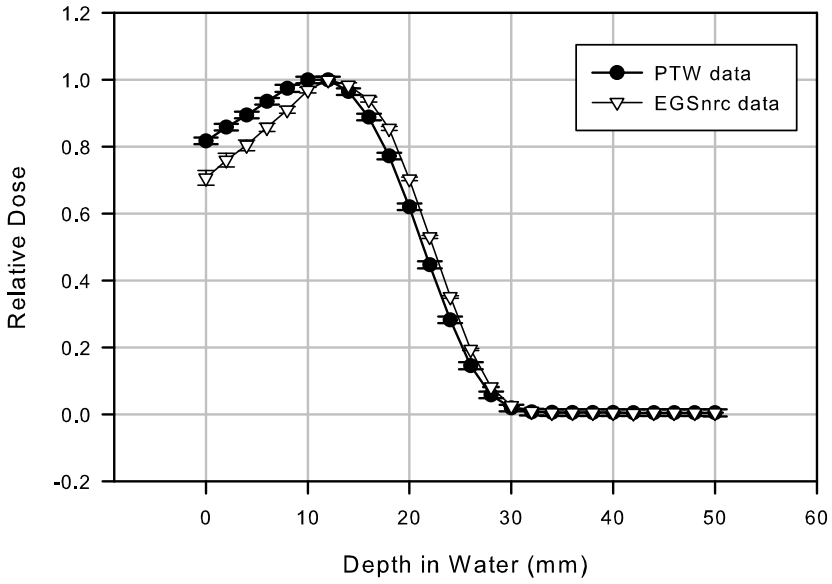

Figure 6.24: Depth dose curves for EGSnrc Monte Carlo simulation and PTW MP3 water phantom measurement of a Varian Clinac® 2100C 6 MeV electron beam with 6 cm × 6 cm electron applicator attached.

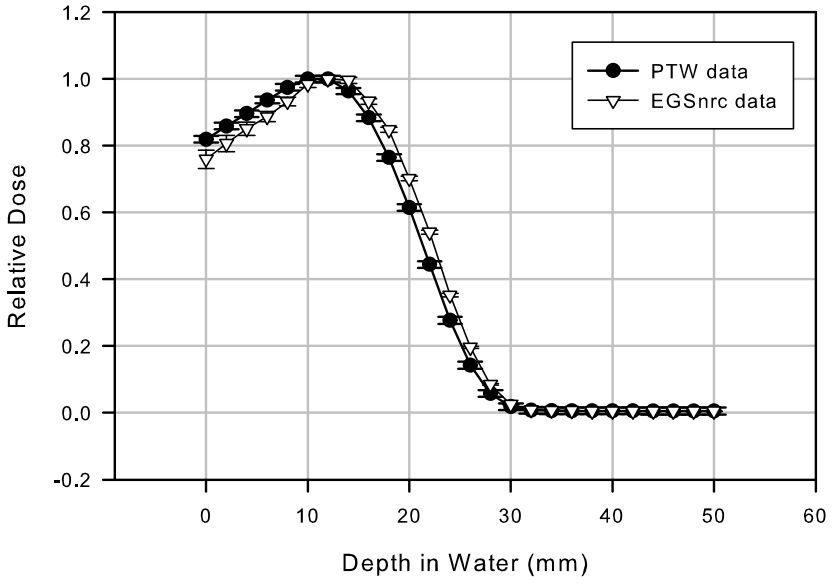

Figure 6.25: Depth dose curves for EGSnrc Monte Carlo simulation and PTW MP3 water phantom measurement of a Varian Clinac® 2100C 6 MeV electron beam with 10 cm × 10 cm electron applicator attached.

The beams match well past d_{max} easily satisfying the Björk *et al.* stipulation of ±2mm. However, the near surface dosimetry for the smaller field size (6 cm × 6 cm electron applicator) shows a marked deviation in the final 8 mm of the depth dose curve. The surface dosimetry with a plane parallel chamber is very problematic due to the formation of a meniscus of water on the top of the chamber as it advances towards the water surface and especially due to the fact that the effective point of measurement is directly behind the front face of the window at an equivalent water depth of 1 mm. These factors combined can lead to the poor match observed in the 6 cm × 6 cm electron applicator graph.

Profiles

The following graphs show the profile curves associated with EGSnrc Monte Carlo simulation and PTW MP3 water phantom measurements for 6 MeV beam from the Varian Clinac® 2100C for 6×6 and 10×10 field size electron beams. The Monte Carlo simulations were taken from a water phantom constructed from 2mm voxels with air between the surface of the phantom and the phase space file source. The water phantom measurements and simulations were performed at the surface and at depths of 0.5cm, 1cm and 3cm. All scans and simulations are normalised to unity along the central axis at d_{max}.

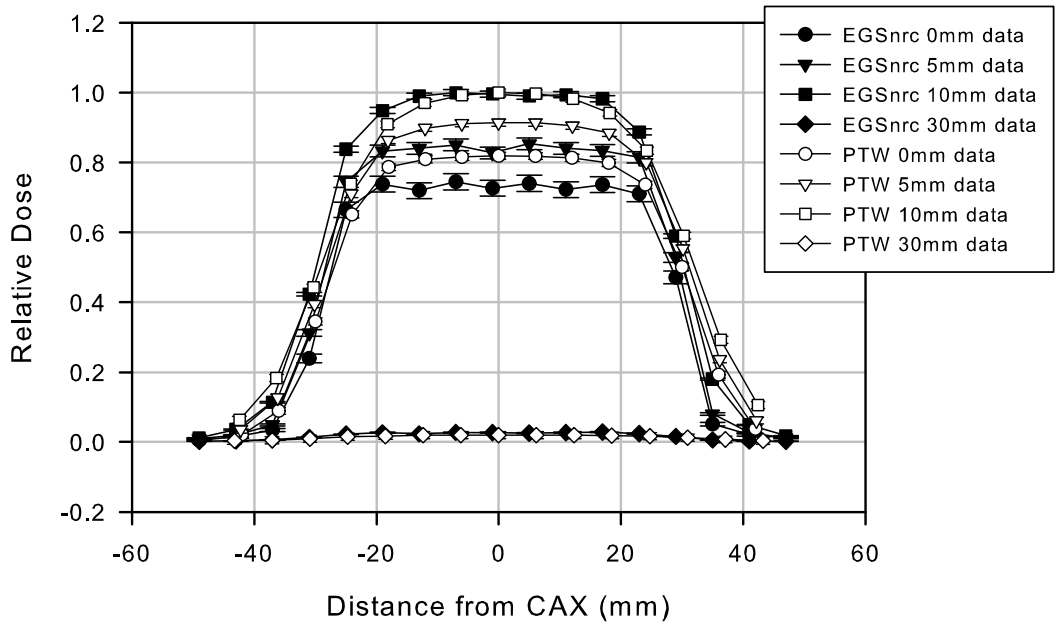

Figure 6.26: Profile curves for EGSnrc Monte Carlo simulation and PTW MP3 water phantom measurement of a Varian Clinac® 2100C 6 MeV electron beam with 6 cm × 6 cm electron applicator attached.

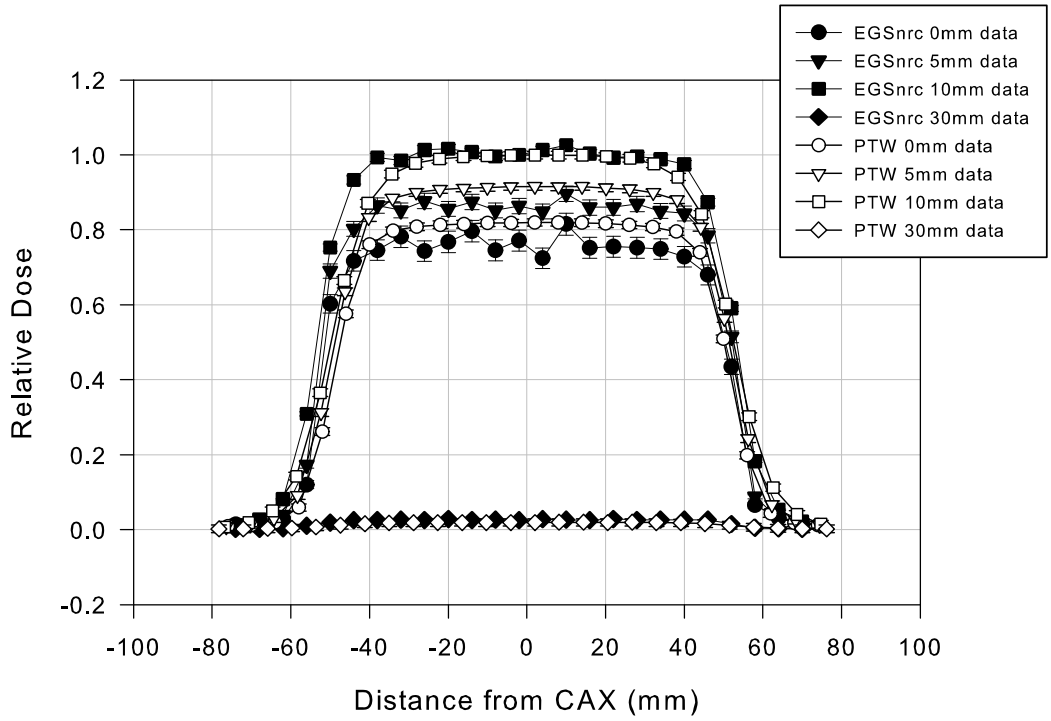

Figure 6.27: Profile curves for EGSnrc Monte Carlo simulation and PTW MP3 water phantom measurement of a Varian Clinac® 2100C 6 MeV electron beam with 10 cm × 10 cm electron applicator attached.

The poor match between the surface and 0.5 cm curves is evident in these profiles as they were evident in the depth dose profiles. However, the structure that the profiles highlights is the convergence between the simulation versus the measured values in the penumbral regions. The curves within the penumbral regions meet the Björk *et al.* stipulation of ±2mm. Any difference between the simulated and measured values can be attributed to the finite size of the PTW Roos chamber air cavity. The relatively large air cavity with respect to the small 2 mm voxel EGSnrc simulation volume tends to blur the edges of sharp dose gradients and hence we see a marked difference near the bottom of the profiles near the ±40 mm and ±60 mm mark in the 6×6 and 10×10 cases respectively.

Also of note is the jagged nature of the surface EGSnrc simulation profile, this is due to poor signal to noise ratio at the surface. It is possible to run the simulation for longer to remove this but the number of particles in the phase space file would not be sufficient to guarantee reliable statistics associated with the simulation. Of course this could be solved by running the initial phase space generating simulation for many more histories but this would be infeasible on the available computer resources dedicated to this project.

Isodose Curves

The following graphs show the isodose curves associated with EGSnrc Monte Carlo simulation (solid line in the graphs) and PTW MP3 water phantom measurements (dashed line in the graphs) for 6 MeV beam from the Varian Clinac® 2100C for 6×6 and 10×10 field size electron beams. The Monte Carlo simulations were taken from a water phantom constructed from 2 mm voxels with air between the surface of the phantom and the phase

space file source. All scans and simulations are normalised to unity along the central axis at d_{max}.

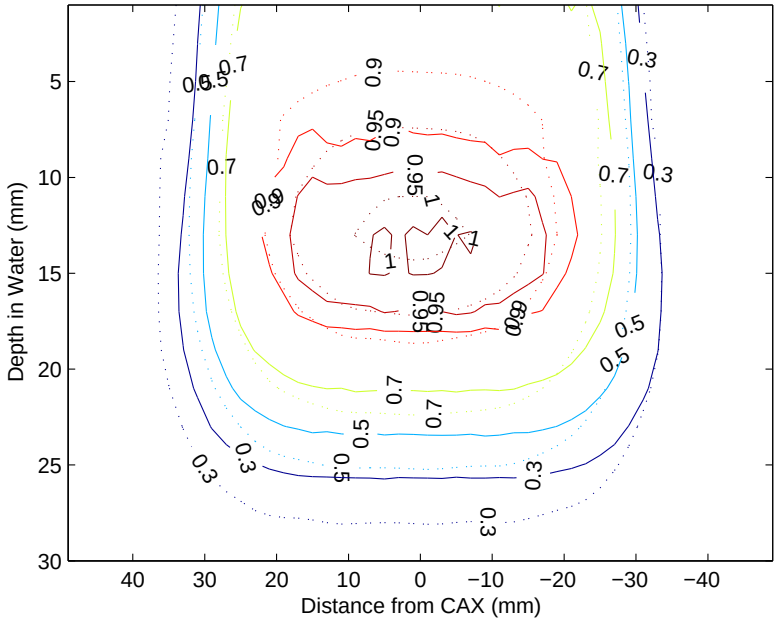

Figure 6.28: Isodose curves for EGSnrc Monte Carlo simulation (solid line) and PTW MP3 water phantom measurement (dashed line) of a Varian Clinac® 2100C 6 MeV electron beam with 6 cm × 6 cm electron applicator attached.

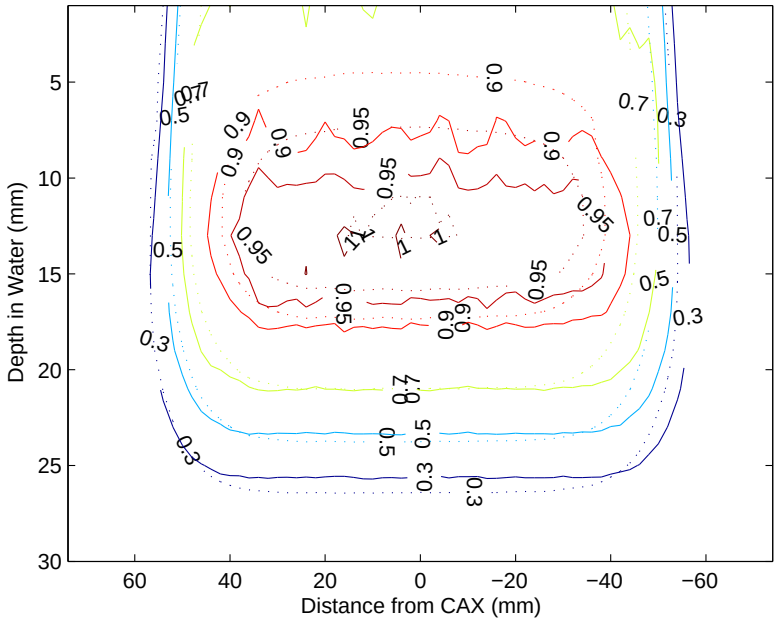

Figure 6.29: Isodose curves for EGSnrc Monte Carlo simulation (solid line) and PTW MP3 water phantom measurement (dashed line) of a Varian Clinac® 2100C 6 MeV electron beam with 10 cm × 10 cm electron applicator attached.

As with the superficial case the isodose reconstructions of the PTW MP3 water phantom data are prone to interpolation errors. The matching of the isodose curves is poor in some peripheral areas and at times lies outside of the Björk *et al.* stipulation of ±2mm. Additionally the mismatch in the isodose curves near the surface is evident in the centre of the beam. However, the inherent empirical difficulty of determining surface dose and penumbral structure can account for some of the mismatch of the isodose curves in these areas. Ultimately the focus of this thesis is not generating a perfect match to the electron beams exiting from the Wellington Blood and Cancer Centre Varian Clinac® 2100Cs, studies showing excellent matches have been reported in the literature for many years (see for example [34]). The focus is upon the comparison between kV photons and MeV electrons in the head and neck region for the irradiation of superficial lesions and all that is required for this to still be a valid study are realistic therapy type beams which this chapter has demonstrated have been simulated.

Chapter 7

Dose Distributions in Complex Geometries

Given that Monte Carlo methods for determining the transport of photons and electrons through matter have been examined in chapter 4 and that the physics of dose deposition has been established for the Monte Carlo method in chapter 5 it is now possible to apply the method to some physical problem. As the determination of the parameters of the photon and electron beams was discussed in chapter 6 we are now in a position to apply the derived phase space files for specific treatment fields. The problem in this thesis is determining the pattern of the dose distribution in phantoms representative of patients with electron and photon beams applied representative of the therapeutic beams employed in a particular treatment. The treatment planning process is detailed in table 7.1, this is a generic process list and dose not apply completely to superficial photon and some electron treatments. It can be clearly seen that the Monte Carlo method can be used quite successfully in such a process provided that once the initial geometric data is extracted the process is followed closely.

The phantoms generated in the current thesis shall be the initial point of discussion in this chapter. In order to create a relevant simulation the issue of the construction and editing of phantoms is pivotal. The reason behind the current investigation was that the pattern of dose distributions in head and neck treatments with additional high atomic number shielding materials was not adequately modelled using current treatment planning system algorithms. This inadequacy is generated by rapidly sloping surfaces, different density interfaces and radiosensitive structures near the surface in the area of treatment. Hence the term "complex geometries" is used in the current context to encapsulate these idiosyncracies of the considered phantoms.

The chapter will then discuss Monte Carlo determined dose distributions and provide an analysis and comparison of the plans generated. The intention is to provide accurate and useful information in the evaluation of a treatment plan to optimise the outcome of radiotherapy for patients.

7.1 Geometries

Amongst the Monte Carlo simulation impediments to the study of radiotherapy outcomes for radiation treatments is the enormous complexity of the phantoms needed for the transport problem to be posed. The file format that describes voxel numbers, boundaries, densities and material types for EGSnrc simulations is the `egsphant` format. These are ASCII files generated for EGSnrc simulations by the user either by hand or by a BEAM application called `ctcreate`. Software tools for manipulating geometries are well advanced for modern treatment planning systems, however, for the typical Monte Carlo system of codes distributed freely over the internet for research purposes such software tools are non-existent. Therefore, a large component of time is required to configure the large

1. Patient Positioning and Immobilisation
• Establish patient reference marks/patient coordinate system
2. Image Acquisition and Input
• Acquire and input CT, MR and other imaging information into the planning system
3. Anatomy Definition
• Define and display contours and surfaces for normal and critical structures
• Geometrically register all input data including registration with initial simulation contours, films patient positions, etc.
• Define target contours, generate 3-D target surface using surface expansion, import target information from multiple imaging modalities
• Generate electron density representation from CT or from assigned bulk density information
4. Beam/Source Technique
• Determine beam or source arrangements
• Generate beam's eye view displays
• Design field shape (blocks, MLC)
• Determine beam modifiers (compensators, wedges)
• Determine beam or source weighting
5. Dose Calculation
• Select dose calculation algorithm and methodology, calculation grid and window, etc.
• Perform dose calculations
• Set relative and absolute dose normalisations
• Input the dose prescription
6. Plan Evaluation
• Generate 2-D and 3-D dose displays
• Perform visual comparisons
• Use DVH analysis
• Calculate the NTCP/TCP values and analyse
• Use automated optimisation tools
7. Plan Implementation
• Align (register) the real patient with the plan (often performed at a plan verification simulation)
• Calculate the monitor units or implant duration
• Generate hardcopy output
• Transfer plan into record and verify system
• Transfer plan to treatment machine
8. Plan Review
• Perform overall review of all aspects of plan before implemenation

Table 7.1: The clinical treatment planning process (Reproduced from [36])

ASCII files comprising all of the geometry information. The means of generating and editing the `egsphant` files shall be discussed in the current section after some preliminary comments concerning the selection of the phantom, artifacts, CT number to density and

voxel considerations.

A decision regarding whether to use a RANDO® phantom as opposed to an anonymised CT image series of an actual patient was required before any investigation could begin[1]. The anonymised CT image series was decided upon after comparison of the images from both. The RANDO® phantom, though completely anonymous, did not display the true extent of complexity in terms of different density interfaces and air gaps that the anonymised CT image series did. The anonymised CT image series that was taken for the present thesis was decided upon because initial matching of the Monte Carlo method to the Varian Eclipse treatment planning system was conducted for a previously planned large regular electron field on the cheek of the patient in question.

Partial voluming artifacts at the surface of the phantom are particularly troublesome in a Monte Carlo simulation. This is not seen in a commercial treatment planning system as the body contour is defined and all voxels external to this contour have dose zeroed in them. A similar process is followed in a Monte Carlo simulation under EGSnrc; however, the voxels with a density close to air have the dose zeroed in them. This does not account for the voxels close to the phantom contour that are prone to partial voluming increasing their intrinsic density, hence yielding a significant distortion to the dosimetry near the surface.

The CT number to either physical or relative electron density relationship must be established for correct dosimetric calculations to performed in any Monte Carlo simulation. This was accomplished by using the Radiology Department of Wellington Hospital Picker PQ5000 CT that has a CT calibration curve applied to it from comparison to a Gammex Electron Density CT Phantom RMI 467. It can therefore be established that the CT numbers that are generated are representative of actual relative electron density. This calibration curve can be transferred to the `egsphant` file.

Voxel size considerations impact upon simulation time significantly. Depending on the calculation volume that is considered the voxel size can create an untenably long simulation hence rendering the Monte Carlo method impractical. However, with a salient choice of calculation volume this becomes irrelevant. Voxel size and the method of analysis is the next consideration. Depending on how the data is to be exported and imported between different software tools dictates the voxel sizes that may be used in a simulation. Ultimately the voxel size is so constrained in the current thesis. This shall be fully developed in section 7.2.1.

7.1.1 `ctcreate`

The EGSnrc system of user codes includes an application for the conversion of a CT image series of DICOM, AAPM, CADPLAN or ADAC Pinnacle file formats into an `egsphant` format phantom file usable by EGSnrc simulation and analysis tools. Typically a subset of the entire data set can be used allowing voxel size and subsequent simulation times to be within reasonable limits. However, given the large amount of data in a typical CT image series this subset can still lead to very large `egsphant` files. Changing the default settings of the `ctcreate` application is necessary to accommodate this large phantom file

[1] A RANDO® phantom is a natural human skeleton cast inside material that is radiologically equivalent to soft tissue. There are lower-density material inserts in the region of the lungs designed to simulate human lungs in a median respiratory state but no differentiating material is located in the head and neck region.

size. The structure of the `egsphant` file includes the number of voxels, voxel boundaries, voxel material and voxel density.

CT calibration curves that align local CT imaging devices with `ctcreate` voxel density output can be applied or a default curve can be applied that yields four standard material types: air, lung, tissue and bone. Either way there is a large degree of flexibility for the user to specify what materials exist in the `egsphant` files as shall be fully developed when discussing the MATLAB® image manipulation undertaken in the current thesis.

A 2.5mm×2.5mm×3mm voxel subset extracted from an anonymised DICOM CT image series was used in the current thesis. Careful alignment of the boundaries of the `egsphant` file was required because the DICOM image values as displayed according to the Varian Eclipse treatment planning system convention do not necessarily align with the native format of the original DICOM file information. As shall be discussed in section 7.2.1 this is entirely due to the choice of software tools to analyse the simulation.

DICOM Images

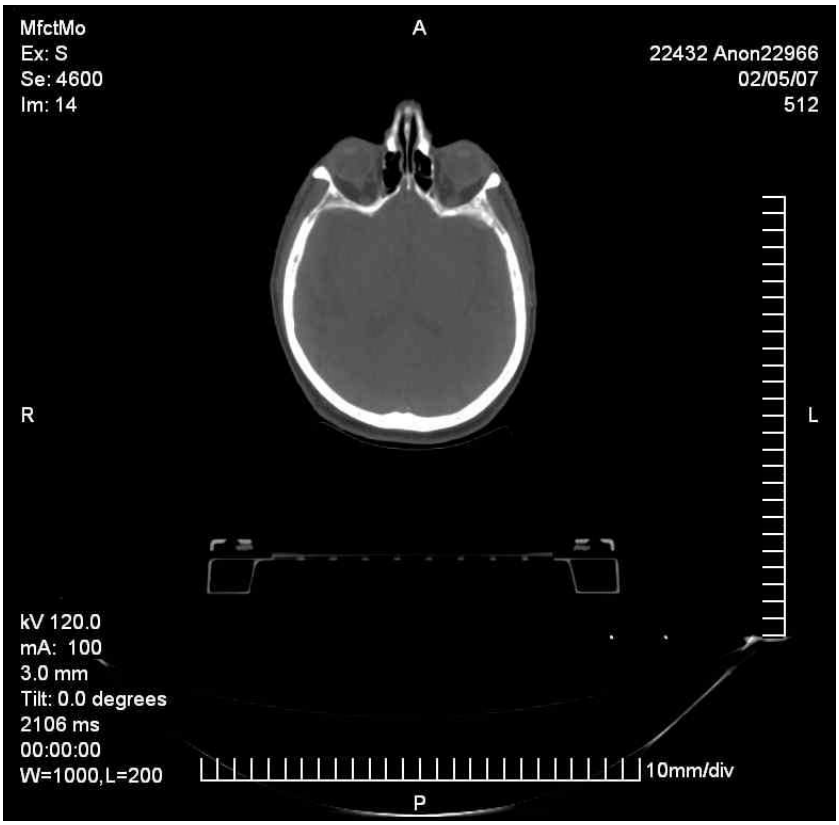

Figure 7.1: An example of an anonymised CT slice from the CT image series used in the current thesis.

The Digital Imaging and Communications in Medicine (DICOM) standard is a widely used and robust standard used for medical imaging devices. In addition to the image information itself a wealth of relevant information is also captured. An example is given in figure 7.1 where energy, mA and slice width information is displayed on the image. This is extremely relevant when matching CT calibration curves and deciding on voxel boundaries. There are a number of tools available for extracting this information, most of

which are available free for research purposes over the internet. The software applications used in the current thesis were AccuLite from Accuimage.com for DICOM viewing and DICOM Shadower for DICOM anonymisation.

MATLAB® image manipulation

The principle limitation of all current medical imaging devices is the inability to accurately capture high density materials alongside low density materials and still maintain good spatial and contrast resolution. Typically the noise in the entire image increases and any structure in close proximity to the high density material is obscured. This in turn leads to poor determination of relative electron density and any dosimetric calculations performed on the basis of the image must be treated with a degree of scepticism.

In conducting Monte Carlo simulations that accurately reflect the true treatment set up it is necessary to edit the `ctcreate` generated phantoms so as to insert the various high density materials that are used to either shield radiosensitive structures or define the field in the irradiation of superficial tumours. The high density materials considered in the current thesis are lead for field shaping and eye shielding and tungsten for eye shielding in the photon and electron cases respectively. In addition to the high density materials additional bolus is typically added to an electron field to shift the d_{max} towards the surface and hence the superficial lesion. These boluses are not routinely placed on the patient during CT imaging, hence this too must be inserted into the `egsphant` files.

The phantom files that are generated by `ctcreate` are ASCII files of 30−50MB size for a typical 60 slice CT study of the head and neck region depending on voxel size. Further reduction in the file size can be achieved by taking subsets of the CT image series; this has been done in the current thesis with an `egsphant` file size of approximately 10MB.

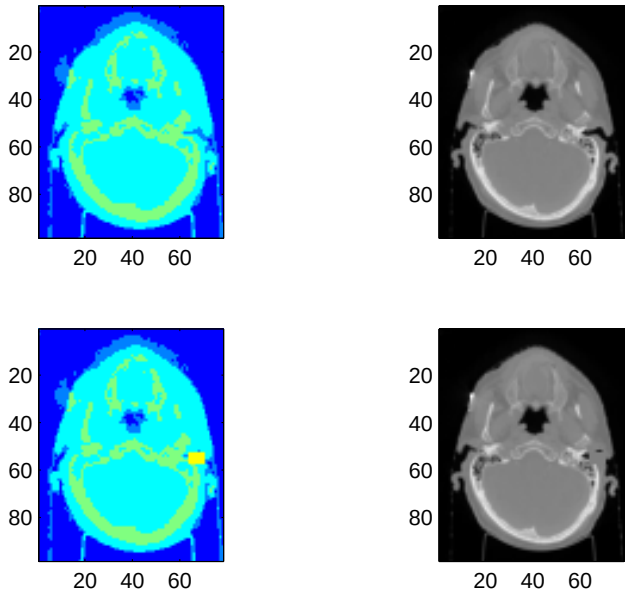

Figure 7.2: An example of an edited slice within an `egsphant` file.

Editing of the `egsphant` files in the current thesis was accomplished by writing a routine in MATLAB® to read in all of the `egsphant` file information and display 2-D planes of the ASCII file and make regions of the 2-D planes accessible for editing (see appendix B for full coding of the routine). Figure 7.2 shows an example of the image prompts used in the routine to guide the user through the editing process. The upper row of images shows a colour coded material matrix visualisation on the left and a grey scale image of the density matrix of the right. After location of the centre of a region of interest nested in the DICOM image native coordinates the user can input any material desired into the material matrix (seen in figure 7.2 as the yellow rectangular area in the left ear canal on the lower left image) with the corresponding density matrix values (lower right image) changed by the user within the same process. The routine works on matrix dimensioned regions of interest so it is possible to generate irregular shaped editing provided that the user carefully tracks the original material and density values that are to remain untouched.

7.2 Dose Distributions

The study of dose distributions for three clinical sites was undertaken for the present investigation. The ear, nose and eye sites were decided upon as the physics of the interactions of the superficial photon beam in comparison to the MeV electron beam for these sites would produce differing dose distributions. The result of this comparison would give radiation oncologists the ability to evaluate plans on more information than currently available. This is relevant clinically as many superficial cancer treatments of the head and neck region can either be irradiated with kV photons or MeV electrons with the former typically been chosen on the experience of radiation oncologists whereas the latter can be modelled and visualised with modern treatment planning systems. However, with the modelling of MeV beams in treatment planning systems the introduction of high atomic number materials invalidates the dose distributions obtained. The only current means of accurately determining dose distributions in these cases is by Monte Carlo methods provided that the phantoms accurately represent the treatment situation as has been established in the previous section.

The physics of the interactions, addressed in chapter 5, shows that the photoelectric effect will dominate for the superficial photon case whereas interactions independent of atomic number will dominate for the MeV electron case. Clearly this will yield different dose distributions with the photons expected to describe a much deeper penetrating dose distribution that will preferentially deposit dose in the bone within the treatment field and the electrons expected to describe a dose distribution confined near the surface but with a larger penumbral region. There is, of course, photon contamination in the MeV electron field but the average energy of this contamination is very low and contributes relatively little the intuitive distribution of dose for an electron field (see figure 6.23 to see the extent of the low energy photon tail of a nominal 6 MeV electron beam from a Varian Clinac® 2100C).

The clinical sites considered in the current thesis are the left ear, left lateral nose and right medial canthus. Each of these sites are good candidates for radiotherapy treatment of basal and squamous cell carcinomas. The sites have convoluted surface geometries, air filled cavities, radiosensitive structures and are in close proximity to bony surfaces which makes them all good candidates for the Monte Carlo method of dose distribution

determination. The PTV associated with each site was drawn on by radiation oncologist Dr. David Hamilton so as to keep the current investigation clinically relevant.

The left ear can be studied with and without bolus in the ear canal. This can provide a means of determining dose to the radiosensitive structures in the inner ear. It is expected that without bolus the photons, either from the superficial unit or the contaminant photons of the electron field, will deposit a larger amount of dose in the inner ear. An impediment to accurately modelling this situation is the partial voluming artifact in CT images for the air filled cavity of the ear canal. It can be readily seen in the `egsphant` file that the ear canal is filled with lung tissue. Given that patient immobilisation is employed in the electron case, but not necessarily the photon case, it is more likely that a representative simulation of this situation would require the editing out of the lung tissue in preference to air. Additionally the actual depth of bolus in the ear canal achievable in the clinical setting was estimated as there are currently no CT images available of patients with bolus inserts in the ear canal.

The left lateral nose presents a similar partial voluming issue concerning the air filled nasal cavity being directly in the beam. In this case given the moist nature of the air circulating in the nasal cavity it has been decided to leave the tissue type and density of the original CT image as interpreted by `ctcreate` intact. The oblique nature of the field needs to be considered especially given the applicator size of both the superficial unit and the Clinac®. It is possible in a Monte Carlo simulation to have a phase space file incident to the isocentre of the treatment overlapping with the patient contour. Physically this is impossible in the clinical setting and careful attention is required to accurately model the treatment set up.

The right medial canthus is the site that provided the original impetus for the current thesis. The eye is routinely shielded in radiation oncology procedures with high density materials due to the radiosensitivity of the lens. A study of the transmission characteristics of lead and tungsten eye shields[37] for superficial photons in the former case and MeV electrons in the latter case highlighted the inadequacy of current models to describe the dose deposition near the eye. There are a number of papers dedicated to the problem of dose determination in the presence of eye shields (see for example [38] [39][40][41]) however these provide only qualitative descriptions. The qualitative descriptions do highlight one of the inadequacies of the Monte Carlo method; the voxel size used in the current thesis masks the presence of a region of slightly elevated dose directly underneath the eye shield [42]. This provides a beneficial reminder to any investigator using Monte Carlo methods that any technique used to calculate dose has intrinsic limitations not always immediately obvious.

7.2.1 DOSXYZnrc

EGSnrc has a user code written that facilitates the simulation of dose deposition in a rectilinear voxel phantom called DOSXYZnrc. For the current investigation it was necessary to change the default settings of DOSXYZnrc to accommodate the large phantom sizes under consideration. The output from a DOSXYZnrc mediated simulation is a `3ddose` file that is formatted to includes the number of voxels in the simulation, voxel boundaries, dose per voxel and uncertainty per voxel. The dose is expressed in absolute terms and requires the user to normalise it to the specific display needs.

The number of simulation histories is an important parameter to consider in any

DOSXYZnrc mediated simulation. Principally, if the number of histories is too low then the uncertainties associated with the doses per voxel become relatively large. Typically the current investigation aims for an uncertainty of $\pm 2\%$ for the dose uncertainty at d_{max}. This can lead to high uncertainties in the penumbral regions and near the surface of the simulation. In such cases where surface and penumbral dosimetry are of importance the number of simulation histories must be increased. There is a drawback to this approach in that the number of particles present in the phase-space file acting as the radiation source in the simulation could be entirely used in the simulation. In such a situation the phase-space particles are used again, thus artificially decreasing the uncertainties associated with dose per voxel. The only means of avoiding this is to generate larger phase-space files.

Once the `3ddose` files are generated the data can be analysed to determine whether the simulation represents a relevant treatment, essentially this is step 6 in table 7.1. After a relevant simulated treatment was captured the means of further analysing the data to extract point dose and dose volume histograms had to be established. In the current thesis two methods were used to generate data comparators.

CMS XiO® DVH Analysis

In collaboration with Deloar Hossain of the Medical Physics and Bioengineering division of Christchurch Hospital the CMS XiO® treatment planning system was used to generate DVH data. The method relied upon using a feature of the proprietary CMS software that enabled the user to overlay a `3ddose` file on top of the import anonymised CT image series used in the DOSXYZnrc simulation. However, in the CMS XiO® case the entire DICOM image needed to be turned into a phantom to facilitate the overlaying of `3ddose` data. This created enormous phantom files that when divided into 2mm×2mm×3mm voxels required immensely long simulation times. Additionally, the editing of these large phantom files to insert high density shielding materials required many hours due to the CPU intensive task of reading approximately 50MB of ASCII data into MATLAB® and then writing the same volume of data to another ASCII file.

Although this technique was successful in producing the first of the treatment plan comparisons it was decided to find a more efficient means of data analysis. The key to finding a more efficient method was the realisation that the DICOM RT standard[2] contained structures that could be populated with Monte Carlo derived information. The adoption of the DICOM RT standard by most major suppliers of radiation oncology equipment was also a deciding factor in utilising the RT Dose object to overlay Monte

[2]DICOM RT (Digital Imaging and Communications in Medicine Radiation Therapy) is the DICOM standard with an additional subset of objects used to handle the transfer of data unique to the radiation oncology arena. The following five objects represent the current recognised DICOM RT standard:

- RT Structure set - Information related to anatomy such as isocenters and markers
- RT Image - Radiotherapy images such as DRRs, Simulation images, and Portal images
- RT Plan - Geometric and dosimetric data such as external beam components
- RT Dose - Dose data such as reference points and isodose curves
- RT Treatment Record - Historical record of all treatment data such that the process may be re-created at any given point in time

Carlo derived information.

CERR Analysis

The Computational Environment for Radiotherapy Research (CERR) from Washington University in St. Louis[43] was utilised in the DICOM RT analysis of the treatment plans generated by Monte Carlo means[3]. It allows the user to work independent of any commercial treatment planning system once the DICOM RT data set has been constructed. After the Monte Carlo analysis has been completed it is possible to export the modified DICOM RT data set back into the commercial treatment planning system although this was not done in the current thesis.

Generating DICOM RT plans in the Varian Eclipse treatment planning system was a matter of deciding upon a relevant calculation volume to encompass all simulated treatment sites and any penumbral regions of interest. This DICOM RT data set could then be exported and anonymised for importing into CERR. Once this was done it was necessary to find the equivalent subset of the DICOM image series and construct a `egsphant` file from it. In comparison to the CMS XiO® method this generated `egsphant` files of only a few MB, hence MATLAB® processing times and DOSXYZnrc simulation times were reasonable.

Overlaying the Monte Carlo `3ddose` files in CERR requires the generation of a matrix of dose values that aligns with the doseArray object in the DICOM RT data set. CERR contains a MATLAB® routine that allows the user to separate a `3ddose` file into dose and error matrices. Once that is complete the user needs to issue a MATLAB command that enables the overwriting of the doseArray object. The CERR environment can then be used to visualise and process the resultant DICOM RT data set with Monte Carlo generated dose overlayed.

Obtaining information about the Monte Carlo treatment simulations from CERR is similar to the way commercial treatment planning systems operate. Dose normalisation can be accomplished by selecting an appropriate normalisation point in the dose distribution. Contouring structures must be done before DVHs can be generated; in the current thesis the PTV contouring was done by Dr. David Hamilton. Once other structures of interest were contoured it is a trivial task to generate the DVH for each structure. Additionally point dose determination is a point and click type feature within the CERR environment and could be equally accomplished with an appropriated normalised `3ddose` displayed with the EGSnrc dose distribution viewing application `dosxyz_show`. In displaying the dose distributions the edited `egsphant` file densities cannot be overlayed upon the initial DICOM images, hence eye shields, surface lead and bolus inserted into the treatment field will not show; however, the dose distributions will ghost the outline of these tissue and high density regions.

7.2.2 kV Photon Dose Distributions

The following section details the kV photon distributions obtained through the use of the DOSXYZnrc user code coupled with the CERR environment. Due to the predomi-

[3]CERR is copyrighted to J. O. Deasy and Washington University in St Louis. A free license is granted to use or modify but only for uses which are non-commercial and non-clinical. In particular, clinical decisions should not be made based on the use of CERR.

nantly photoelectric means of interaction for the kV photons these dose distributions are expected to preferentially deposit dose in the high density regions of the treatment field. Additionally because of the neutral charge on the photon the penetration of the photon beam is expected to allow dose deposition well past the PTV.

For each of the following simulations the voxel size constrains the minimum thickness of this lead shield the current thesis shall consider a 2.5mm layer of lead present. The centre of the treatment field is defined as the centre of the PTV. The dose is normalised to 2Gy within an area of the PTV that has a low dose gradient. The dose distributions are presented for selected central slices from each DICOM RT data set.

Left Ear

The left ear field in the kV photon case is shaped by the placement of lead on the phantom surface. The field shape is roughly circular of diameter 6cm and encompasses the entire PTV.

The 100kV photon with 5cm diameter applicator phase-space file was used in the Monte Carlo simulation of dose deposition. A stand-off of 4cm was introduced for the field to fully encompass the area to be irradiated. Two cases are considered for irradiation of the left ear. Bolus has been modelled into the ear canal in one plan (see figure 7.3), whereas no bolus is present in the other plan (see figure 7.4).

Left Lateral Nose

The left lateral nose field in the kV photon case is shaped by the placement of lead on the phantom surface. The field shape presented to the beam is roughly circular of diameter 4cm and encompasses the entire PTV. This is a problematic field shape due to the oblique nature of the incident phase-space file. Planar views in most image processing applications only allow the three orthogonal views of the coronal, sagittal and transverse aspects.

The 80kV photon with 3cm diameter applicator phase-space file was used in the Monte Carlo simulation of dose deposition. A stand-off of 2cm was introduced to accommodate the patient contour as it is physically impossible to bring the applicator closer to the treatment site. See figure 7.5 for detail of the dose distribution.

Right Medial Canthus

The right medial canthus field in the kV photon case is shaped by the placement of lead on the phantom surface. The field shape roughly circular of diameter 2.5cm and encompasses the entire PTV.

For shielding of the radiosensitive eye a lead eye shield is inserted into the `egsphant` file. Due to the constraint of the 2.5mm voxel dimension the accurate modelling of the eye shield is somewhat limited. However it is not the intent of the current thesis to fully investigate the dosimetry surrounding the high density shielding materials as this has already been discussed in the literature [44][45].

The 100kV photon with 3cm diameter applicator phase-space file was used in the Monte Carlo simulation of dose deposition. A stand off of 2cm was used as the patient contour prevents the closer placement of the applicator. See figure 7.6 for detail of the dose distribution.

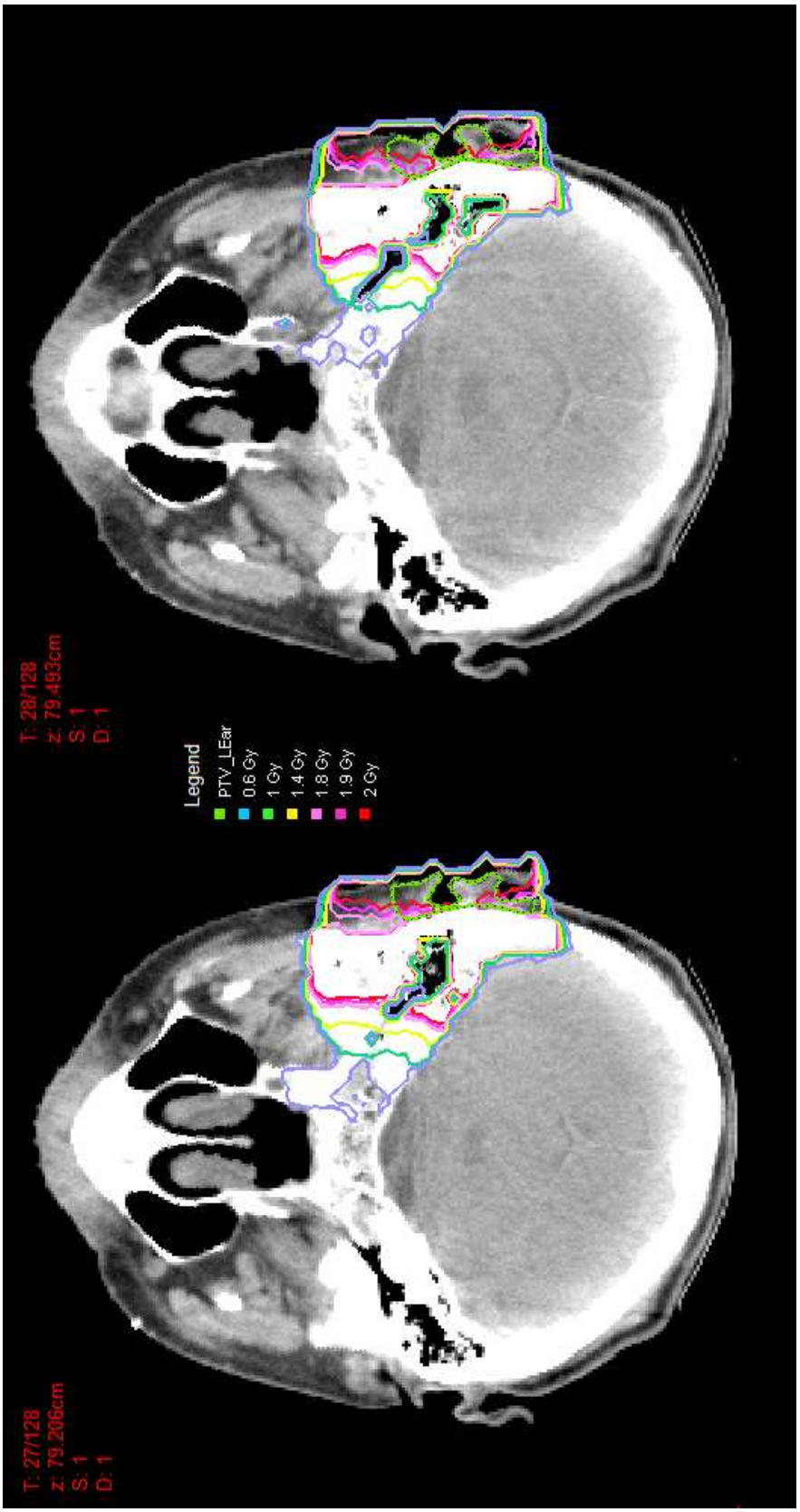
T: 28/128
z: 79.493cm
S: 1
D: 1
Legend
PTV_LEar
0.6 Gy
1 Gy
1.4 Gy
1.8 Gy
1.9 Gy
2 Gy
T: 27/128
z: 79.206cm
S: 1
D: 1

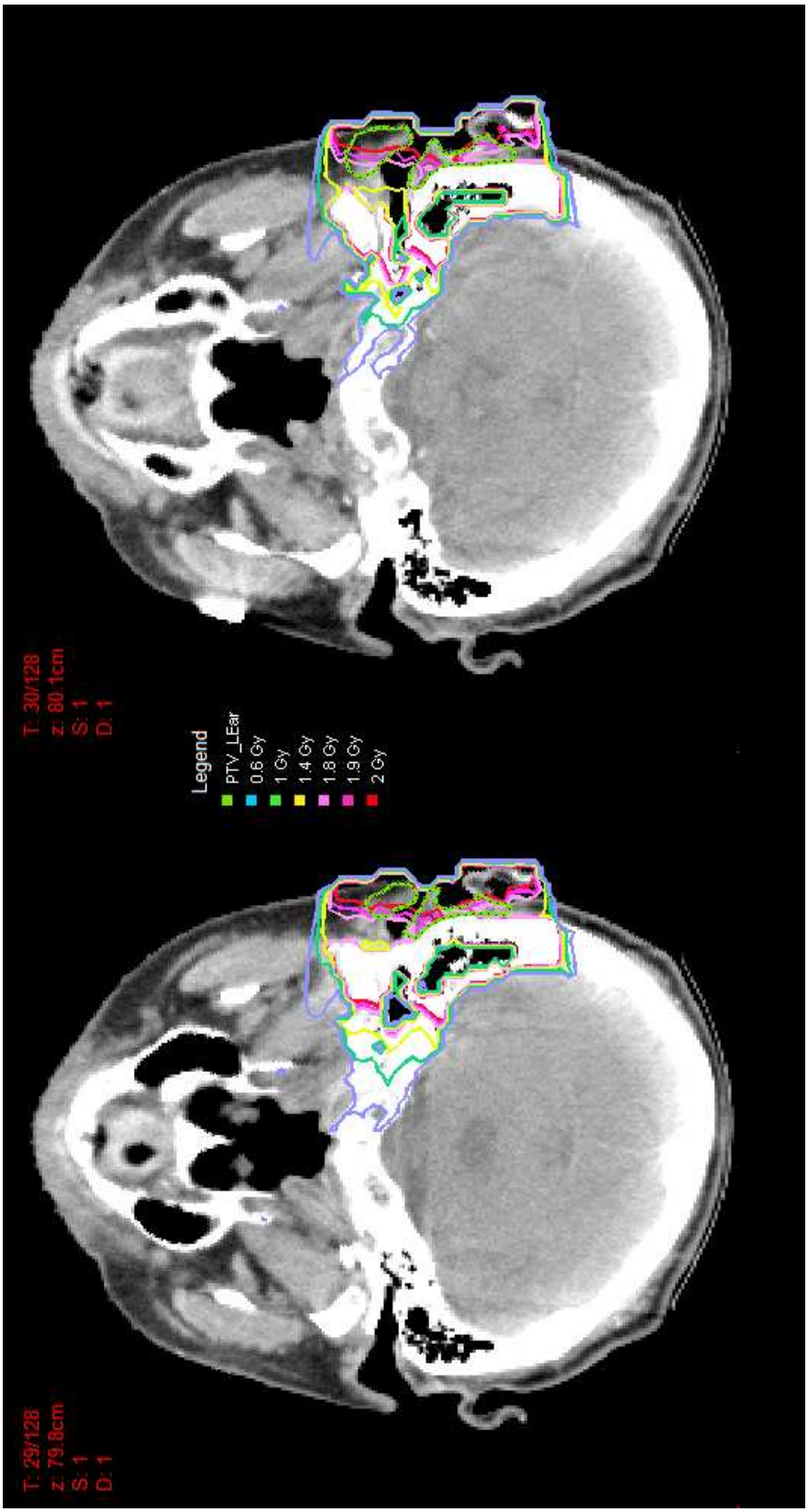
T: 30/128
z: 80.1cm
S: 1
D: 1
Legend
PTV_LEar
0.6 Gy
1 Gy
1.4 Gy
1.8 Gy
1.9 Gy
2 Gy
T: 29/128
z: 79.8cm
S: 1
D: 1

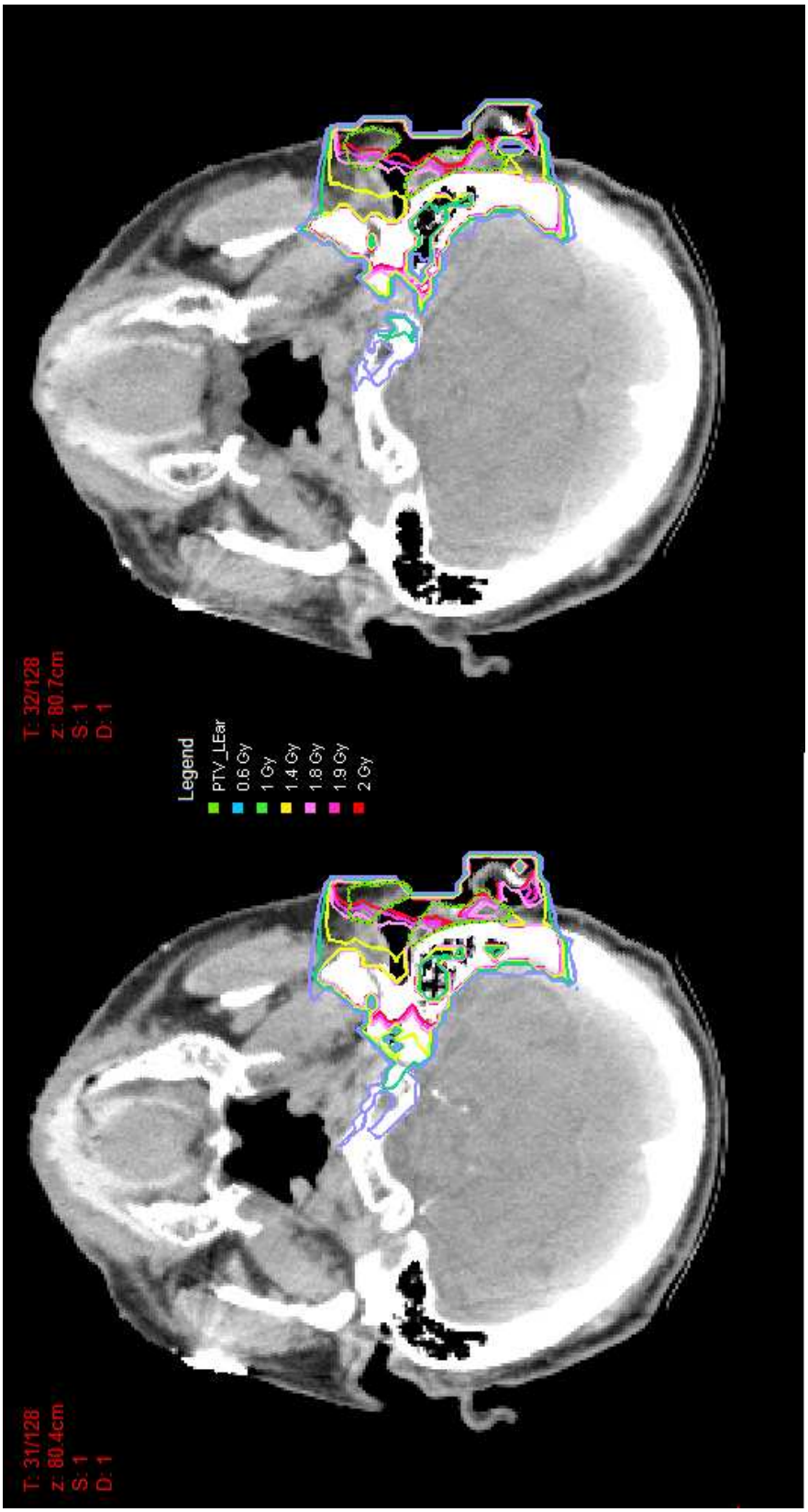

Figure 7.3: Dose distributions of 100kV photon field on left ear field with bolus insert in the ear canal

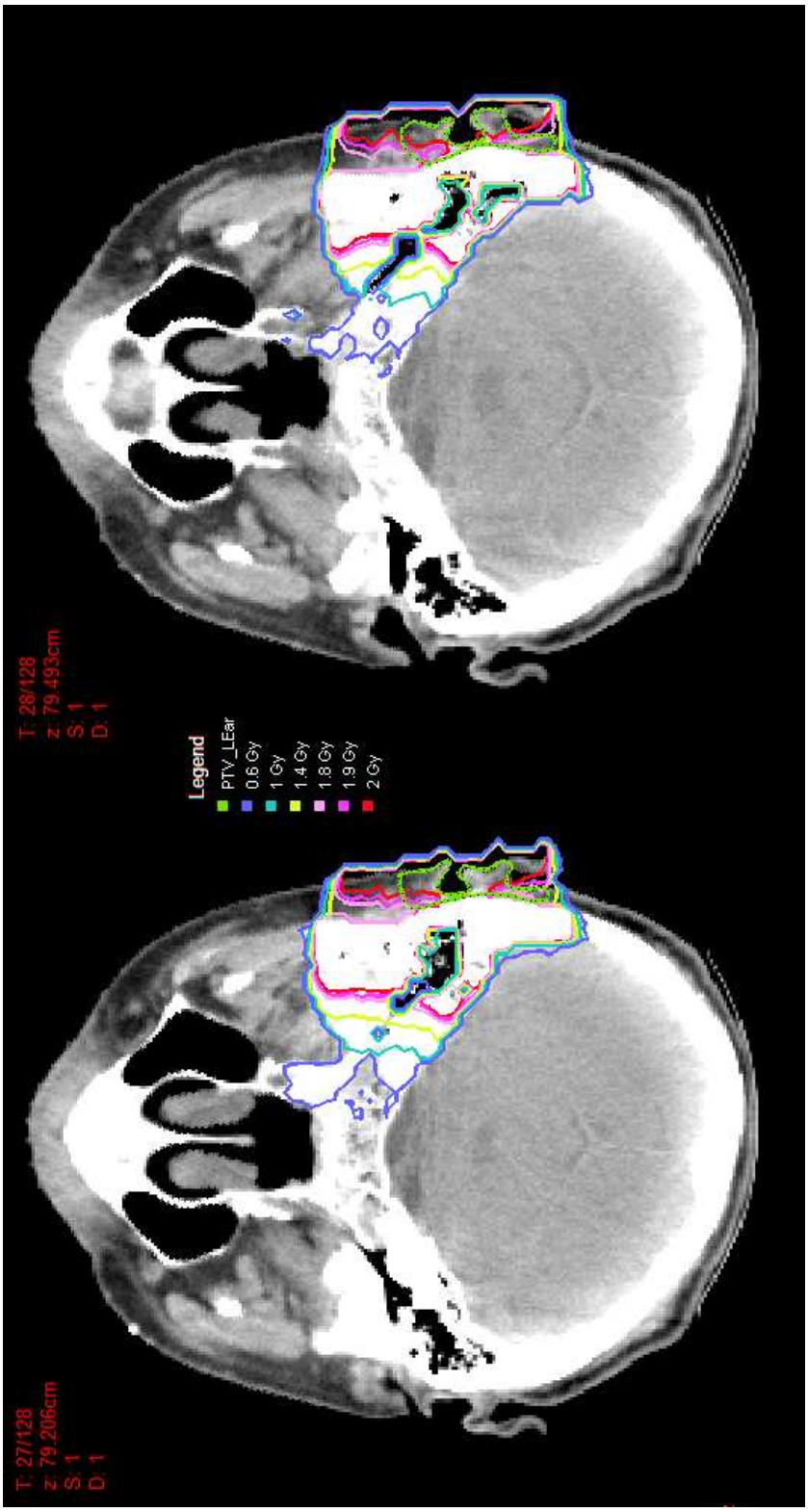
T: 28/128
z: 79.493cm
S: 1
D: 1
Legend
PTV_LEar
0.6 Gy
1 Gy
1.4 Gy
1.8 Gy
1.9 Gy
2 Gy
T: 27/128
z: 79.206cm
S: 1
D: 1

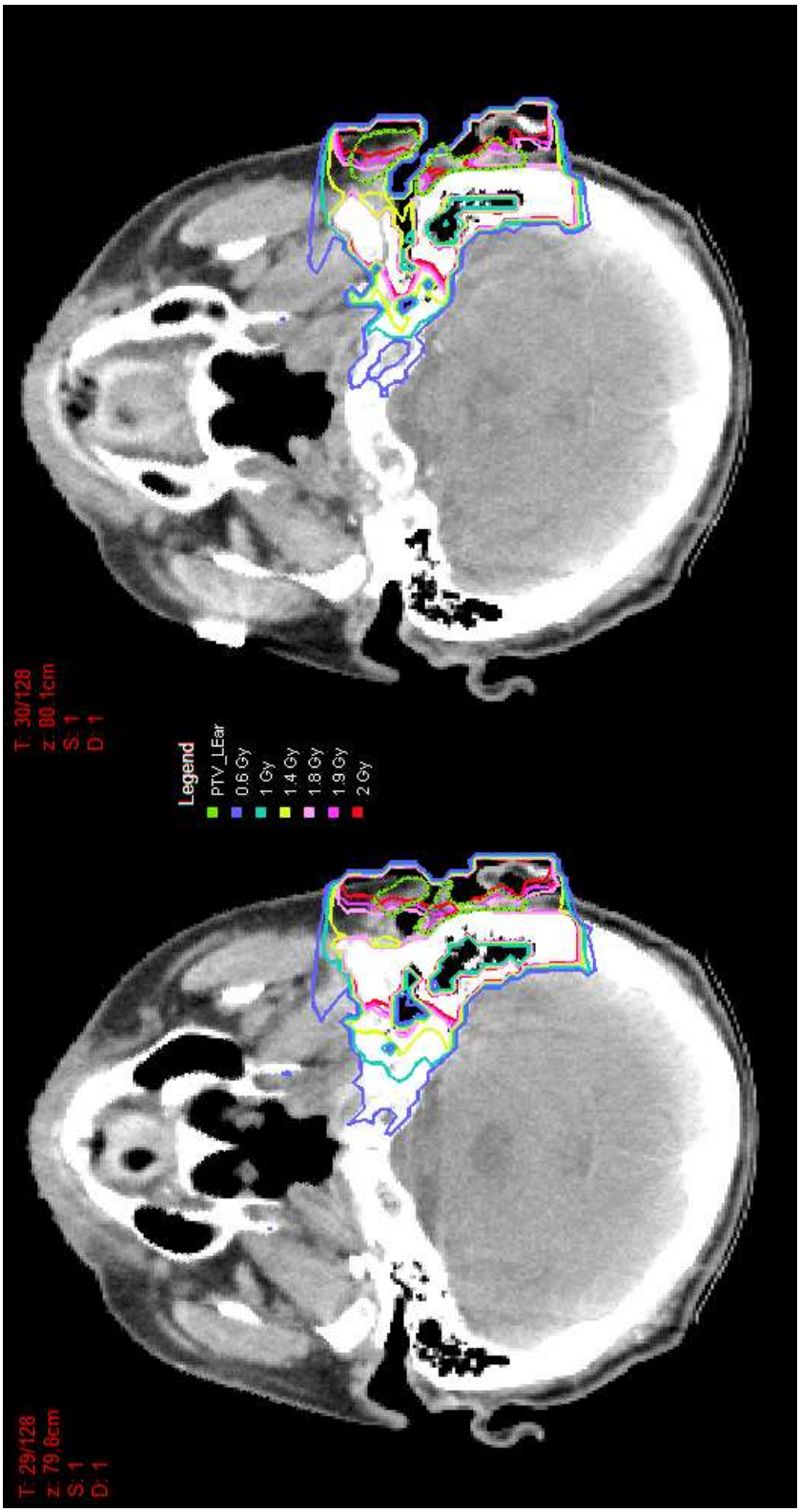
T: 30/128
z: 80.1cm
S: 1
D: 1
Legend
PTV_LEar
0.6 Gy
1 Gy
1.4 Gy
1.8 Gy
1.9 Gy
2 Gy
T: 29/128
z: 79.6cm
S: 1
D: 1

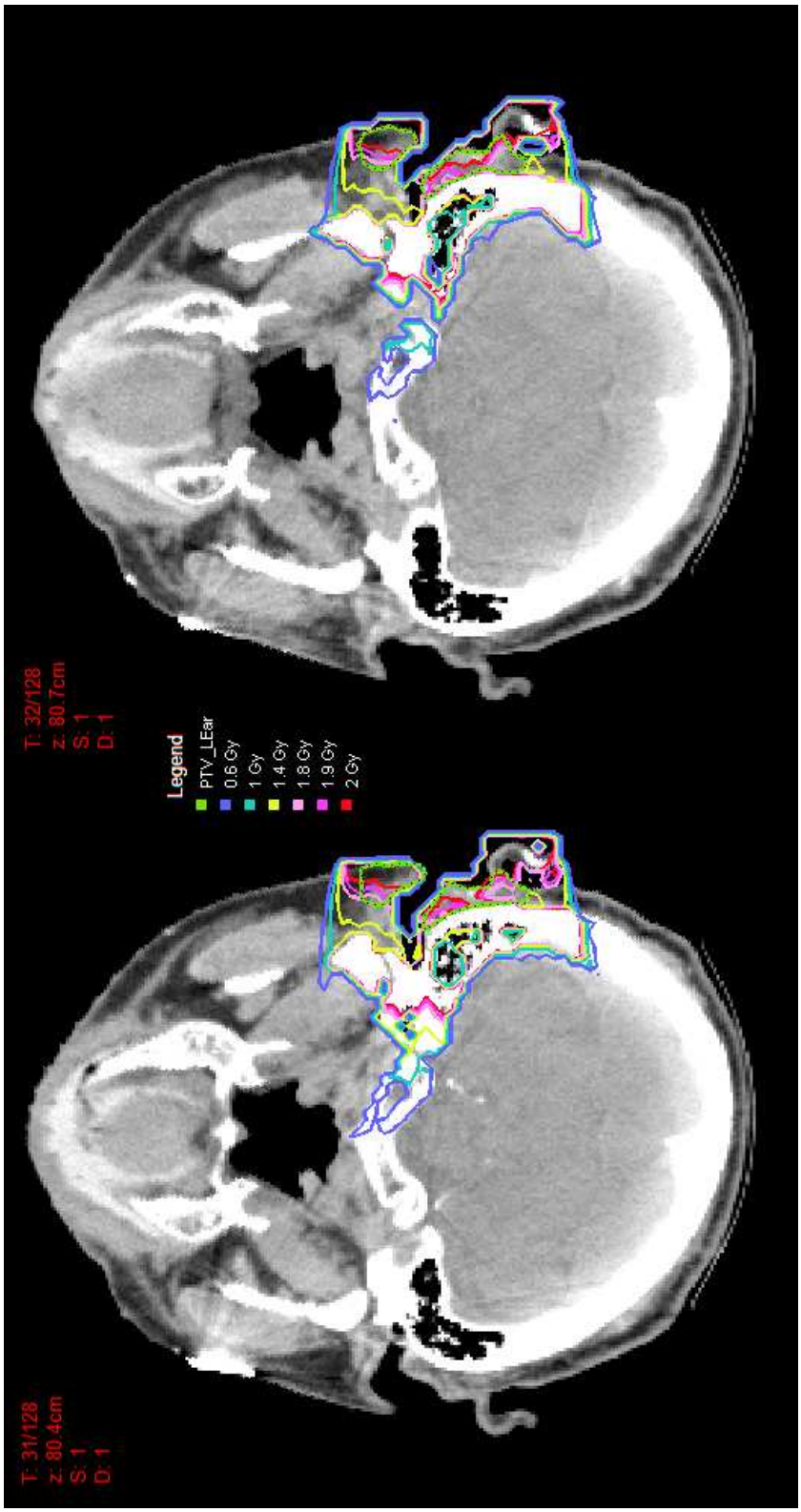

Figure 7.4: Dose distributions of 100kV photon field on left ear field without bolus insert in the ear canal

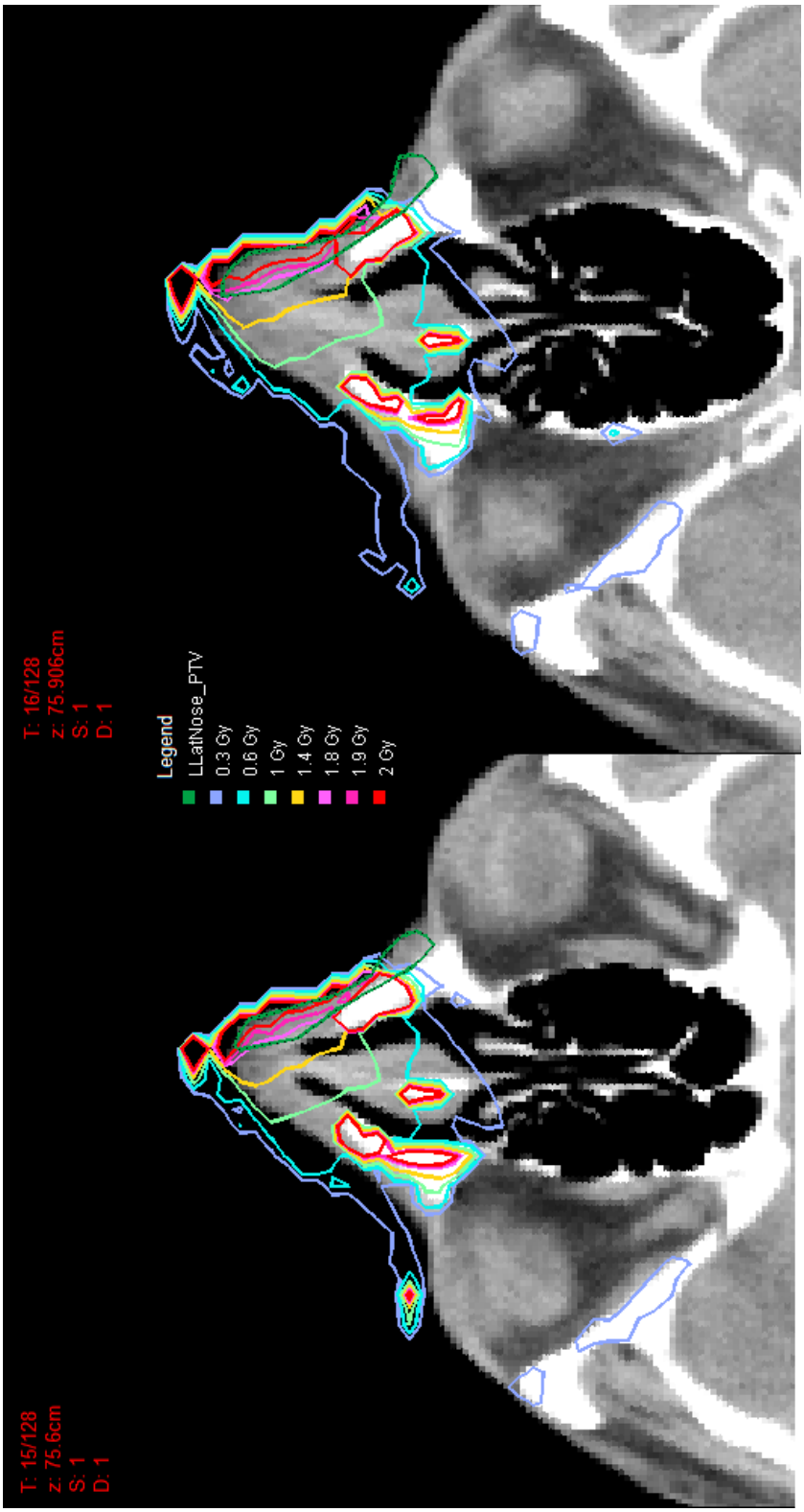
T: 16/128
z: 75.906cm
S: 1
D: 1
Legend
LLatNose_PTV
0.3 Gy
0.6 Gy
1 Gy
1.4 Gy
1.8 Gy
1.9 Gy
2 Gy
T: 15/128
z: 75.6cm
S: 1
D: 1

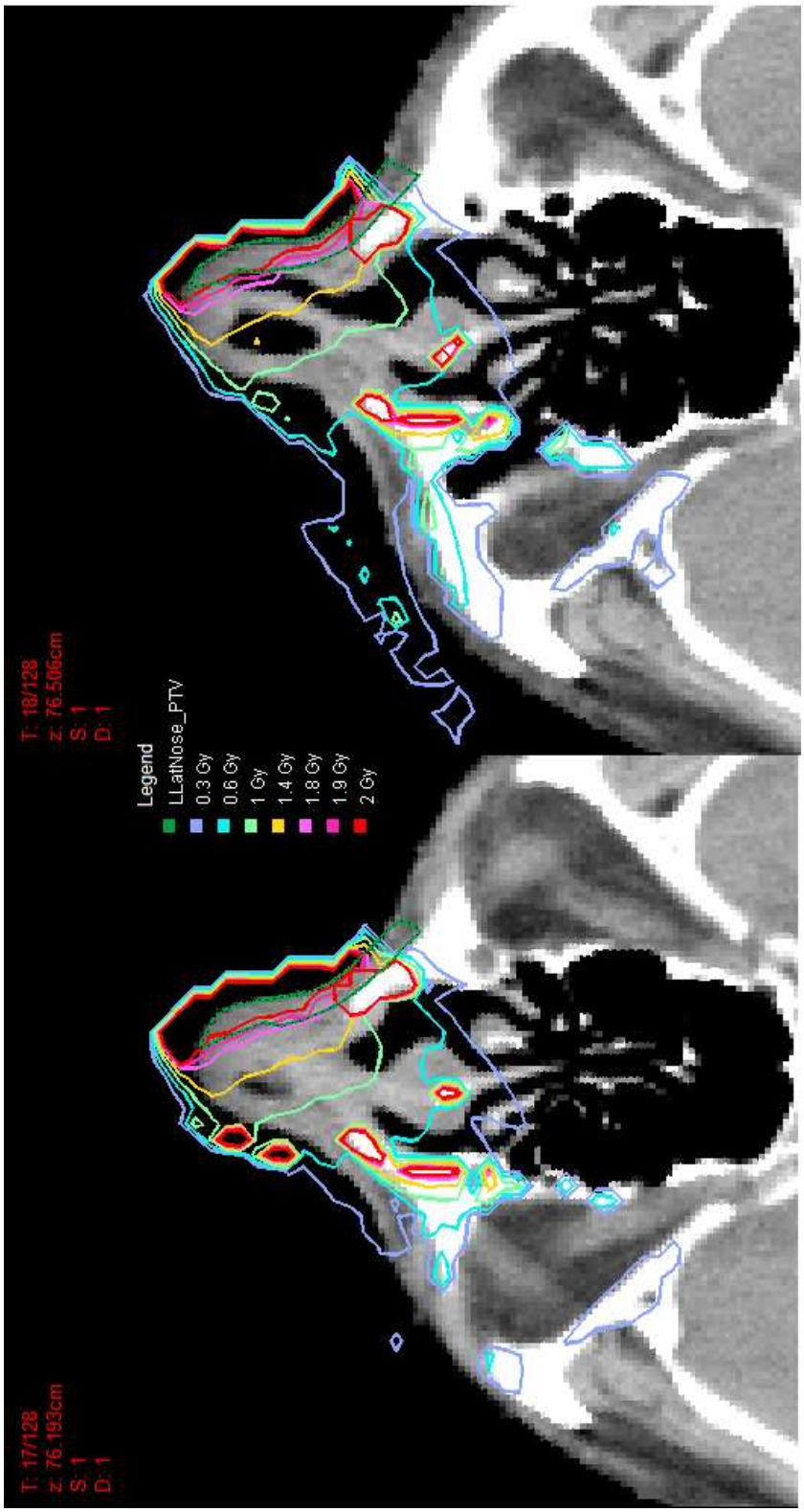
T: 18/128
z: 76.506cm
S: 1
D: 1
Legend
LLatNose_PTV
0.3 Gy
0.6 Gy
1 Gy
1.4 Gy
1.8 Gy
1.9 Gy
2 Gy
T: 17/128
z: 76.193cm
S: 1
D: 1

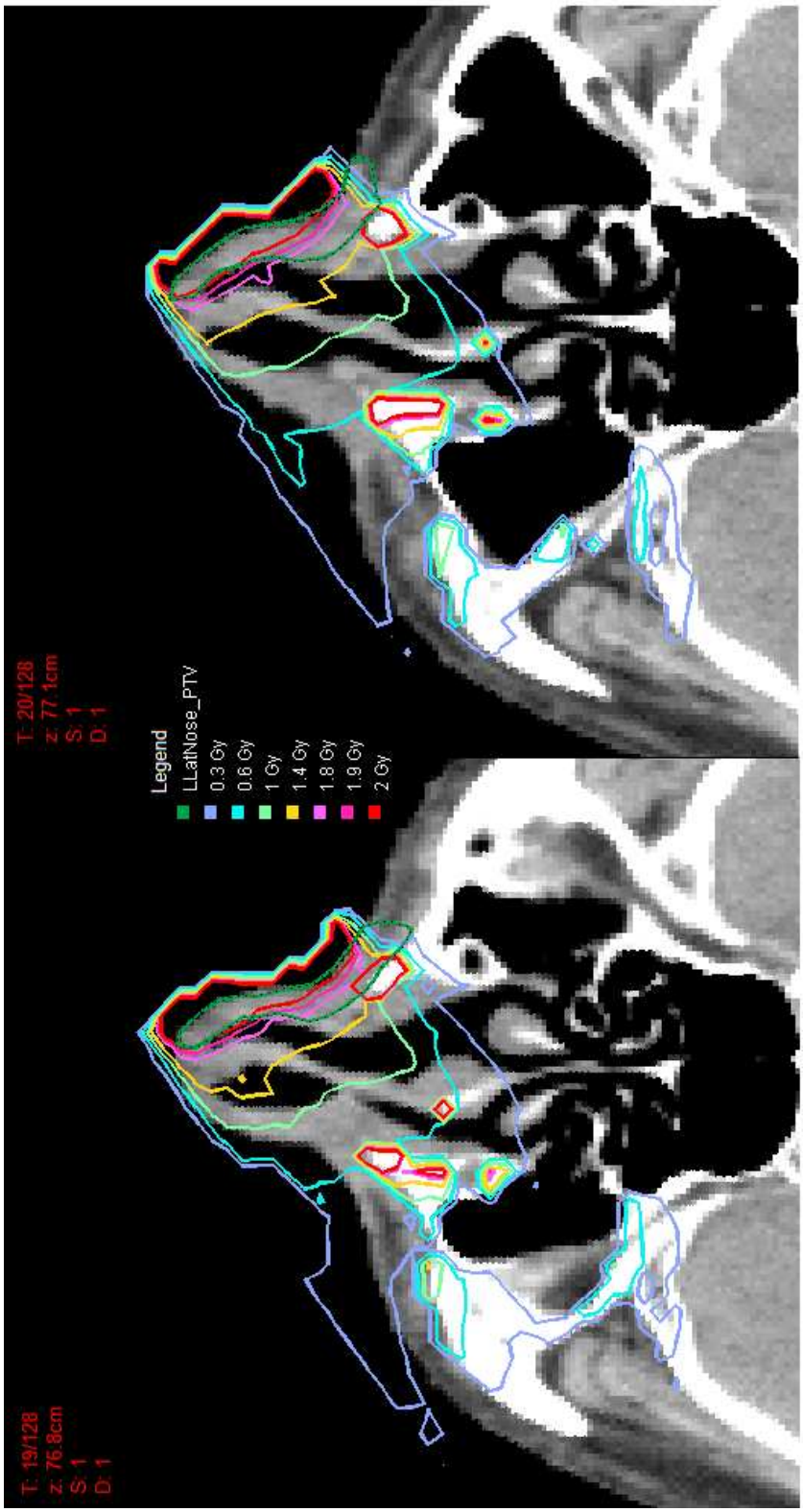

Figure 7.5: Dose distributions of 80kV photon field on left lateral nose

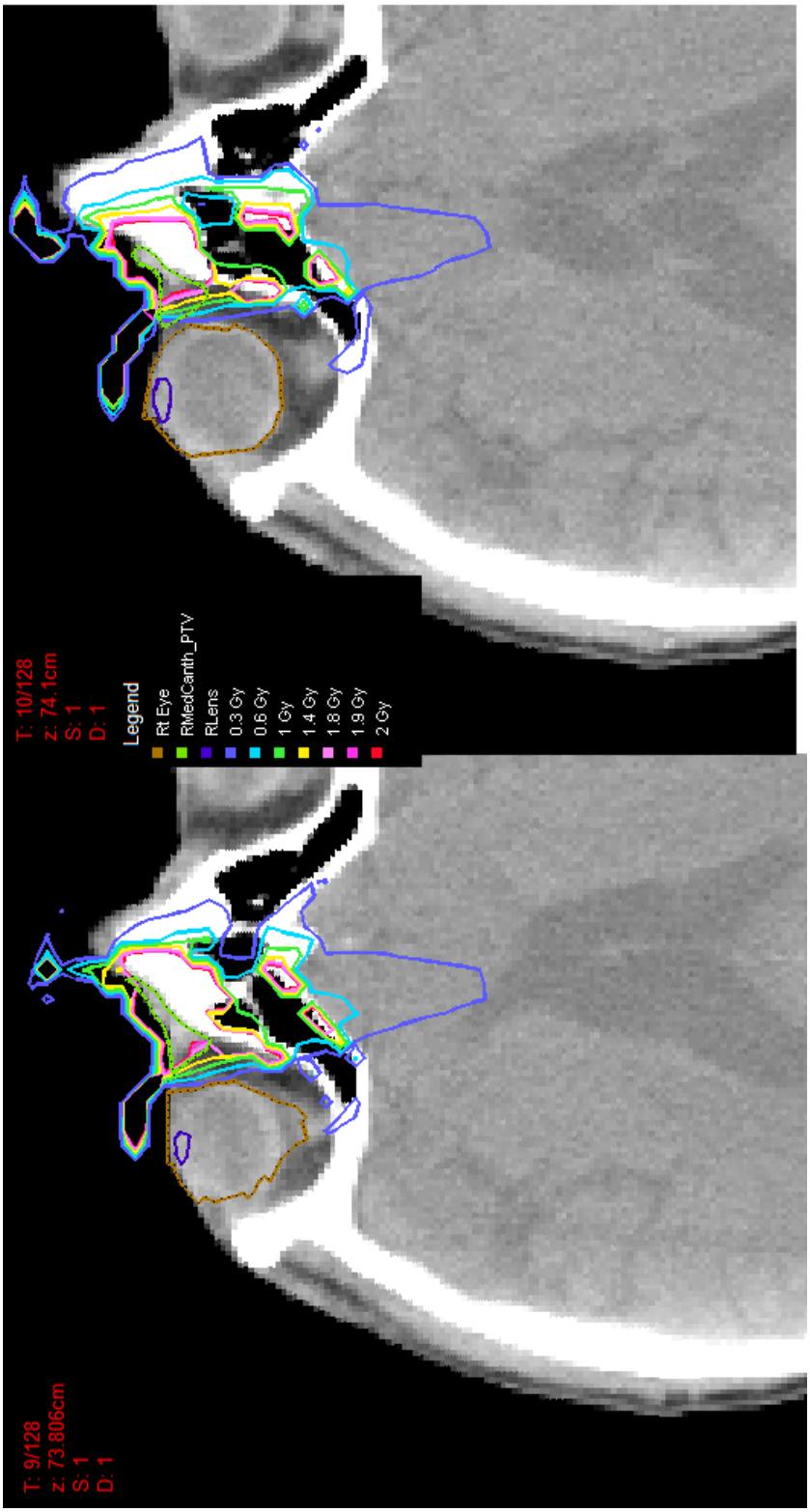
T: 10/128
z: 74.1cm
S: 1
D: 1
Legend
Rt Eye
RMedCanth_PTV
RLens
0.3 Gy
0.6 Gy
1 Gy
1.4 Gy
1.8 Gy
1.9 Gy
2 Gy
T: 9/128
z: 73.806cm
S: 1
D: 1

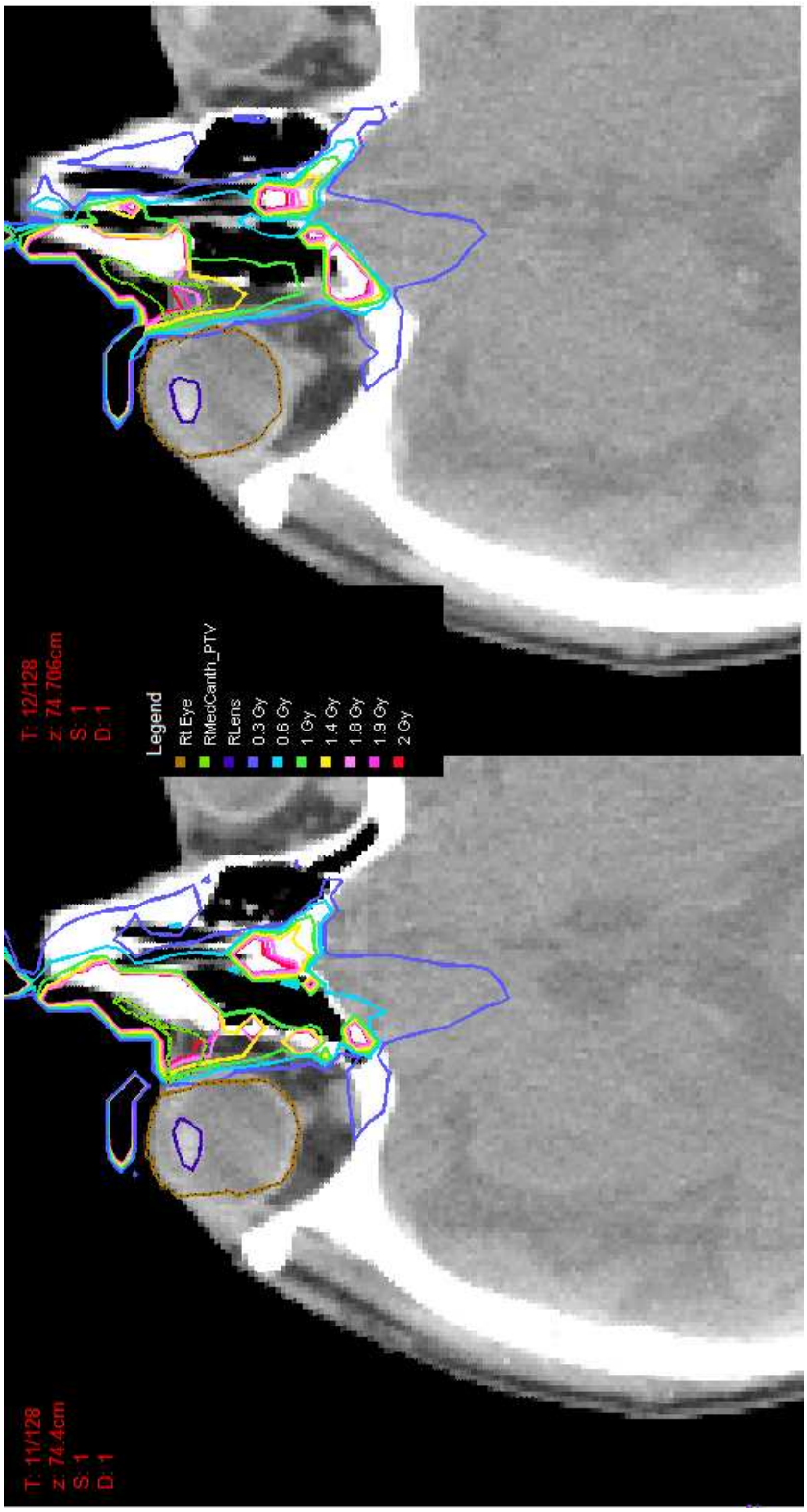
T: 12/128
z: 74.706cm
S: 1
D: 1
Legend
Rt Eye
RMedCanth_PTV
RLens
0.3 Gy
0.6 Gy
1 Gy
1.4 Gy
1.8 Gy
1.9 Gy
2 Gy
T: 11/128
z: 74.4cm
S: 1
D: 1

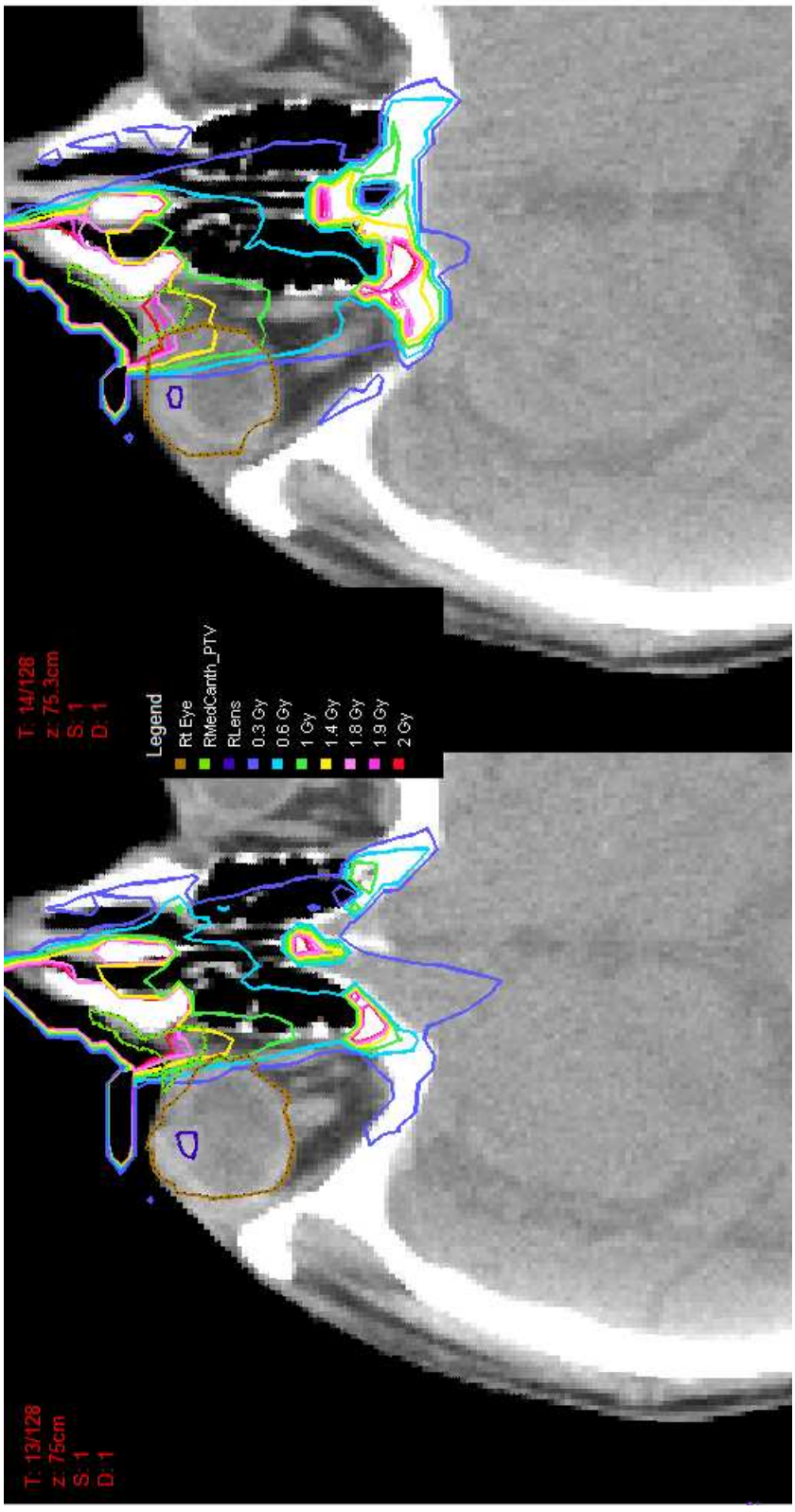

Figure 7.6: Dose distributions of 100kV photon field on right medial canthus with lead eye shield inserted

The kV photon dose distributions exhibit a number of features:

- Sharp penumbral boundaries - a feature of the neutral nature of the photon, very little lateral spread is seen in the first few centimeters of the dose distribution as the number of secondary electrons liberated that have sufficient energy to wander outside of the penumbral region is low.
- Hot spots above bone and cartilage - a feature of the dominant photoelectric effect for kV energies. This can lead to complications in the treatment site such as necrosis of the overlaying tissue even though it may contain the PTV.
- Effective attenuation by lead - the 2.5mm lead thickness modelled in the current investigation adequately shields underlying radiosensitive structures. However, the true dimensions of the eye shields are of the order of 1.7mm thickness[4] which allows for 1% transmission at 120kVp (3mm Al HVL). Additionally the size must be small enough for the shield to be accommodate for the course of treatment under a patient's eyelid.
- Long photon tail - the dose distributions have a low energy component that extends for several centimeters past the PTV. This low energy component typically extends into the brain which is quite radioresistant

7.2.3 MeV Electron Dose Distributions

The following section details the MeV electron distributions obtained through the use of the DOSXYZnrc user code coupled with the CERR environment. In contrast to the photon case the predominant interaction in the MeV energy range is via interaction processes independent of atomic number. Thus dose deposition in the high and low density regions of the treatment field is expected to show a more homogeneous distribution. Additionally, because of the charge on the electron the penetration of the electron beam is expected to be quite shallow and largely constrained to the area of the PTV. There is a slight build up region for the MeV electron fields as well (see figures 6.24 and 6.25), this has been accounted for by the insertion of bolus into the phantom.

For each of the following simulations the voxel size constrains the minimum thickness of either tungsten eye shielding or bolus present in the treatment field. For each patient 1cm of bolus was added to the treatment field. The nominal energy of the electron field for all of the simulations presented is 6MeV. The centre of the treatment field is defined as the centre of the PTV. The dose is normalised to 2Gy within an area of the PTV that has a low dose gradient. The dose distributions are presented for selected central slices from each DICOM RT data set.

Left Ear

The left ear field in the MeV electron case is shaped by a Cerrobend® in the 6cm × 6cm applicator. The field shape is roughly circular of diameter 5cm and encompasses the entire PTV. A stand-off of 4cm was introduced for the field to fully encompass the area to be irradiated and exclude as much penumbra from the PTV. Two cases are considered

[4]Radiation Products Design Inc. silver plated eye shields #934-014 are quoted as 1.7mm thick

for irradiation of the left ear. Bolus has been modelled into the ear canal in one plan (see figure 7.7), whereas no bolus is present in the other plan (see figure 7.8).

Left Lateral Nose

The left lateral nose field in the MeV electron case is shaped by a Cerrobend® in the 6cm × 6cm applicator. The field shape is roughly circular of diameter 4cm and encompasses the entire PTV. As the field size decreases the d_{max} starts migrating towards the surface and the penumbral regions start to dominate the dose distribution, this is therefore the smallest field size considered for electrons in the current investigation. A stand-off of 2cm was introduced to accommodate the patient contour as it is physically impossible to bring the applicator closer to the treatment site. See figure 7.9 for detail of the dose distribution.

Right Medial Canthus

The right medial canthus field in the MeV electron case is shaped by a Cerrobend® in the 6cm × 6cm applicator. The field shape roughly circular of diameter 4cm and encompasses the entire PTV. A stand off of 2cm was used as the patient contour prevents the closer placement of the applicator. See figure 7.10 for detail of the dose distribution.

For shielding of the radiosensitive eye a tungsten eye shield is inserted into the `egsphant` file. Due to the constraint of the 2.5mm voxel dimension the accurate modelling of the eye shield is somewhat limited. However it is not the intent of the current thesis to fully investigate the dosimetry surrounding the high density shielding materials as this has already been discussed in the literature [44][45].

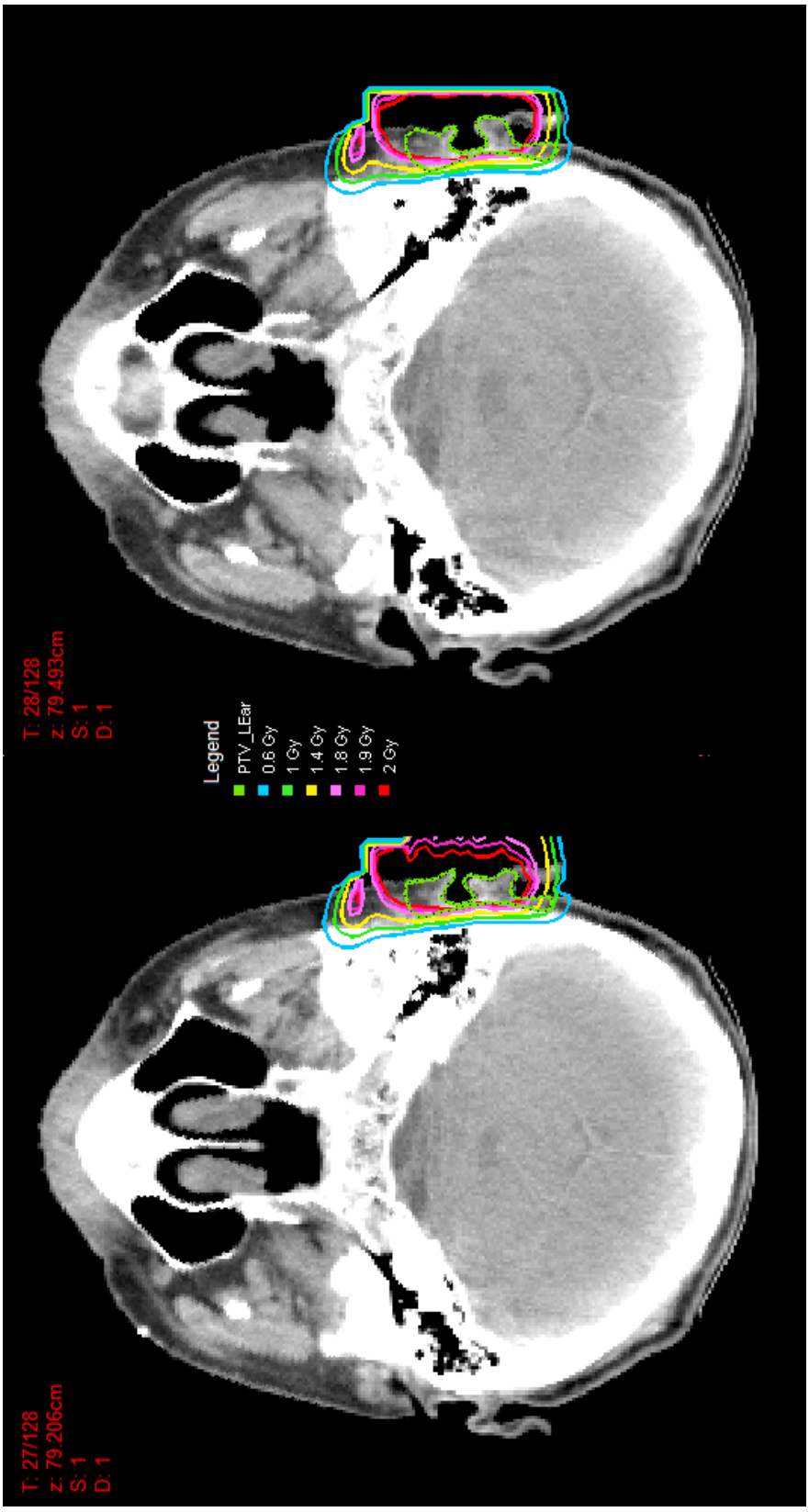
T: 28/128
z: 79.493cm
S: 1
D: 1
Legend
PTV_LEar
0.6 Gy
1 Gy
1.4 Gy
1.8 Gy
1.9 Gy
2 Gy
T: 27/128
z: 79.206cm
S: 1
D: 1

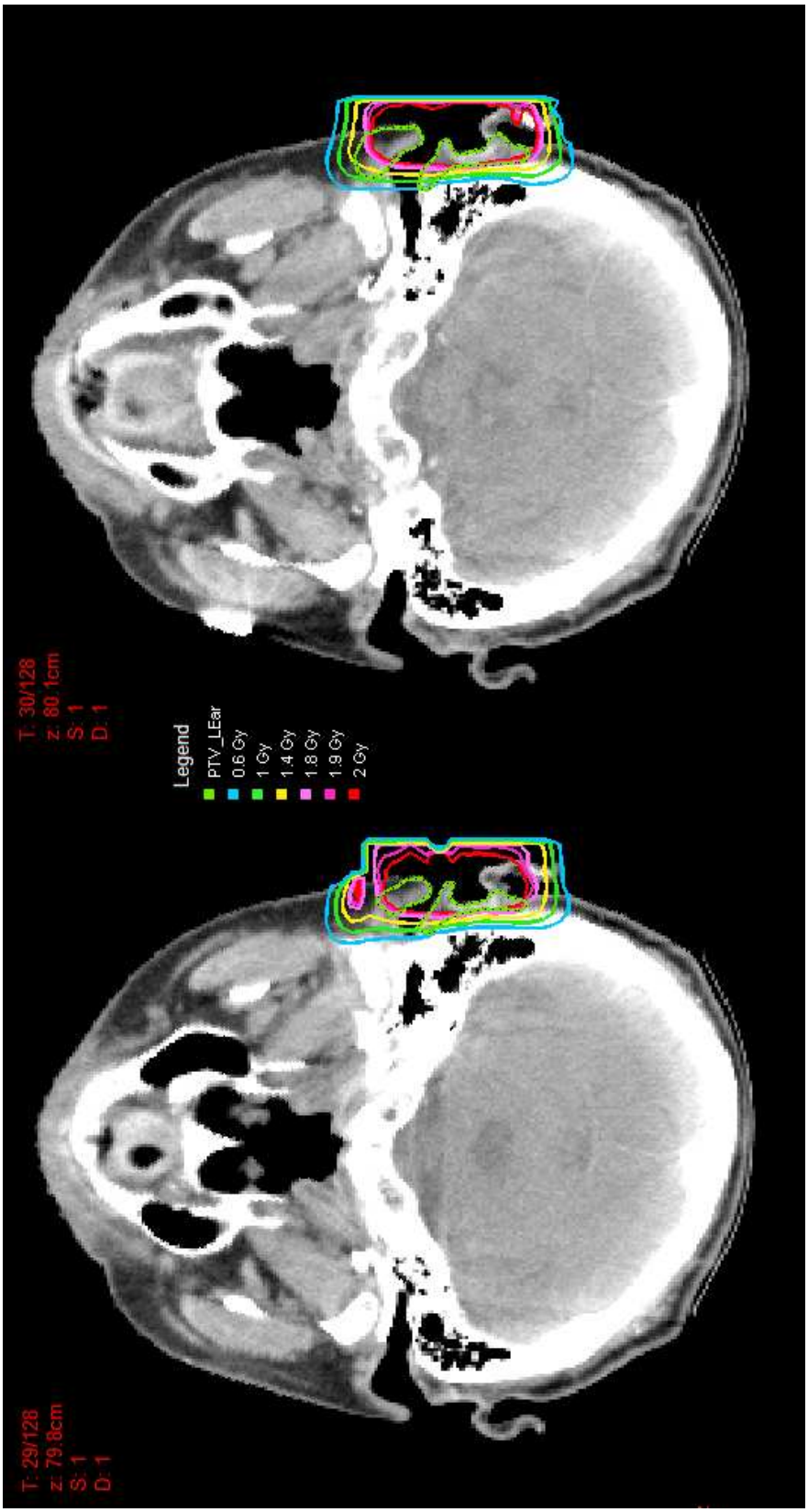
T: 30/128
z: 80.1cm
S: 1
D: 1
Legend
PTV_LEar
0.6 Gy
1 Gy
1.4 Gy
1.8 Gy
1.9 Gy
2 Gy
T: 29/128
z: 79.8cm
S: 1
D: 1

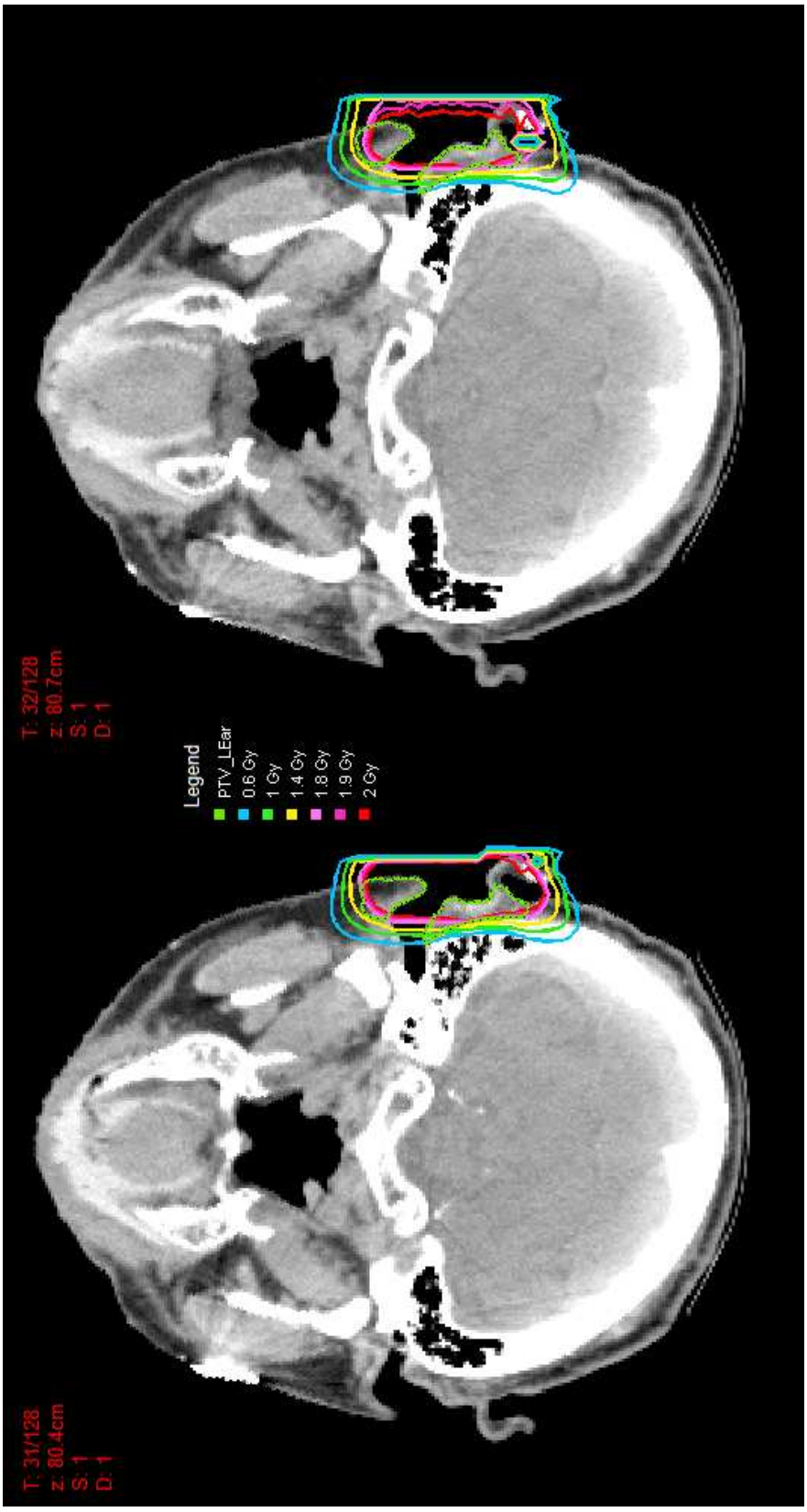

Figure 7.7: Dose distributions of 6MeV electron field on left ear field with bolus insert in the ear canal

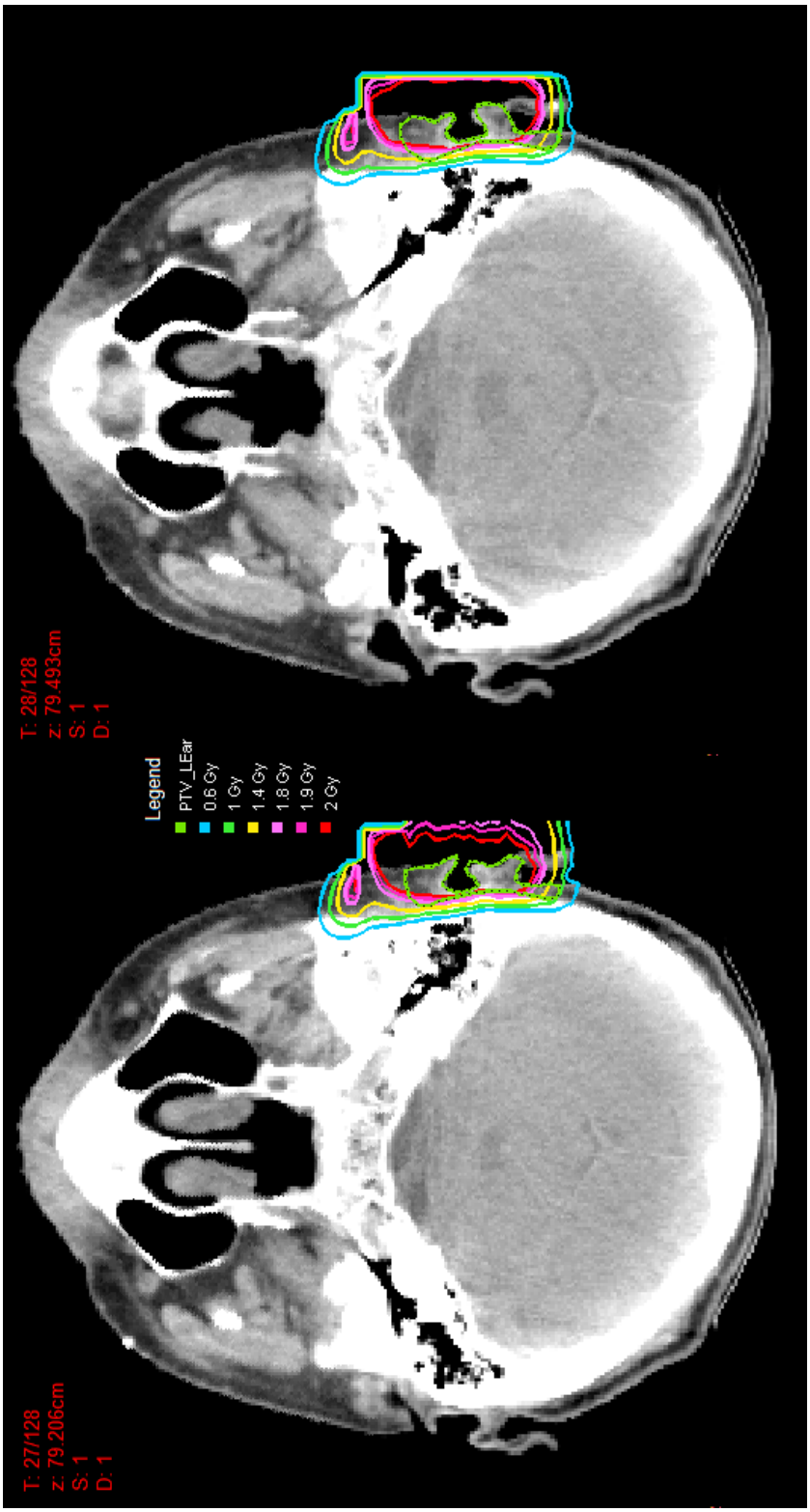
T: 28/128
z: 79.493cm
S: 1
D: 1
Legend
PTV_LEar
0.6 Gy
1 Gy
1.4 Gy
1.8 Gy
1.9 Gy
2 Gy
T: 27/128
z: 79.206cm
S: 1
D: 1

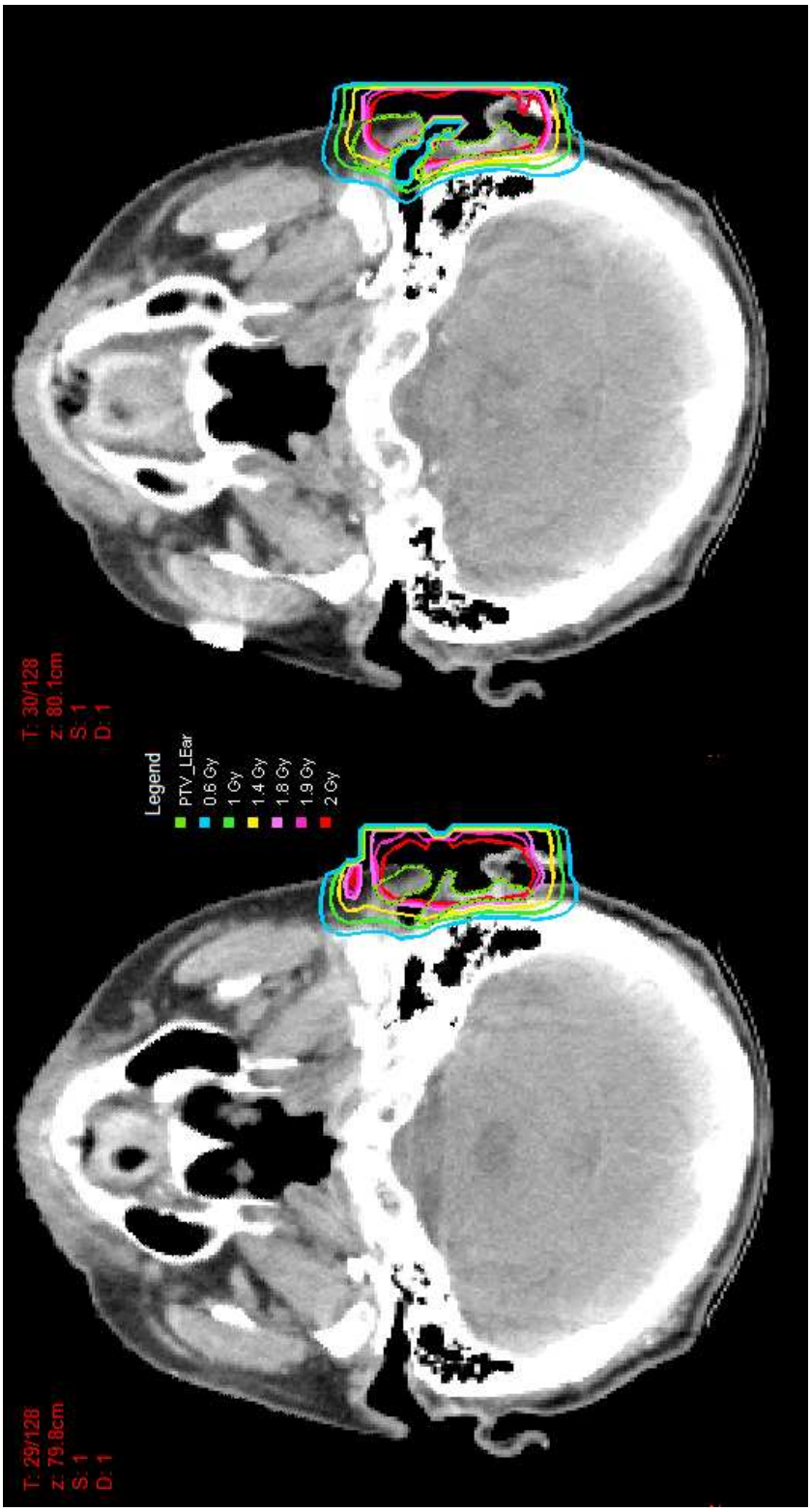
T: 30/128
z: 80.1cm
S: 1
D: 1
Legend
PTV_LEar
0.6 Gy
1 Gy
1.4 Gy
1.8 Gy
1.9 Gy
2 Gy
T: 29/128
z: 79.8cm
S: 1
D: 1

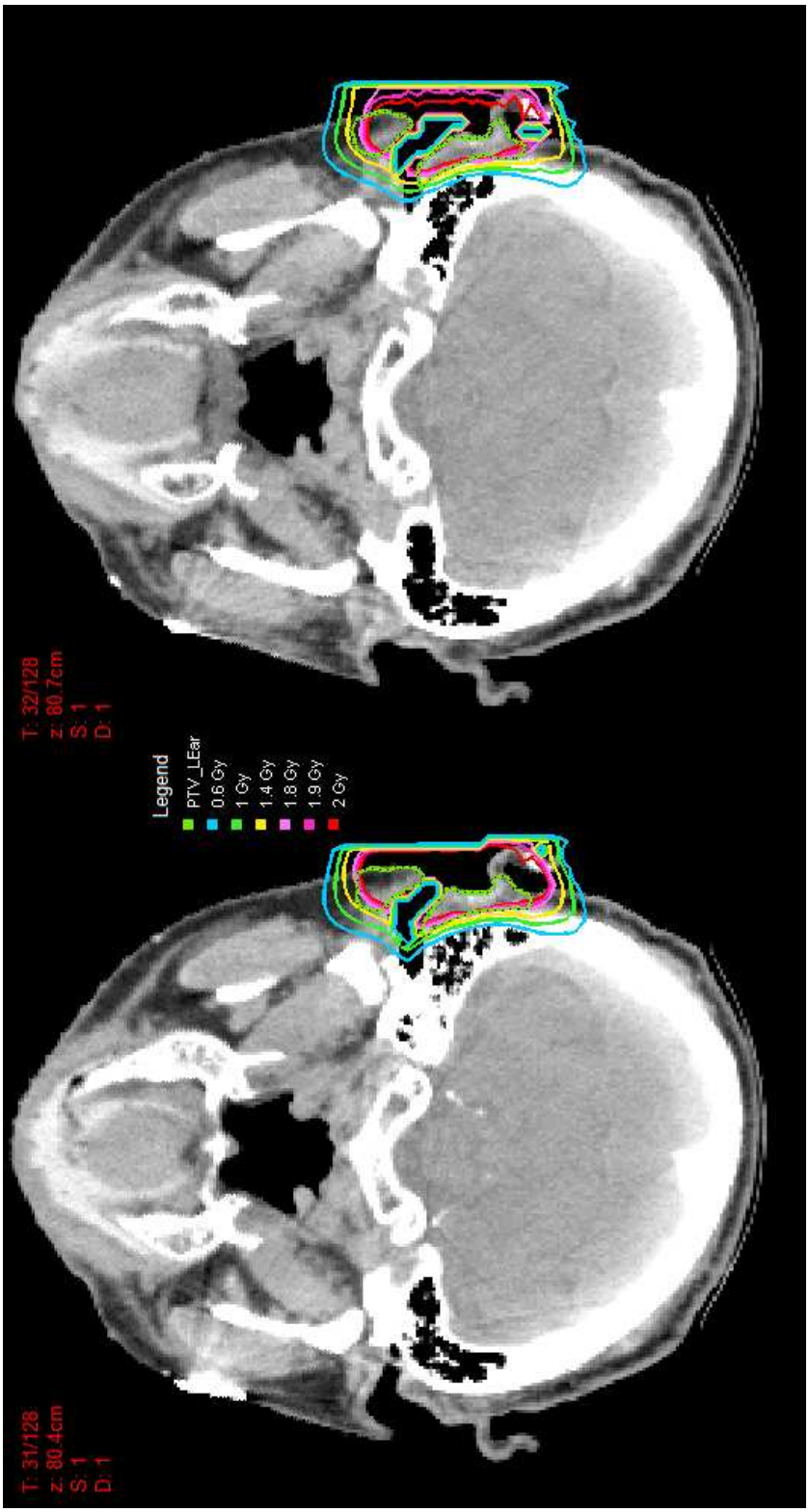

Figure 7.8: Dose distributions of 6MeV electron field on left ear field without bolus insert in the ear canal

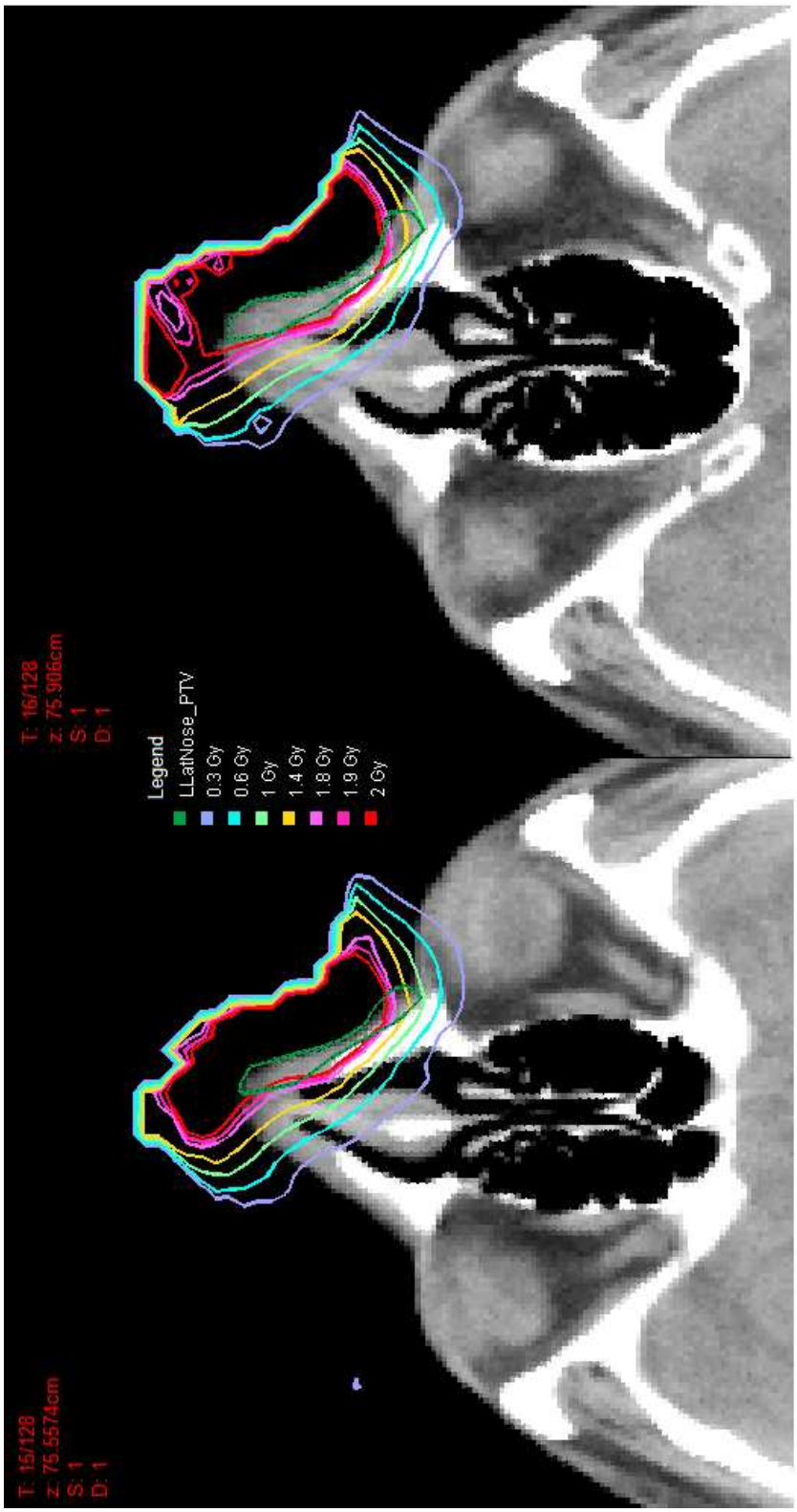
T: 16/128
z: 75.906cm
S: 1
D: 1
Legend
LLatNose_PTV
0.3 Gy
0.6 Gy
1 Gy
1.4 Gy
1.8 Gy
1.9 Gy
2 Gy
T: 15/128
z: 75.5574cm
S: 1
D: 1

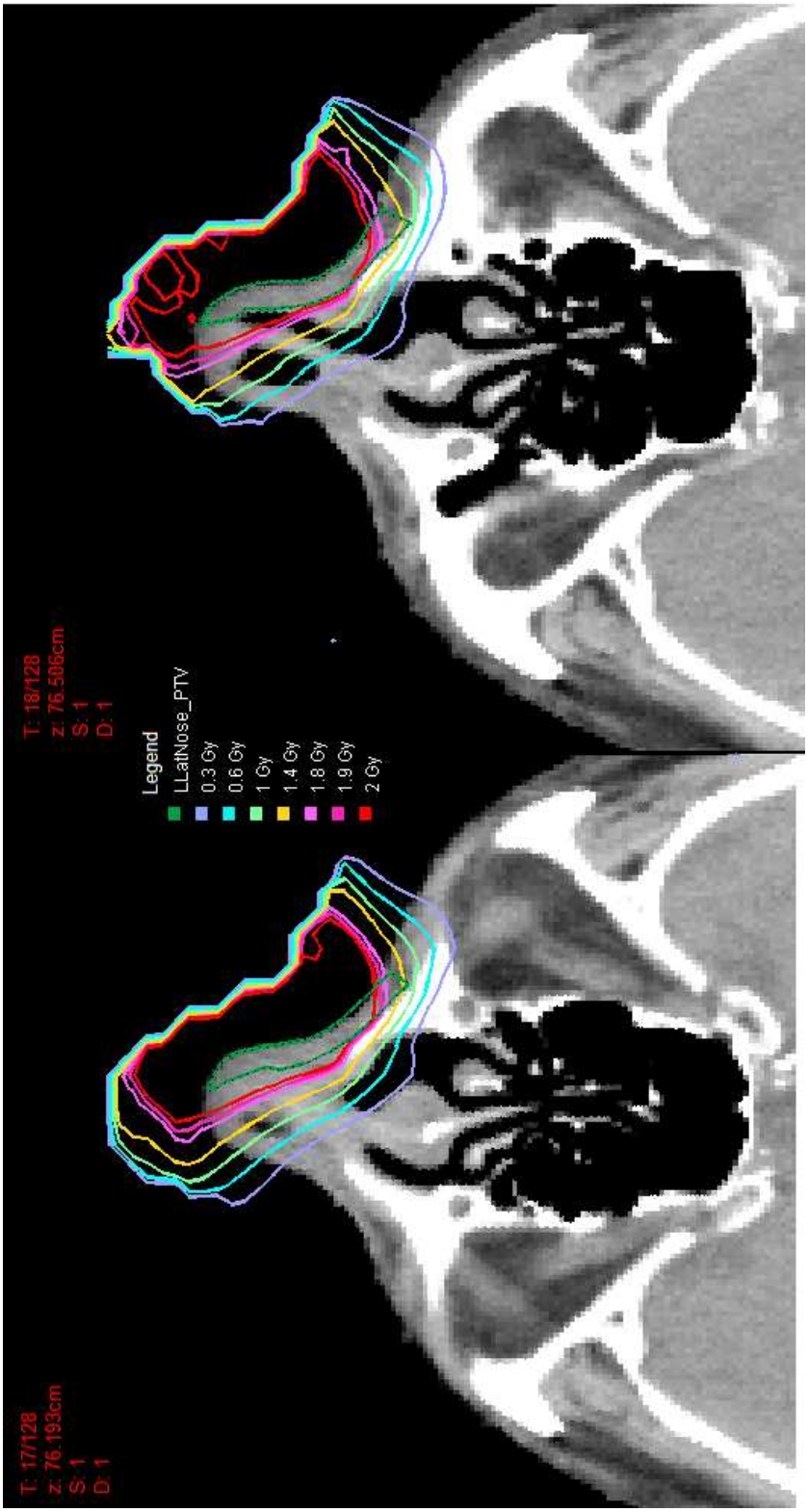
T: 18/128
z: 76.506cm
S: 1
D: 1
Legend
LLatNose_PTV
0.3 Gy
0.6 Gy
1 Gy
1.4 Gy
1.8 Gy
1.9 Gy
2 Gy
T: 17/128
z: 76.193cm
S: 1
D: 1

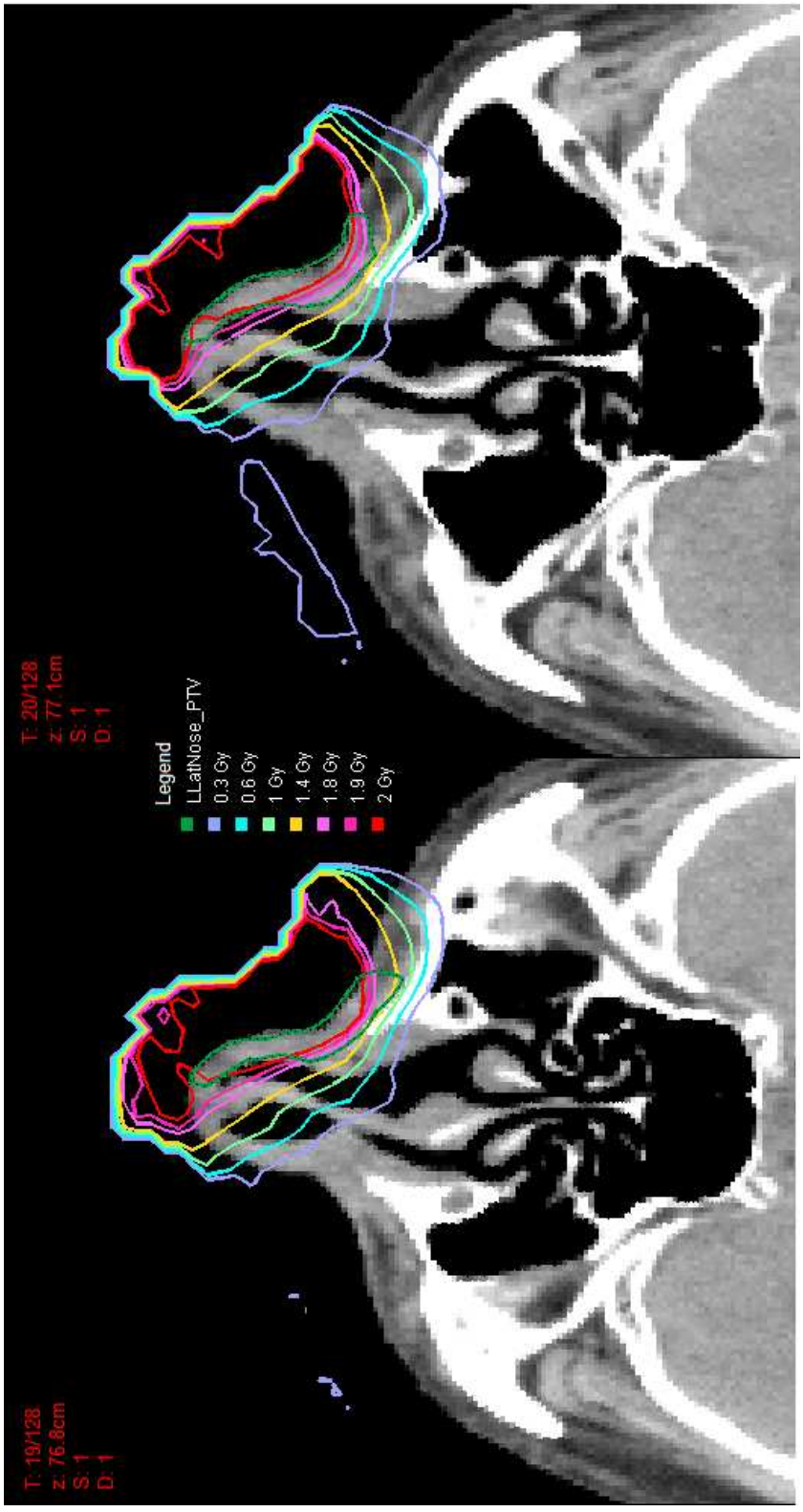

Figure 7.9: Dose distributions of 6MeV electron field on left lateral nose


T: 10/128
z: 74.1cm
S: 1
D: 1
Legend
Rt Eye
RMedCanth_PTV
RLens
0.3 Gy
0.6 Gy
1 Gy
1.4 Gy
1.8 Gy
1.9 Gy
2 Gy
T: 9/128
z: 73.806cm
S: 1
D: 1

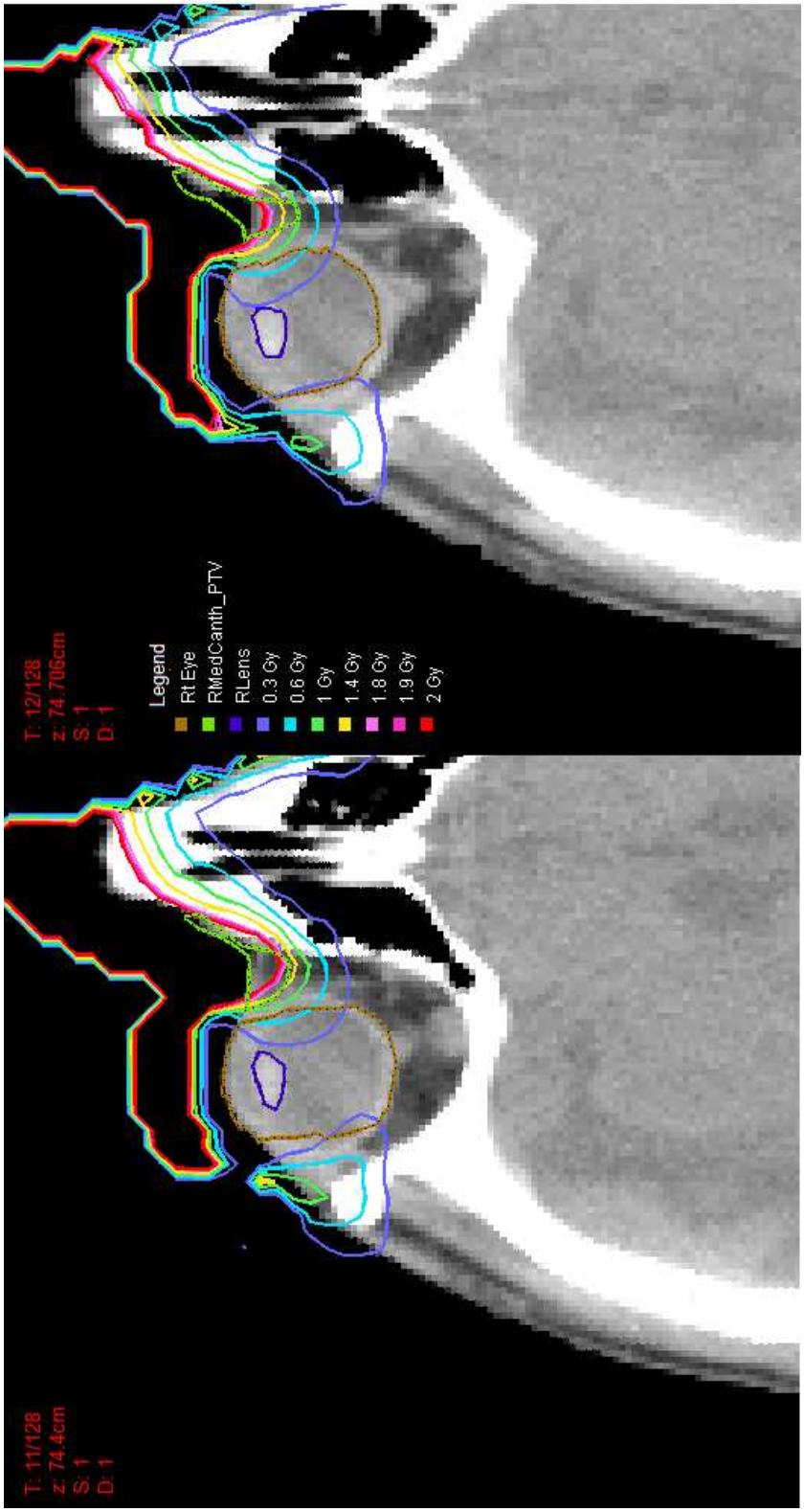
T: 12/128
z: 74.706cm
S: 1
D: 1
Legend
Rt Eye
RMedCanth_PTV
RLens
0.3 Gy
0.6 Gy
1 Gy
1.4 Gy
1.8 Gy
1.9 Gy
2 Gy
T: 11/128
z: 74.4cm
S: 1
D: 1

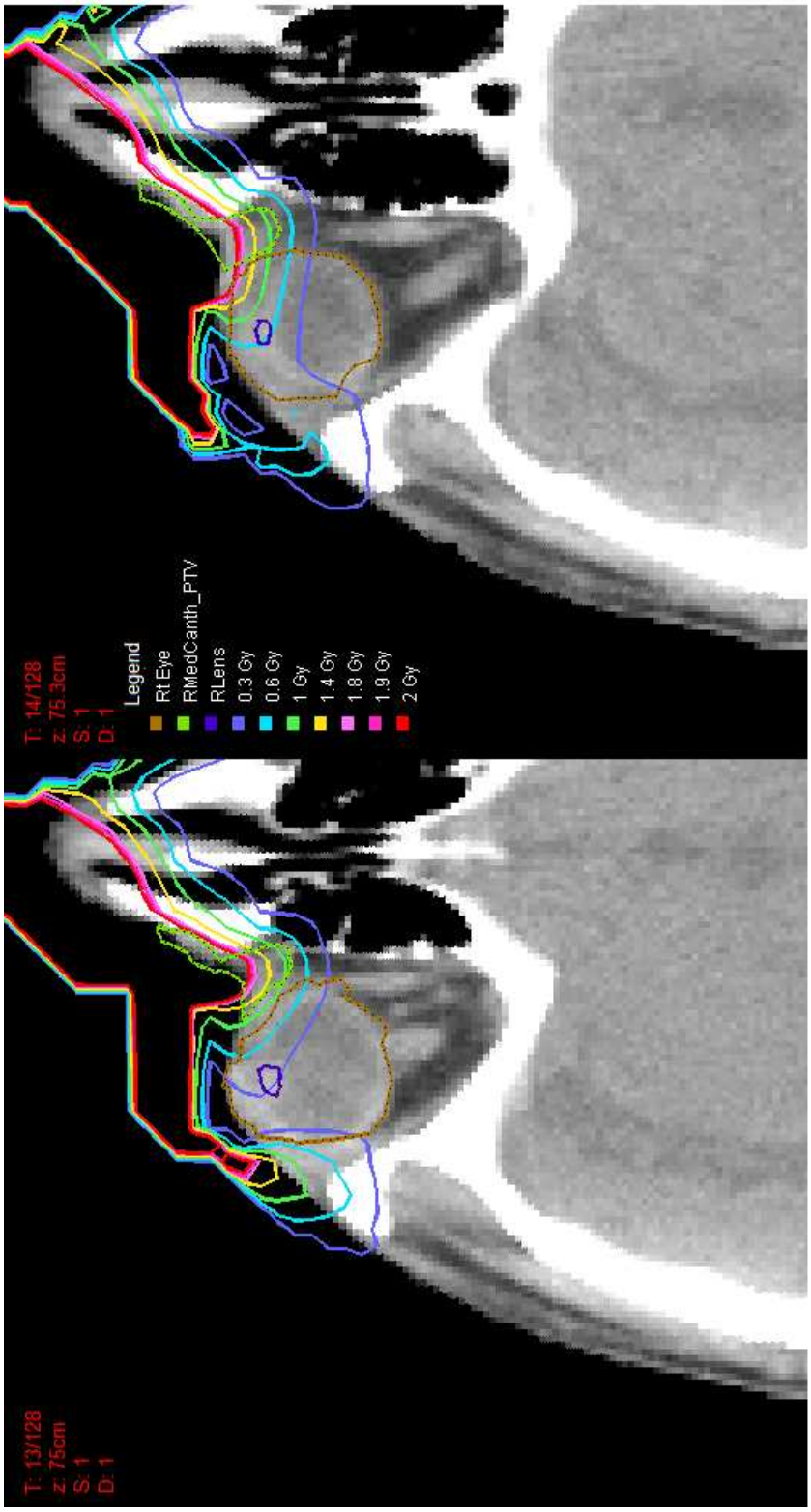

Figure 7.10: Dose distributions of 6MeV electron field on right medial canthus with tungsten eye shield inserted

The MeV electron dose distributions exhibit a number of features:

- Large penumbral boundaries - the penumbral region of the electron dose distributions is more disperse than in the photon case due to the large angles through which photons scatter as they rapidly lose energy in the first few centimeters of the phantom. This is also exacerbated by the diminishing field sizes used to cover the PTV, the smaller the field size the more the penumbral region grows due to scattering and transmission characteristics at the Cerrobend® insert defining the field.

- Smooth dose distributions - due to the predominant interaction being relatively independent of atomic number the dependence on density of the interaction is somewhat removed (this statement is qualified by the lesser perturbation of the dose distribution within bone but not by that due to tungsten). Hence the dose distribution, although attenuated by, are not predominated by the presence of bone beneath the PTV regions assessed in the current investigation.

- Effective attenuation by tungsten - tungsten is an effective attenuator of 6MeV electron fields for approximately 2.5mm thickness. The MEDTEC MT-T-45 medium sized tungsten eye shield upon which the dimensions of the current investigation are based are adequately modelled here. As the energy of the electrons increase adequate shielding is not the case and one must consider the size of the shield to be accommodated for the course of treatment under a patient's eyelid.

7.3 DVH and Point Dose Comparison

Within the current investigation the means of comparison is taken to be the DVH and point dose evaluations within the different fields. Point doses were assessed for the volume of a single voxel. Other ways by which dose distributions can be compared include such objects as normal tissue complication probabilities and tumour control probabilities.

7.3.1 Left Ear

The DVH for the PTV of the left ear without bolus in the ear canal is given in figures 7.11 and 7.12 for 100kV photons and 6MeV electron fields respectively. The total volume of the left ear PTV is 15.5 cubic cm. Dose information is given in table 7.2.

	6MeV	**100kV**
Mean dose	2.0Gy	2.1Gy
Maximum dose	2.8Gy	9.7Gy
Minimum dose	0.025Gy	0.025Gy
% volume above 2Gy	53	46

Table 7.2: Dose information for PTV DVHs in left ear treatment field with either 6MeV electrons or 100kV photons without bolus in the ear canal

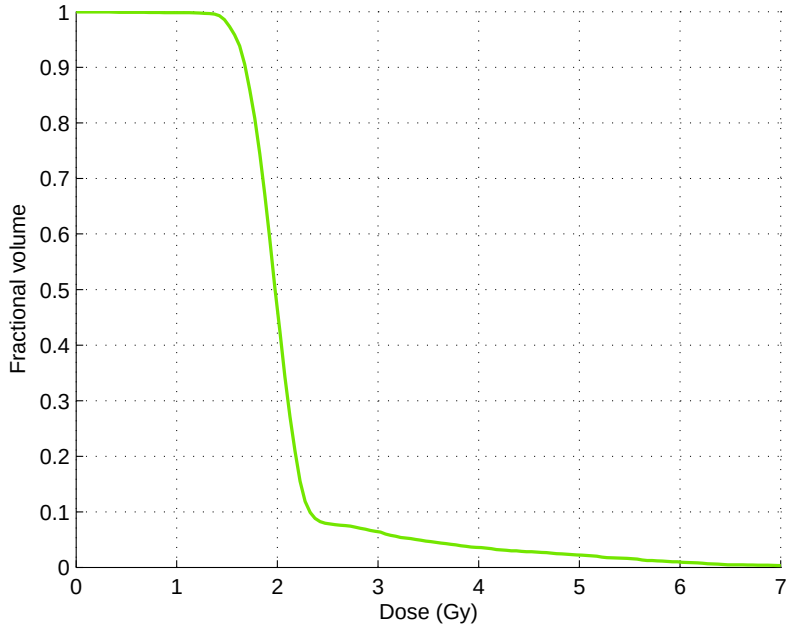

Figure 7.11: DVH comparison for the PTV in a left ear treatment field irradiated with 100kV photons without bolus in ear canal

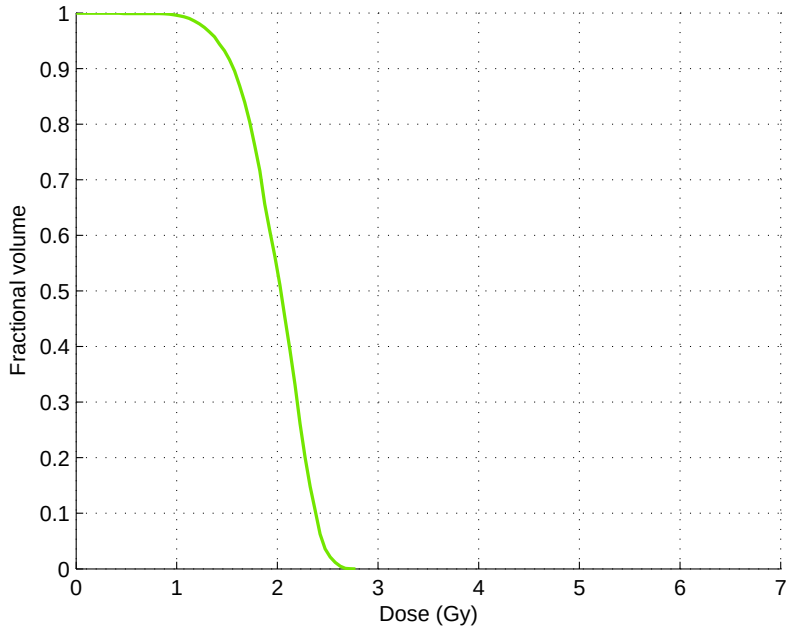

Figure 7.12: DVH comparison for the PTV in a left ear treatment field irradiated with 6MeV electrons without bolus in ear canal

The DVH for the PTV of the left ear with bolus in the ear canal is given in figures 7.13 and 7.14. Dose information for the bolus in ear canal condition is given in table 7.3.

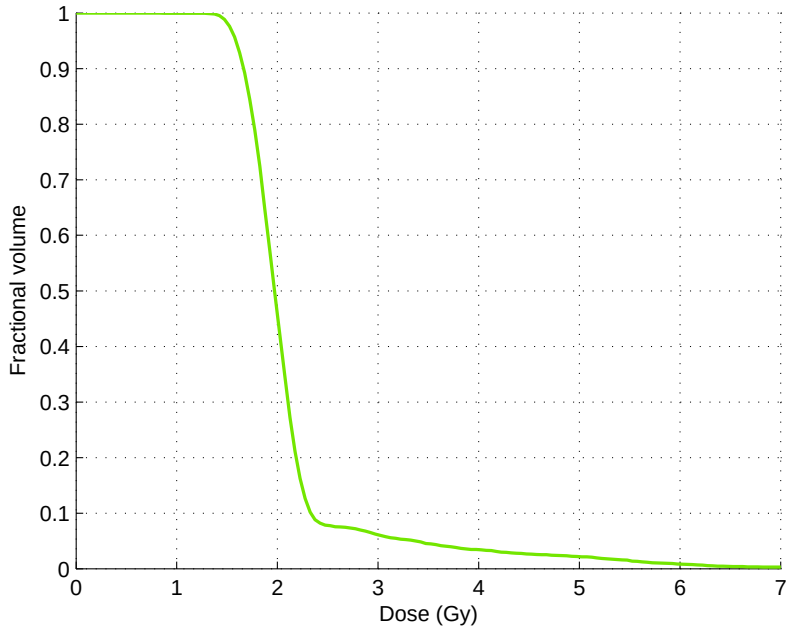

Figure 7.13: DVH comparison for the PTV in a left ear treatment field irradiated with 100kV photons with bolus in ear canal

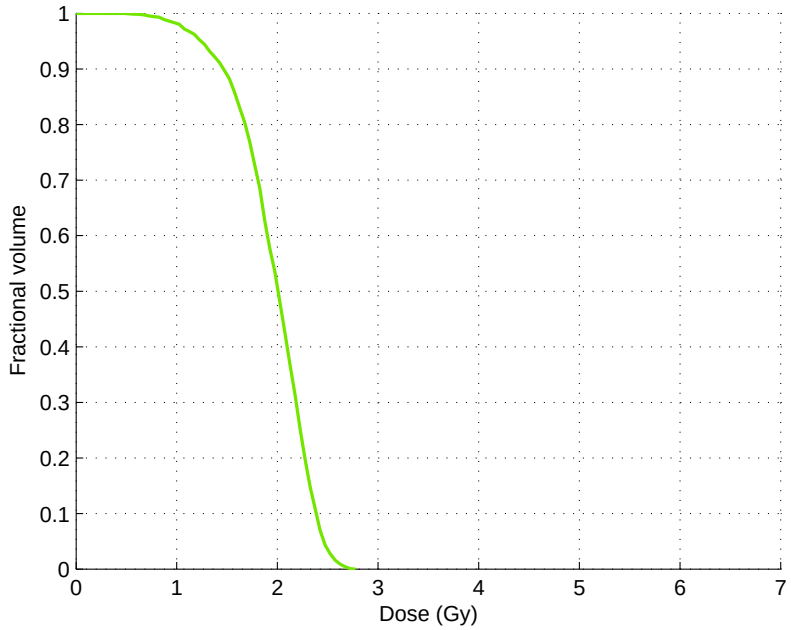

Figure 7.14: DVH comparison for the PTV in a left ear treatment field irradiated with 6MeV electrons with bolus in ear canal

	6MeV	**100kV**
Mean dose	2.0Gy	2.1Gy
Maximum dose	2.8Gy	9.8Gy
Minimum dose	0.53Gy	0.68Gy
% volume above 2Gy	51	46

Table 7.3: Dose information for DVHs in left ear treatment field with either 6MeV electrons or 100kV photons with bolus in the ear canal

As an additional comparator point doses were taken at the brain surface, at a central point within the parotid gland, within the cartilage of the ear canal, at the temporomandibular joint and within the bones of the ear. Table 7.4 details these point dose comparisons without bolus and table 7.5 details the same with bolus.

Region of Interest	**6MeV**	**100kV**
Brain Surface	0.8Gy	2Gy
Parotid Gland	0.1Gy	0.1Gy
Cartilage of the Ear Canal	1.7Gy	6Gy
Temporomandibular Joint	0.2Gy	3Gy
Bones of the Ear	0.02Gy	1Gy

Table 7.4: Point dose comparison for selected sites in left ear treatment field with either 6MeV electrons or 100kV photons without bolus in the ear canal

Region of Interest	**6MeV**	**100kV**
Brain Surface	0.8Gy	2Gy
Parotid Gland	0.1Gy	0.1Gy
Cartilage of the Ear Canal	1.7Gy	6Gy
Temporomandibular Joint	0.2Gy	3Gy
Bones of the Ear	0.01Gy	1Gy

Table 7.5: Point dose comparison for selected sites in left ear treatment field with either 6MeV electrons or 100kV photons with bolus in the ear canal

The comparison clearly shows the effect of the dominant photoelectric interaction within the 100kV photon field. This is demonstrated in the high maximum dose in the dose information tables driven by the preferential deposition of dose in high density materials within and adjacent to the photon field (such as the cartilage of the ear). The DVHs show the sharp photon penumbra influence in the steep gradient near the 2Gy normalisation dose and the long tail associated with high doses generated from high density materials in the field. In contrast the electron DVHs show the shallower gradient at near the 2Gy normalisation dose driven by the greater amount of scatter that electrons undergo as they traverse the first few centimetres of phantom.

There is no appreciable difference between the with and without bolus cases. This is demonstrated in the DVH graphs and point dose tables. The exception is the bones of the

ear in the 6MeV case that demonstrates half the point dose in the bolus case compared to the non-bolus case; although this comparison should not be considered with too much weight as the dose in the region is low and prone to high uncertainties that could be in excess of the apparent difference in doses. The major benefit from inserting bolus into the ear canal is the smoothing of the dose distribution in the PTV; both the electron and photon fields show a significant elevation in the minimum dose associated with the PTV. This investigation should not be considered definitive in this respect as it is possible to generate phantoms at a finer spatial resolution and hence model the ear canal more effectively than the current 2.5mm grid allows. Such an investigation was not undertaken here as the calculation grid associated with Varian's Eclipse treatment planning system did not allow a grid as fine as that associated with the DICOM images.

7.3.2 Left Lateral Nose

The DVH for the PTV of the left lateral nose is given in figures 7.15 and 7.16 for 80kV photons and 6MeV electrons respectively. The volume of the PTV is 4.2 cubic cm. Dose information is presented in table 7.6.

	6MeV	**80kV**
Mean dose	2.0Gy	1.7Gy
Maximum dose	2.8Gy	7.5Gy
Minimum dose	1.1Gy	0.025Gy
% volume above 2Gy	54	36

Table 7.6: Dose information for PTV DVHs in left lateral nose treatment field with either 6MeV electrons or 80kV photons

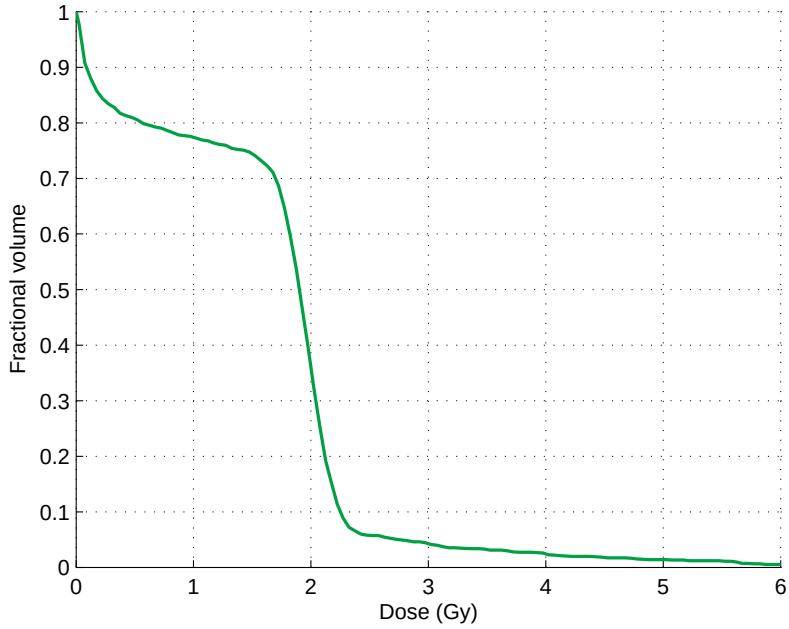

Figure 7.15: DVH comparison for the PTV in a left lateral nose treatment field irradiated with 80kV photons

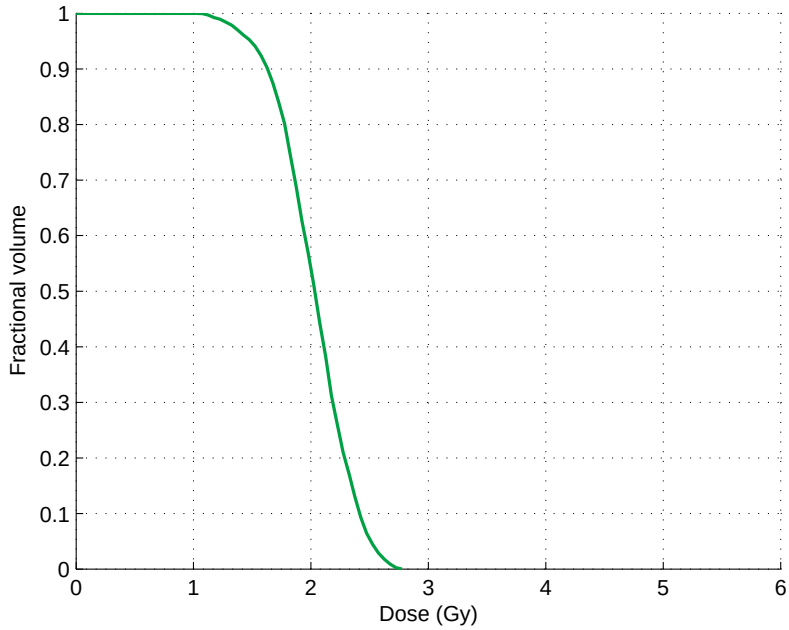

Figure 7.16: DVH comparison for the PTV in a left lateral nose treatment field irradiated with 6MeV electrons

As an additional comparator point doses were taken at the right eye lens and nasolacrimal duct. Table 7.7 details these point dose comparisons.

Region of Interest	**6MeV**	**80kV**
Nasolacrimal Duct	0.1Gy	0.2Gy
Lens of Right Eye	0.3Gy	0.13Gy

Table 7.7: Point dose comparison for selected sites in left lateral nose treatment field with either 6MeV electrons or 80kV photons

There are a number of factors that generate the differences seen between the electron and photon fields in this case. The physical size of the applicator is one such factor for the photon field and this is clearly seen in the DVH where a portion of the PTV is poorly covered by the 80kV photon field. The ability to optimise the treatment plan in the Monte Carlo simulation is poor as the visualisation tools thus far developed are memory intensive and several orders of magnitude slower than the similar tools on commercial treatment planning systems. Therefore, optimal angles and stand off distance determinations to generate the optimum dose distribution require several days to accomplish. In this instance if the 80kV field shows more favourable characteristics in the penumbral region marked by the steep gradient at the 2Gy mark on the DVH. Additionally the presence of cartilage and bone directly beneath the PTV increases the dose in certain areas of the PTV for the photon field up to 7.5Gy. The 6MeV electron field, due to the predominance of interactions independent of atomic number of the incident and secondary particles, shows a much smoother dose distribution.

The lens of the right eye is irradiated more in the electron case due to some of the electron field passing past the tip of the nose and and scattering in the bolus there and into the right lens area. This could be mitigated somewhat by the addition of an eye shield.

7.3.3 Right Medial Canthus

The DVHs for the PTV, right lens and right eye of the right medial canthus treatment field are given in figures 7.17 and 7.18 for 100kV photons and 6MeV electrons respectively. Dose information for the sites of interest is presented in table 7.8. The volumes associated with the structures of interest are: 2.5 cubic cm for the PTV, 0.35 cubic cm for the right lens and 11 cubic cm for the right eye.

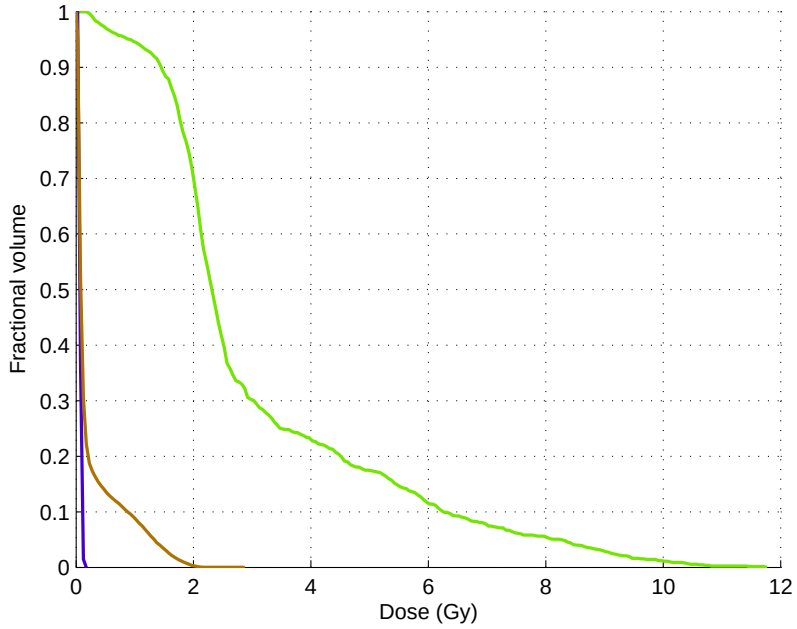

Figure 7.17: DVH comparison for the PTV, right lens and right eye in a right medial canthus treatment field irradiated with 100kV photons (PTV in green, right lens in blue and right eye in brown)

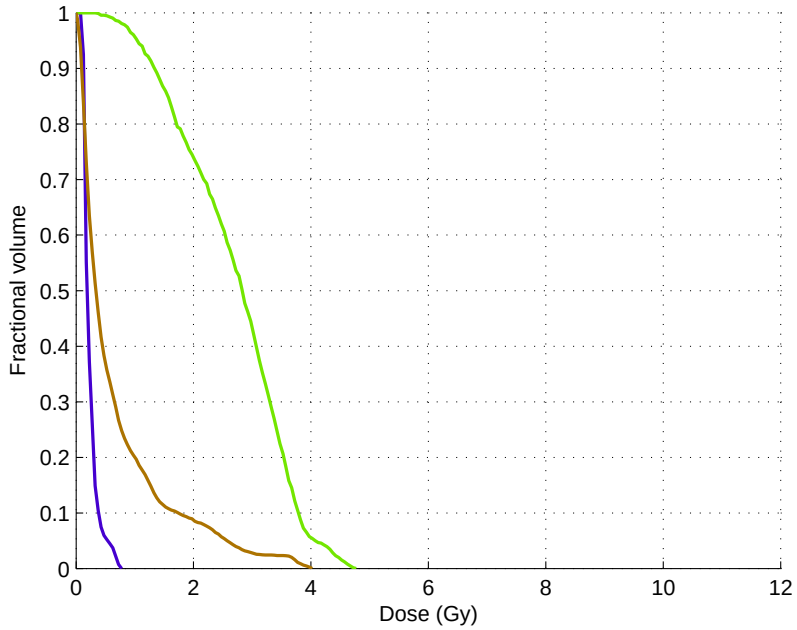

Figure 7.18: DVH comparison for the PTV, right lens and right eye in a right medial canthus treatment field irradiated with 6MeV electrons (PTV in green, right lens in blue and right eye in brown)

	6MeV	**100kV**
	PTV	
Mean dose	2.7Gy	3.1Gy
Maximum dose	4.8Gy	12Gy
Minimum dose	0.38Gy	0.23Gy
% volume above 2Gy	73	70
	Right Lens	
Mean dose	0.26Gy	0.094Gy
Maximum dose	0.78Gy	0.18Gy
Minimum dose	0.13Gy	0.075Gy
	Right Eye	
Mean dose	0.68Gy	0.27Gy
Maximum dose	4.0Gy	2.9Gy
Minimum dose	0.025Gy	0.025Gy

Table 7.8: Dose information for PTV, right lens and right eye DVHs in right medial canthus treatment field with either 6MeV electrons or 100kV photons

As an additional comparator point doses were taken for the nasolacrimal duct. Table 7.9 details this point dose comparisons.

Region of Interest	**6MeV**	**100kV**
Nasolacrimal Duct	2.2Gy	1.9Gy

Table 7.9: Point dose comparison for selected sites in right medial canthus treatment field with either 6MeV electrons or 100kV photons

This is an extremely problematic treatment field to simulate due to the induration exhibited by the PTV. The PTV is shielded somewhat by the overlying eye shield that is inserted into the treatment field to protect the lens of the eye. The 6MeV electron field can cope with this to a degree due to the natural propensity of the electrons to scatter laterally after only a short distance into the phantom. This generates the elevated dose that is seen in the right eye of the 6MeV electron field. The photon field has to be angled more towards the eye to cope with this induration.

The hot spots in the 80kV photon field are driven by the predominantly photoelectric interaction of the photons. Skin overlying cartilage and bone has been protected somewhat by the addition of lead on to the surface of the phantom. The addition of bolus in the 6MeV electron field removes the effect of the slight build up region in the electron field.

Chapter 8

Conclusion

The dose distributions derived in the investigation into the treatment of superficial cancers of the head and neck present some interesting features. Firstly that there are a number of properties of the accelerator outputs at surface that are not in full agreement with the measurements derived from the PTW MP3 water phantom. These have been explained by the limitations associated with the measurement apparatus. As the investigation was primarily concerned with superficial cancers the regions of interest, *e.g.* the PTVs, have portions of their dose distributions present in this surface discrepancy region, especially those associated with the photons due to the lack of bolus in the treatment field. The agreement obtained for the electron accelerators was within reason though not optimised as much as it could of been due to the desire not to perfectly emulate the clinical treatment unit but to show proof of concept and hence move on to determination of dose distributions. However, the greatest discrepancy was derived for the superficial unit simulation with up to 20% difference at the surface for the 5cm diameter applicator. This is provided that the normalisation point is taken at depth (specifically this was taken to be 20mm depth in the current investigation). If the normalisation had been taken at surface this discrepancy would have presented itself more markedly at depth through the steep gradient region. However, such a normalisation would not be entirely trustworthy due to the limitations of the measurement devices at surface. A more definitive study of surface dosimetry is required for the superficial units before any quantitative conclusion can be drawn.

In keeping with the initial accelerator simulations the matching of the isodose data highlights the limitations of the use of interpolation and extrapolation on the sparse data sets that are typical of the water phantom measurements. Even though a good quantitative comparison can be made from depth dose and profile curves alone the expansion of the measured data set to compare to the Monte Carlo simulations shows large deviations in the penumbral regions away from the measured depth dose and profile curves. Refining the method of interpolation and extrapolation would be an obvious solution to this however the physics of the interactions changes markedly from the superficial unit to the electron accelerator and any method would need to take this into account and hence be entirely subjective. The only solution to this problem would be to take as complete a measurement set as the Monte Carlo simulation, *i.e.* 2mm voxel across the length and depth of simulation. Such a task would require a large amount of water phantom time and still be subject to the limiting characteristics of the measurement devices at the surface.

The means by which the phantoms are edited to insert high atomic number materials and the subsequent display of this information in the DICOM RT driven applications requires further refinement. At present there appears a ghosting in the dose distribution information where bolus, tungsten and lead was simulated but the original DICOM image does not contain the updated electron density information. Additionally the means by which the editing is effected is rudimentary and could be speed up considerably by

devoting more time to coding an efficient and user friendly interface to do so.

The superficial cancer treatment field dose distributions display a lot of information regarding the three sites considered in the current investigation. For the MeV electron fields the structure seen in the dose distribution does not depart considerably from that currently seen on the commercial treatment planning systems, except in the instance of tungsten eye shields. However this structure is qualitatively similar to investigations of tungsten eye shields reported in the literature [38]. The quantitative analysis drawn from these dose distributions is limited to the 2mm×2mm×3mm voxel sizes used in the simulations. This spatial resolution can be finer at the expense of simulation time and requires more computational power than was available for the current investigation but is possible. The features of the dose distributions were still sufficient to demonstrate the coverage achievable by MeV electrons in the treatment of superficial cancers. The diffuse nature of electrons was demonstrated in the gradient as the dose in the DVHs approached the 2Gy normalisation point and the short practical range of the fields was demonstrated in the low maximum doses associated with the PTVs. The major finding in the current investigation was the quantitative measure of scatter underneath an eye shield with the DVH analysis of the right medial canthus showing elevated mean, maximum and minimum doses for both lens and eye in the field in comparison to the photon field applied to the same region.

For kV photons the pattern of dose distributions for the treatment sites demonstrates the sharp penumbra and greater penetration expected of photon fields. This is demonstrated in the steep gradients in the DVHs as the dose approached the 2Gy normalisation point and the much deeper isodose lines within the phantoms. The sharp penumbra is also demonstrated in the eye shielded right medial canthus field where, in comparison to the MeV electron field, very little radiation is scattered into either the lens or the eye. However, the major finding of the investigation is the high level of dose deposition along the higher density interfaces inside the phantoms, *i.e.* tissue to cartilage or tissue to bone. In these instances up to 12Gy was seen in the point doses. This was typical of very thin skin layers overlying bone on the nasal portion of the right medial canthus field. These point doses are relative to the normalisation point of 2Gy within the body of the PTV.

Normalisation of the dose distributions was undertaken in as even a gradient region as possible within the PTVs associated with each site. This was of the order of 1cm deep for the photon fields and 2cm deep for the electron fields. This is past the surface region where the demonstrated discrepancies in depth dose curves lie but still required careful consideration due to the obvious gradient through the PTV. The task of normalisation and comparison is complicated in this respect due to the difficulties in optimising the treatment field. The CPU intensive calculation of dose distributions via the Monte Carlo method means that the number of times one can calculate different field set ups within a certain level of confidence is dependent on the amount of time available to generate a plan. In a clinical setting it is not an option to spend a week optimising angles, stand off distances and field shape. As demonstrated in the left lateral ear treatment the PTV can have quite different structure if adjacent air gaps are filled with bolus. This requires efficient modelling of the air gaps in a treatment plan which is complicated by the presence of partial volume artifacts. Such artifacts are driven not only by the limitations of CT technology but also in generating the much coarser spatial resolution `egsphant` files used in the Monte Carlo simulations. Hence, even though the Monte Carlo method is a powerful general purpose calculation tool the underlying optimisation is still subjective.

The means of comparison that was presented in this thesis is not limited to reporting the maximum, minimum, mean and point doses. It is not a trivial task to code other comparators into an application such as CERR running in the MATLAB® environment and hence was not undertaken here. Similarly the maximum and minimum doses are derived for the voxel size used in the simulation and if the uncertainty associated with a pixel is high (as is likely in the surface regions where a thin layer of skin overlies bone in the superficial fields generating the largest point doses) the severity of the dose can be put into context. Increasing the size of the region used to calculate maximum and minimum doses would yield more pertinent information about the treatment field.

This thesis has presented the findings of the investigation into the Monte Carlo simulation of superficial cancer treatments of the head and neck region. It has shown that it is possible to simulate kV X-ray units, highlighting issues with surface dosimetry. It has also shown that quantitative dose distributions can be determined for both MeV electron and kV photon fields with high atomic number materials, rapidly sloping surfaces and different density interfaces, highlighting the relatively high level of dose deposition of dose in tissue-bone and tissue-cartilage interfaces in the kV photon fields. From these dose distributions DVH and dose comparators have been used to assess the simulated treatment fields, highlighting the extent to which further development of software tools in the optimisation of Monte Carlo simulations in radiotherapy is required.

8.1 Acknowledgements

As with any project of this magnitude there are plenty of people to acknowledge and thank wholeheartedly. Of course there are my employers Capital and Coast District Health Board in association with the Australasian College of Physical Scientists and Engineers in Medicine whom have embraced the training of medical physicists and allowed me to write this thesis. Lynne Greig and Anthony Johnson of the Wellington Blood and Cancer Centre deserve special thanks for being my clinical supervisors for this work and have provided support and constructive criticism when needed. Associate Professor Lou Reinisch of the Physics and Astronomy Department, University of Canterbury is the academic supervisor of this project and, for such an ordinary thesis student, he has put up with me extraordinarily well; he has also been a source of great wisdom for me and my association with him has seemed to be a bit of a one way street of me taking and taking, I just hope one day to be able to repay the debt. My colleagues at the Wellington Blood and Cancer Centre have also been very supportive during this venture with special thanks to Ekta Jhala for her positivism and listening to my tangential Friday rants and Tony Venning for his invaluable MATLAB® technical support. Iwan Kawrakow, Blake Walters and Ernesto Mainegra-Hing of the National Research Council of Canada in association with Carleton University's Dave Rogers are owed a special thanks for running two courses which I was fortunate enough to attend in using the EGSnrc and BEAMnrc applications. Last, but by no means least, Deloar Hossain of the Physics and Biomedical Engineering Department of Christchurch Hospital is to be thanked for the help that he gave me on several occasions when I travelled down to Christchurch and set up office next to him to undertake the Monte Carlo simulation comparisons.

Thank you all so much, it is a humbling experience to have so much input into my professional development from so many enthusiastic and intelligent people

Appendix A

Input Files for BEAMnrc Simulations

The following are the input files used in the Pantak Therapax SXT 150 simulations contained within this thesis. For a fuller explanation of the format and parameter definition of the following files see [21].

A.1 Open Geometry 100kV

```
%SXR unit - 100kV beam with open field #!GUI1.0
AIR521ICRU
0, 0, 0, 0, 0, 2, 0, IWATCH ETC. 1000000000, 33, 97, 999, 1, 1000, 0, 0, NCASE
ETC.
-1, 10, 0.375, -1, 0, 0, 0.0, 0.0, 0.0, 0.0, IQIN, ISOURCE + OPTIONS
0, MONOENERGETIC
0.1
0, 0, 0.51, 0.001, 0, 0, , 0 , ECUT,PCUT,IREJCT,ESAVE
0, 0, 0, 0, 0, PHOTON FORCING
1, 3, SCORING INPUT
1, 0
5,
0, DOSE COMPONENTS
0.0, Z TO FRONT FACE
********** start of CM XTUBE with identifier MXR_161 ***********
5, RMAX
X-ray tube
0, 3.7, ZMIN, ZTHICK
30, ANGLE
2, # LAYERS
5
0, 0, 0, 0,
CU521ICRU
0.2
0, 0, 0, 0,
W521ICRU
0, 0, 0, 0,
VACUUM
0, 0, 0, 0,
CU521ICRU
********** start of CM SLABS with identifier BeWin ***********
5, RMAX
```

```
Be exit window
2, NSLABS
3.7, ZMIN
1.65, 0, 0, 0, 0, 0
VACUUM
0.08, 0, 0, 0, 0, 0
BE521ICRU
********** start of CM CONESTAK with identifier Filter ***********
5, RMAX
Filter
5.43, 4.9999, ZMIN, RBN
5, NUMBER OF LAYERS
1.5, 1.76, 1.76,
0.2, 1.9, 1.9,
0.01, 1.9, 1.9,
0.18, 1.9, 1.9,
0.21, 1.9, 1.9,
0, 0, 0, 0, OUTER WALL
STEEL521ICRU
0, 0, 0, 0,
AIR521ICRU
0, 0, 0, 0,
STEEL521ICRU
0, 0, 0, 0,
AIR521ICRU
0, 0, 0, 0,
STEEL521ICRU
0, 0, 0, 0,
CU521ICRU
0, 0, 0, 0,
STEEL521ICRU
0, 0, 0, 0,
AL521ICRU
0, 0, 0, 0,
STEEL521ICRU
0.51, 0.001, , ,
AIR521ICRU
0.51, 0.001, , ,
STEEL521ICRU
**********end of all CMs**********
#########################
:Start MC Transport Parameter:
Global ECUT= 0.51
Global PCUT= 0.001
Global SMAX= 5
ESTEPE= 0.25
XIMAX= 0.5
```

```
Boundary crossing algorithm= PRESTA-I
Skin depth for BCA= 0
Electron-step algorithm= PRESTA-II
Spin effects= On
Brems angular sampling= Simple
Brems cross sections= BH
Bound Compton scattering= On
Pair angular sampling= Simple
Photoelectron angular sampling= On
Rayleigh scattering= Off
Atomic relaxations= On
Electron impact ionization= On
:Stop MC Transport Parameter:
##########################
```

A.2 Open Geometry 80kV

```
%SXR unit - 80kV beam with open field #!GUI1.0
AIR521ICRU
0, 0, 0, 0, 0, 2, 0, IWATCH ETC. 1000000000, 33, 97, 999, 1, 1000, 0, 0, NCASE
ETC.
-1, 10, 0.375, -1, 0, 0, 0.0, 0.0, 0.0, 0.0, IQIN, ISOURCE + OPTIONS
0, MONOENERGETIC
0.08
0, 0, 0.51, 0.001, 0, 0, , 0 , ECUT,PCUT,IREJCT,ESAVE
0, 0, 0, 0, 0, PHOTON FORCING
1, 3, SCORING INPUT
1, 0
5,
0, DOSE COMPONENTS
0.0, Z TO FRONT FACE
********** start of CM XTUBE with identifier MXR_161 ***********
5, RMAX
X-ray tube
0, 3.7, ZMIN, ZTHICK
30, ANGLE
2, # LAYERS
5
0, 0, 0, 0,
CU521ICRU
0.2
0, 0, 0, 0,
W521ICRU
0, 0, 0, 0,
VACUUM
0, 0, 0, 0,
```

```
CU521ICRU
********** start of CM SLABS with identifier BeWin ***********
5, RMAX
Be exit window
2, NSLABS
3.7, ZMIN
1.65, 0, 0, 0, 0, 0
VACUUM
0.08, 0, 0, 0, 0, 0
BE521ICRU
********** start of CM CONESTAK with identifier Filter ***********
5, RMAX
Filter
5.43, 4.9999, ZMIN, RBN
5, NUMBER OF LAYERS
1.5, 1.76, 1.76,
0.2, 1.9, 1.9,
0.01, 1.9, 1.9,
0.18, 1.9, 1.9,
0.21, 1.9, 1.9,
0, 0, 0, 0, OUTER WALL
STEEL521ICRU
0, 0, 0, 0,
AIR521ICRU
0, 0, 0, 0,
STEEL521ICRU
0, 0, 0, 0,
AIR521ICRU
0, 0, 0, 0,
STEEL521ICRU
0, 0, 0, 0,
CU521ICRU
0, 0, 0, 0,
STEEL521ICRU
0, 0, 0, 0,
AL521ICRU
0, 0, 0, 0,
STEEL521ICRU
0.51, 0.001, , ,
AIR521ICRU
0.51, 0.001, , ,
STEEL521ICRU
**********end of all CMs**********
#########################
:Start MC Transport Parameter:
Global ECUT= 0.51
Global PCUT= 0.001
```

```
Global SMAX= 5
ESTEPE= 0.25
XIMAX= 0.5
Boundary crossing algorithm= PRESTA-I
Skin depth for BCA= 0
Electron-step algorithm= PRESTA-II
Spin effects= On
Brems angular sampling= Simple
Brems cross sections= BH
Bound Compton scattering= On
Pair angular sampling= Simple
Photoelectron angular sampling= On
Rayleigh scattering= Off
Atomic relaxations= On
Electron impact ionization= On
:Stop MC Transport Parameter:
##########################
```

Appendix B

MATLAB® Routines

The removal of partial volume artifacts near the surface of phantoms derived from CT data and insertion of bolus, lead and high atomic number shielding materials required the writing of a MATLAB® routine to edit the `egsphant` files. This process is very CPU and memory intensive especially as the `egsphant` files become large due to increased spatial resolution or calculation volume. To mitigate this would require much more software development work, however the routine detailed here was sufficient for the research undertaken.

```
%Utility to read egsphant ascii file and allow user
%to edit the media type and density
%
%Written by Bryn Currie July 2006

clear all
clc
close all
imview close all

%User input required by program
fprintf('\nInput the name of the file to be divided into material and\n')
fprintf('density matrices\n')
egsfile = input('Filename including extension:  ','s');

%Open the specified file
fphant = fopen(egsfile,'r');

%Output media information
media = textscan(fphant,'%n',1);
n_media = media{1};

fprintf('\nNumber of materials in the phantom = %d',n_media)
dlmwrite('edited.egsphant',n_media)

material = cell(n_media,1);
fedtegs=fopen('edited.egsphant','a');

for nm = 1:n_media
   material(nm,1) = textscan(fphant,'%s',1);
   mat = material{nm,1};
```

```
   fprintf('\nMaterial %d is %s',nm,mat{:});
   fprintf(fedtegs,'%s\n',mat{:});
end

fclose(fedtegs);

%Skip dummy input line but write into edited.egsphant file
% ignore_dummy=cell(n_media,1);

for dummy = 1:n_media
   ignore_dummy = textscan(fphant,'%n',1);
end

ignore = ones(1,n_media);
dlmwrite('edited.egsphant',ignore,'-append','delimiter',' ')

%Output voxel information
x_index = textscan(fphant,'%n',1);
x = x_index{:};
y_index = textscan(fphant,'%n',1);
y = y_index{:};
z_index = textscan(fphant,'%n',1);
z = z_index{:};

fprintf('\n\nThe voxel numbers in the data set are:\n x = %d\n y = %d\n z =
%d\n',x,y,z)

fedtegs=fopen('edited.egsphant','a');
fprintf(fedtegs,'%g %g %g\n',x,y,z);

%Skip voxel boundaries but calculate the length of the x, y and z axes
Xboundary = cell(1,x+1);
Yboundary = cell(1,y+1);
Zboundary = cell(1,z+1);

for Xignore_boundary = 1:x+1
   Xboundary(1,Xignore_boundary) = textscan(fphant,'%n',1);
   fprintf(fedtegs,'%g%',Xboundary{1,Xignore_boundary});
   fprintf(fedtegs,' ');
end

fprintf(fedtegs,'\n');

for Yignore_boundary = 1:y+1
   Yboundary(1,Yignore_boundary) = textscan(fphant,'%n',1);
   fprintf(fedtegs,'%g%',Yboundary{1,Yignore_boundary});
   fprintf(fedtegs,' ');
```

```
end

fprintf(fedtegs,'\n');

for Zignore_boundary = 1:z+1
   Zboundary(1,Zignore_boundary) = textscan(fphant,'%n',1);
   fprintf(fedtegs,'%g% ',Zboundary{1,Zignore_boundary});
   fprintf(fedtegs,' ');
end

fprintf(fedtegs,'\n'); fclose(fedtegs);

if (Xboundary{1,1}<0) & (Xboundary{1,x+1}>0)
   Xlen = Xboundary{1,x+1} - Xboundary{1,1};
elseif (Xboundary{1,1}<0) & (Xboundary{1,x+1}<0)
   Xlen = abs(Xboundary{1,x+1} - Xboundary{1,1});
else
   Xlen = abs(Xboundary{1,x+1} - Xboundary{1,1});
end

if (Yboundary{1,1}<0) & (Yboundary{1,y+1}>0)
   Ylen = Yboundary{1,y+1} - Yboundary{1,1};
elseif (Yboundary{1,1}<0) & (Yboundary{1,y+1}<0)
   Ylen = abs(Yboundary{1,y+1} - Yboundary{1,1});
else
   Ylen = abs(Yboundary{1,y+1} - Yboundary{1,1});
end

if (Zboundary{1,1}<0) & (Zboundary{1,z+1}>0)
   Zlen = Zboundary{1,z+1} - Zboundary{1,1};
elseif (Zboundary{1,1}<0) & (Zboundary{1,z+1}<0)
   Zlen = abs(Zboundary{1,z+1} - Zboundary{1,1});
else
   Zlen = abs(Zboundary{1,z+1} - Zboundary{1,1});
end

fprintf('\nThe phantom is %d cm wide, %d cm high and %d cm
deep\n',Xlen,Ylen,Zlen)

%The material and density information is now in matrix format,
%the next thing to do is load the DICOM images from the slice that the
%user wants to edit.  This is done by using the ctcreate slice list
%file that is used in the original generation of the .egsphant
%file.

%User input required by program
fprintf('\nInput the name of the file containing dicom images with
```

```
directory\n') fprintf('information stripped off\n')
slicefile = input('Filename including extension (if any):  ','s');

%Open the specified file
fslice = fopen(slicefile,'r');

%Output image information
slice = cell(z,1);

for ns = 1:z
   slice(ns,1) = textscan(fslice,'%s',1);
   n_slice = slice{ns,1};
   fprintf('\nSlice %d file is %s',ns,n_slice{:})
end

fclose(fslice);

%The users is now prompted to enter the slice that they wish to
%edit and a dicom viewer opens the appropriate file

%User input required by program
editslice = input('\n\nInput the number of the slice you wish to edit:  ');

fprintf('\nLocate the mouse over the area that you wish to edit
and enter the') fprintf('\nX and Y pixel values below\n')

dicomY = input('\nX: '); dicomX = input('\nY: ');

% Now we wish to open the corresponding matrix of .egsphant density and
% material types around this dicom image location.  These two matrices are
to
% be edited and then written back into the .egsphant file and then the
% density matrix corresponding to the edited slice read in and displayed
% as an image.

% This is a rather limited program in that the pixel that the user selects
% assumes that the user is wanting to edit the image close to the centre of
% a 512x512 matrix and that the region of interest is small.

%Find the pixel location
Xpixel_loc = Xlen*(dicomX/512); Ypixel_loc = Ylen*(dicomY/512);

%Find the corresponding location in the .egsphant file

   %Pixel size in .egsphant
   Xphantpix_size = Xlen/x;
   Yphantpix_size = Ylen/y;
```

```
Xphantpix = ceil(Xpixel_loc/Xphantpix_size);
Yphantpix = ceil(Ypixel_loc/Yphantpix_size);

%Prompt user to select the region of interest size in numbers of pixels in
%X and Y directions

fprintf('\nThe following ROI pixel values MUST BE ODD to centre the ROI\n')
Yroi = input('\nInput the x-pixel extent of the ROI to be edited in the
.egsphant file:  ');
Xroi = input('\nInput the y-pixel extent of the ROI to be edited in the
.egsphant file:  ');

%Read/write media matrix for editing into a slice specific cell
%and write the remaining unnecessary elements into the edited.egsphant
%file

fedtegs=fopen('edited.egsphant','a'); mat_matrix = cell(x,y);

%Pre-slice writing
for zpreslice = 1:(editslice-1)
   for fpx = 1:x
      for fpy = 1:y
         mat_element = textscan(fphant,'%1n',1);
         fprintf(fedtegs,'%g',mat_element{:});
      end
      fprintf(fedtegs,'\n');
   end
   fprintf(fedtegs,'\n');
end

%Slice loaded into memory
for xlim = 1:x
   for ylim = 1:y
      mat_matrix(xlim,ylim) = textscan(fphant,'%1n',1);
   end
end

%Display the current material matrix in a colour plot indicating
%material types
mat_display = zeros(x,y); for mdi = 1:x
   for mdj = 1:y
      mat_display(mdi,mdj)=mat_matrix{mdi,mdj};
   end
end

subplot(2,2,1),subimage(mat_display,jet(8))
```

```
%Display the material type component of the .egsphant file in the region of
%interest

mat_displayROI = zeros(Xroi,Yroi);
for mdxroi = 1:Xroi
   for mdyroi = 1:Yroi
      mat_displayROI(mdxroi,mdyroi)=...
      mat_matrix{(mdxroi-1+(Xphantpix-((Xroi-1)/2))),...
      (mdyroi-1+(Yphantpix-((Yroi-1)/2)))};
   end
end

fprintf('\nThe region of interest values for the material matrix
is as follows:\n')
mat_displayROI

%Prompt user to enter new values for region of interest

mat_ROI_edit = mat_displayROI;
fprintf('\nEnter the new values for the corresponding position in the
material\n')
fprintf('and density matrices.\n')
fprintf('\nNEW MATERIAL VALUES at x,y in mat_displayROI\n')
mat_displayROI
for matedx = 1:Xroi
   for matedy = 1:Yroi
      fprintf('\nMatrix element %d, %d:',matedx,matedy)
      mat_ROI_edit(matedx,matedy)=input('\nMATERIAL = ')
   end
end

%Write edited subspaces back into original matrix data

mat_matrix_edt = zeros(x,y);

limx = (Xphantpix-((Xroi-1)/2)); limy = (Yphantpix-((Yroi-1)/2));

for mmex=1:x
   for mmey=1:y
      mat_matrix_edt(mmex,mmey)=mat_matrix{mmex,mmey};
   end
end

for owritex = limx:limx+Xroi-1
   for owritey = limy:limy+Yroi-1
      mat_matrix_edt(owritex,owritey)=...
```

```
      mat_ROI_edit(owritex-limx+1,owritey-limy+1);
   end
end

%Write edited matrix into edited.egsphant
for fpx = 1:x
   for fpy = 1:y
      fprintf(fedtegs,'%g',mat_matrix_edt(fpx,fpy));
   end
   fprintf(fedtegs,'\n');
end
fprintf(fedtegs,'\n');

%Post-slice writing
for zpostslice = 1:(z-editslice)
   for fpx = 1:x
      for fpy = 1:y
         mat_element = textscan(fphant,'%1n',1);
         fprintf(fedtegs,'%g',mat_element{:});
      end
      fprintf(fedtegs,'\n');
   end
   fprintf(fedtegs,'\n');
end

subplot(2,2,3),subimage(mat_matrix_edt,jet(8))

%Read write density matrix for editing into a slice specific cell
%and write the remaining unnecessary elements into the edited.egsphant
%file

dens_matrix = cell(x,y);

%Pre-slice writing
for zpreslice = 1:(editslice-1)
   for fpx = 1:x
      for fpy = 1:y
         dens_element = textscan(fphant,'%n',1);
         fprintf(fedtegs,' %g',dens_element{:});
      end
      fprintf(fedtegs,'\n');
   end
   fprintf(fedtegs,'\n');
end

%Slice loaded into memory
for xlim = 1:x
```

```
   for ylim = 1:y
      dens_matrix(xlim,ylim) = textscan(fphant,'%n',1);
   end
end

%Display the current density matrix
dens_display = zeros(x,y); for mdi = 1:x
   for mdj = 1:y
      dens_display(mdi,mdj)=dens_matrix{mdi,mdj};
   end
end

subplot(2,2,2),subimage(dens_display,[0,2])

%Display the density component of the .egsphant file in the region of
%interest

dens_displayROI = zeros(Xroi,Yroi);
for ddxroi = 1:Xroi
   for ddyroi = 1:Yroi
      dens_displayROI(ddxroi,ddyroi)=...
      dens_matrix{(ddxroi-1+(Xphantpix-((Xroi-1)/2))),...
      (ddyroi-1+(Yphantpix-((Yroi-1)/2)))};
   end
end

fprintf('\nThe region of interest values for the density matrix
is as follows:\n')
dens_displayROI

%Prompt user to enter new values for region of interest

dens_ROI_edit = dens_displayROI;
fprintf('\nNEW DENSITY VALUES at x,y in mat_displayROI\n')
dens_displayROI
for denedx = 1:Xroi
   for denedy = 1:Yroi
      fprintf('\nMatrix element %d, %d:',denedx,denedy)
      dens_ROI_edit(denedx,denedy)=input('\nDENSITY = ')
   end
end

%Write edited subspaces back into original matrix data

dens_matrix_edt = zeros(x,y);

limx = (Xphantpix-((Xroi-1)/2));
```

```
limy =(Yphantpix-((Yroi-1)/2));

for dmex=1:x
   for dmey=1:y
      dens_matrix_edt(dmex,dmey)=dens_matrix{dmex,dmey};
   end
end

for dens_owritex = limx:limx+Xroi-1
   for dens_owritey = limy:limy+Yroi-1
      dens_matrix_edt(dens_owritex,dens_owritey)=...
      dens_ROI_edit(dens_owritex-limx+1,dens_owritey-limy+1);
   end
end

%Write edited matrix into edited.egsphant
for fpx = 1:x
   for fpy = 1:y
      fprintf(fedtegs,' %g',dens_matrix_edt(fpx,fpy));
   end
   fprintf(fedtegs,'\n');
end
fprintf(fedtegs,'\n');

%Post-slice writing
for zpostslice = 1:(z-editslice)
   for fpx = 1:x
      for fpy = 1:y
         dens_element = textscan(fphant,'%n',1);
         fprintf(fedtegs,' %g',dens_element{:});
      end
      fprintf(fedtegs,'\n');
   end
   fprintf(fedtegs,'\n');
end

subplot(2,2,4),subimage(dens_matrix_edt,[0,2])

fclose(fedtegs); fclose(fphant);

%End of the program
```

References

[1] D Giffiths. *Introduction to Elementary Particle Physics*. John Wiley & Sons, 1987.

[2] H E Johns and J R Cunningham. *The Physics of Radiology*. Charles C Thomas, 4$^{\text{th}}$ edition, 1983.

[3] F M Khan. *The Physics of Radiation Therapy*. Williams and Wilkins, 3$^{\text{rd}}$ edition, 2003.

[4] D W O Rogers, B A Faddegon, G X Ding, and J We. BEAM: A Monte Carlo code to simulate radiotherapy treatment units. *Med. Phys.*, 22(5):503–524, 1995.

[5] I D Fleming, J S Cooper, D E Henson, R V Hutter, B J Kennedy, G P Murphy, B O'Sullivan, L H Sobin, and J W Yarbro, editors. *AJCC Cancer Staging Manual*. Lippincott-Raven, 5$^{\text{th}}$ edition, 1997.

[6] G J Tortora and S R Grabowski. *Principles of Anatomy and Physiology*. John Wiley & Sons, Inc., 10$^{\text{th}}$ edition, 2003.

[7] ICRP. ICRP Publication 41: Nonstochastic effects of ionizing radiation. *Annals of the ICRP*, 14(3), 1984.

[8] J A K Patterson and R G Geronemus. *Cancer: Principles and Practice of Oncology*, volume 2. Lippincott, 3$^{\text{rd}}$ edition, 1989. Chapter 43: Cancers of the Skin.

[9] F Urbach. Geographic distribution of skin cancer. *Journal of Surgical Oncology*, 3(3):219–234, 1971.

[10] K Paver, K Poyzer, N Burry, and M Deakin. Letter: The incidence of basal cell carcinoma and their metastases in Australia and New Zealand. *Australas J Dermatol.*, 14(1):53, 1973.

[11] N R Telfer, G B Colver, and P W Bowers. Guidelines for the management of basal cell carcinoma. *British Journal of Dermatology*, 141:415–423, 1999.

[12] Varian Oncology Systems. *CadPlan External Beam Modelling: Physics*, 1998. P/N: CP30-20PH.

[13] A F Bielajew. Fundamentals of the Monte Carlo method for neutral and charged particle transport. Downloaded from http://www-personal.engin.umich.edu/ bielajew/MCBook/book.pdf in June 2005, 2001.

[14] I Kawrakow and D W Rogers. *The EGSnrc Code System:Monte Carlo Simulation of Electron and Photon Transport*. Ionizing Radition Standards, National Research Council of Canada, Ottawa, K1A OR6, 2003.

[15] J W Motz, H A Olsen, and H W Koch. Pair production by photons. *Reviews of Modern Physics*, 41(4):581–639, 1969.

[16] M J Berger. *Methods in Computational Physics*, volume 1, chapter Monte Carlo Calculation of the Penetration and Diffusion of Fast Charged Particles, page 135. Academic Press, New York, 1963.

[17] P Björk, T Knöös, and P Nilsson. Influence of initial electron beam characteristics on monte carlo calculated absorbed dose distributions for linear accelerator electron beams. *Phys. Med. Biol.*, 47:4019–4041, 2002.

[18] S B Jiang, A Kapur, and C M Ma. Electron beam modeling and commissioning for Monte Carlo treatment planning. *Med. Phys.*, 27(1):180–191, 2000.

[19] K Aljarrah, G C Sharp, T Neicu, and S B Jiang. Determination of the initial beam parameters in monte carlo linac simulation. *Med. Phys.*, 33(4):850–858, April 2006.

[20] F Verhaegen and J Seuntjens. Monte Carlo modelling of external radiotherapy photon beams. *Phys. Med. Biol.*, 48:R107–R164, 2003.

[21] D W O Rogers, B Walters, and I Kawrakow. *BEAMnrc Users Manual, NRCC Report PIRS-0509.* Ionizing Radiation Standards, National Research Council of Canada, 2005. Available online via: http://www.irs.inms.nrc.ca/inms/irs/BEAM/beamhome.html.

[22] P Alaei, B J Gerbi, and R A Geise. Evaluation of a model-based treatment planning system for dose computations in the kilovoltage energy range. *Med. Phys.*, 27(12):2821–2826, 2000.

[23] F Verhaegen, A E Nahum, S Van de Putte, and Y Namito. Monte Carlo modelling of radiotherapy kV x-ray units. *Phys. Med. Biol.*, 44:1767–1789, 1999.

[24] BJR Supplement 25. Central Axis Depth Dose Data for Use in Radiotherapy: 1996. Technical report, British Institute of Radiology, 1996. Joint Working Party of the British Institute of Radiology and the Institution of Physics and Engineering in Medicine and Biology.

[25] F Verhaegen, B Reniers, F Deblois, S Devic, J Seuntjens, and D Hristov. Dosimetric and microdosimetric study of contrast-enhanced radiotherapy with kilovolt x-rays. *Phys. Med. Biol.*, 50:3555–3569, 2005.

[26] X A Li, C M Ma, D Salhani, and O Agboola. Dosimetric evaluation of a widely used kilovoltage x-ray unit for endocavitary radiotherapy. *Med. Phys.*, 25(8):1464–1471, August 1998.

[27] Technical Report Series No. 398. Abosrbed dose determination in external beam radiotherapy: An international code of practice fro dosimetry based on standards of absorbed dose to water. Technical report, International Atomic Energy Agency, 2000.

[28] D W O Rogers. Fifty years of Monte Carlo simulations for medical physics. *Phys. Med. Biol.*, 51:R287–R301, 2006.

[29] Varian Medical Systems. *Vision™ Electron Monte Carlo Algorithm: Reference Guide*, 2003. P/N B4 01998R01A.

[30] H Neuenschwander, T R Mackie, and P J Reckwerdt. Mmc - a high performance Monte Carlo code for electron beam treatment planning. *Phys. Med. Biol.*, 40:543–574, 1995.

[31] J J Janssen, E W Korevaar, L J van Battum, P R M Storchi, and H Huizenga. A model to determine the initial phase space of a clinical electron beam from measured beam data. *Phys. Med. Biol.*, 46:269–286, 2001.

[32] J E Cygler, C Lochrin, G M Daskalov, M Howard, R Zohr, B Esche, L Eapen, L Grimard, and J M Caudrelier. Clinical use of a commercial Monte Carlo treatment planning system for electron beams. *Phys. Med. Biol.*, 50:1029–1034, 2005.

[33] V W Huang, J Seuntjens, S Devic, and F Verhaegen. Experimental determination of electron source parameters for accurate Monte Carlo calculation of large field electron therapy. *Phys. Med. Biol.*, 50:779–786, 2005.

[34] G X Ding and D W O Rogers. Energy spectra, angular spread and dose distributions of electron beams from various accelerators used in radiotherapy (pirs-0439). Technical report, Institute for National Measurements Standards, National Research Council of Canada, 1995.

[35] D Hossain. Personal communication, 2006.

[36] B Frass, K Doppke, M Hunt, G Kutcher, G Starkschall, R Stern, and J Van Dyke. American Association of Physicists in Medicine Radiation Therapy Committee Task Group 53: Quality assurance for clinical radiotherapy treatment planning. *Med. Phys.*, 25(10):1773–1829, 1998.

[37] B E Currie. Transmission Factors, Depth Dose Curves and Relative Dose Profiles for MED-TEC MT-T-45 Medium and Small Tungsten Eyeshields in 6 and 9 MeV Electron Beams. Wellington Blood and Cancer Centre Internal Physics Report, 2003.

[38] R D Weaver, B J Gerbi, and K E Dusenbury. Evaluation of eye shields made of tungsten and aluminium in high-energy electron beams. *Int. J. Rad. Onc. Biol. Phys.*, 41(1):233–237, 1998.

[39] G D Lambert, M R Sandland, A C Whitton, and D Doughty. Combining backscattered electrons and low energy photons to improve the dose distribution to an eyelid. *Int.*, 11:617–620, 1985.

[40] C M Wilson, D P Schreiber, J D Russell, and P Hitchcock. Electron beam versus photon beam radiation therapy for the treatment of orbital lymphoid tumors. *Medical Dosimetry*, 17:161–165, 1992.

[41] F Verhaegen, F M Buffa, and C Deehan. Quantifying effects of lead shielding in electron beams: a Monte Carlo study. *Phys. Med. Biol.*, 46:757–769, 2001.

[42] R J Amdur, K J Kalbaugh, L M Ewald, J T Parsons, W M Mednedhall, F J Bova, and R R Million. Radiation therapy for skin cancers near the eye: kilovoltage x-rays versus electrons. *Int. J. Rad. Onc. Biol. Phys.*, 23(4):769–779, 1992.

[43] Washington University in St. Louis Advanced Radiotherapy Treatment Planning Group. http://radium.wustl.edu/cerr/. Internet webpage. CERR version 3.0 Beta 1 downloaded 28 August 2006.

[44] A S Shiu, S S Tung, R J Gastrof, K R Hogstrom, W H Morrison, and L J Peters. Dosimetric evaluation of lead and tungsten eye shields in elctron beam treatment. *Int. J. Rad. Onc. Biol. Phys.*, 35(3):599–604, 1996.

[45] C R Baker, F Luhana, and S J Thomas. Absorbed dose behind eye shields during kilovoltage photon radiotherapy. *British Journal of Radiography*, 75:685–688, 2002.